ABSTRACT

Title of dissertation: PIEZOELECTRIC MICROBEAM RESONATORS BASED ON EPITAXIAL $Al_{0.3}Ga_{0.7}As$ FILMS

Lihua Li, Doctor of Philosophy, 2005

Dissertation directed by: Professor Don DeVoe
Department of Mechanical Engineering

In this work, piezoelectric resonators based on single crystal $Al_{0.3}Ga_{0.7}As$ films are implemented. The combination of Si doped $Al_{0.3}Ga_{0.7}As$ as electrode layers and moderate piezoelectric properties of updoped $Al_{0.3}Ga_{0.7}As$ film leads to lattice matched single crystal resonators with high attainable quality factors and capability of integration with high speed circuits.

To validate the fabrication process, simple cantilever beam structures are developed and characterized by laser Doppler vibrometry. In order to achieve higher center frequencies, a clamped-clamped (c-c) beam design is explored. Important resonator parameters including resonance frequency, quality factor, and power handling ability are investigated. Measured quality factors of c-c beams were found to be limited by anchor losses to the substrate. A free-free (f-f) beam design is proposed in order to alleviate the energy dissipation due to anchor losses. Fabricated f-f beam devices show increased quality factors compared to the c-c beam design. Another improvement is the adoption of bimorph configuration instead of unimorph configuration.

Compared to unimorph cantilever beam design, bimorph cantilevers showed 80% to 120% of increase in displacement with the same driving voltage without significant change in quality factors.

The quality factors of flexural mode resonators in atmospheric pressure are low due to the effect of air damping. For this reason, proper working of flexural mode resonators requires a vacuum package which imposes unwanted complexity in packaging. To solve this problem, length-extensional mode resonators (bar resonators) are proposed to take advantage of low air shear damping. Bar resonators with lengths ranging from $1000\mu m$ to $100\mu m$ have been fabricated and tested. Measured resonant frequencies range from 2.5 MHz to 72 MHz with good matching to theoretical predictions. The quality factors of bar resonators at their first resonant frequency are measured in air and in high vacuum, showing values between 4,300 – 8,900 and 8,000 – 17,000, respectively, with corresponding measured motional resistances of 7.3 kΩ – 10.5 kΩ and 4.0 kΩ – 7.8 kΩ, respectively. The developed bar resonators showed excellent power handling ability up to -10 dBm which is much higher than equivalent electrostatic resonators.

PIEZOELECTRIC MICROBEAM RESONATORS BASED ON EPITAXIAL $Al_{0.3}Ga_{0.7}As$ FILMS

by

Lihua Li

Dissertation submitted to the Faculty of the Graduate School of the
University of Maryland, College Park in partial fulfillment
of the requirements for the degree of
Doctor of Philosophy
2005

Advisory Committee:

Professor Don DeVoe, Chair/Advisor
Professor Balakumar Balachandran
Professor Amr Baz
Associate Professor Bongtae Han
Professor Norman Wereley

DEDICATION

To my husband Xingzhi Wen and my mother for their support of my work.

ACKNOWLEDGMENTS

I would like thank my advisor Dr. Don DeVoe for his guidance and support of this work. I would also like thank Dr. Parshant Kumar for his excellent work on device fabrication. I am also grateful to my fellow students in Maryland MEMS Lab for their assistance and advise on this work. This work is funded by DARPA grant. I would also like people over LPS for their support in film growth and microfabrication.

TABLE OF CONTENTS

LIST OF FIGURES

Chapter 1

Introduction

1.1 Motivation

Filters are important elements in radio communication systems. Proper operation of receivers and transmitters requires filters in the VHF (30 MHz to 300 MHz) and UHF (300 MHz to 1 GHz) range with low insertion loss and high quality factors to protect receivers from adjacent channel interference and limit the bandwidth of transmitter noise [1]. Fig. 1.1 shows the frequency response of a typical bandpass filter as well as definitions of some important parameters for bandpass filters. The ongoing development in wireless communication technology requires high performance frequency control devices as spectrum crowding increases, with additional requirements including a higher level integration and low cost.

Discrete RLC circuits are used extensively as a building block of bandpass filters. However, traditional RLC circuits become increasingly unable to provide adequate quality factors at high frequencies because required component values are often impractical to realize using VLSI technology. Taking a bandpass filter with center frequency of 1 MHz and quality factor of 100,000 as an example, the required inductor and capacitor values are about 8 H and 3.2 fF, respectively, which is difficult to realize with traditional IC technology [2]. Bulk Acoustic Wave (BAW) and Sur-

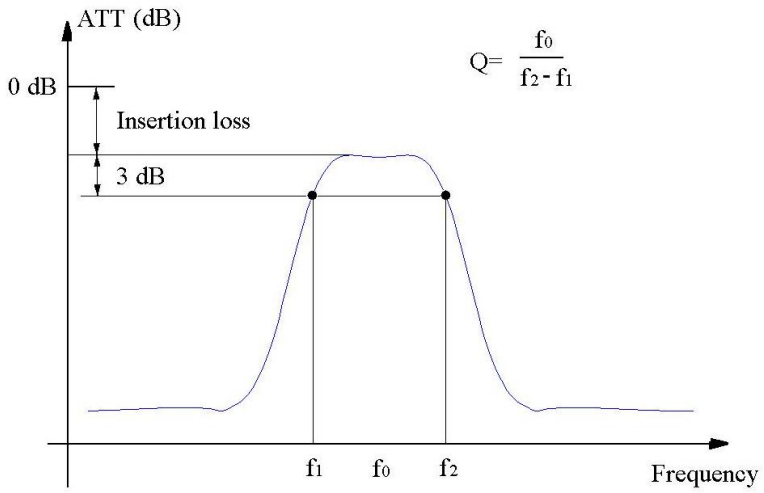

Figure 1.1: Frequency response of a typical bandpass filter.

face Acoustic Wave (SAW) resonators are widely used as an option to replace RLC circuits, but they still suffer from problems including large volumes, and difficulty with circuit integration [3]. Film Bulk Acoustic Resonators (FBAR) overcome the size issue and have GHz frequencies, but still have problems of integration with circuits. Also, multiple frequency devices cannot be implemented on the same chip because the center frequency is dependent on the thickness longitudinal vibration of the piezoelectric film [4].

Similarly, mechanical filters have been used where narrow bandwidth, low loss, and good stability are required. Mechanical filters transform electrical signals into mechanical energy, perform a filtering function, then transform mechanical energy back to electrical energy. Ever since the first reported mechanical filters in 1946 by Robert Adler of Zenith [5], mechanical filters found wide spread use in telephone technol-

ogy. The reason behind the rapid development of mechanical filters lies in their inherent characteristics such as a high Q, good temperature stability, and good aging properties, which are all critical in achieving low-loss, narrow bandwidth, stable bandpass filters. The early macroscopic mechanical filters have typical center frequencies lower than 600 kHz due to their size and manufacturing capability. The insertion losses are typically about 2 dB. Apparently, these macroscopic mechanical filters have little use in modern day communication applications, due to their low center frequencies, difficulty of integration, and large volume they occupy [5].

In contrast, micromechanical resonators offer the potential to alleviate many of the key problems with existing filter technology. With reduced dimensions produced by modern MEMS technology, micromechanical resonators have emerged as a promising candidate for future RF filters. In fact, micromechanical resonator based filters have been the subject of extensive interest and exploration over recent years. The motivation for developing micromechanical resonator filters lies on the potential to fabricate high center frequency, low volume, low power consumption, high Q on-chip filters. A number of approaches to micromechanical resonators have been investigated in the context of MEMS technology. The most widely investigated resonators include devices based on electrostatic and piezoelectric transduction.

Electrostatic resonators have been successfully reported by taking advantage of low loss nature of polycrystalline silicon and well-developed integrated circuit (IC) processes [6]. In one recent report, an electrostatically actuated disk resonator fabri-

cated in poly-Si, provided a quality factor of 40,000 in vacuum with a 148 MHz center frequency [7]. As the frequency range goes higher, the desired gap between the electrode and the resonator will shrink down to nanometer range in order to achieve adequate electromechanical coupling force and will pose a main challenge to their future application.

Piezoelectric micromachined beam resonators offer an alternative for high-frequency filters because of the following factors: first their power consumption is very low, and they also need a low input voltage, normally smaller than 5V; second, piezoelectric transduction of thin films, when designed in certain modes, creates a moment at the beam's boundaries while in contrast, electrostatic transduction creates a distributed force across the beam length. For this reason, compared to electrostatic resonators, it is suggested that piezoelectric resonators can provide higher electromechanical strength at higher frequency range, yet they have better scalability down to nanoscale [8]. This increased electromechanical coupling coefficient linking electrical and mechanical sides of a transducer will manifest itself when desired center frequencies increase. For these reasons, various groups are starting to pay attention to the development of piezoelectric micromechanical resonators for bandpass filter applications. Various piezoelectric materials including ZnO [8, 9], PZT [10], and AlN [11, 12] have been utilized in piezoelectric resonator applications.

1.2 Dissertation Objective

The main objective of this dissertation work is to realize high-Q piezoelectric resonators based on single crystal thin film $Al_{0.3}Ga_{0.7}As$ material. Both piezoelectric and electrode layers are based on lattice matched thin film $Al_{0.3}Ga_{0.7}As$. The combination of low damping single crystal nature inherent in this material and lattice matched heterostructures will potentially result in high quality factors obtainable with this approach. Various design schemes including flexural mode resonators such as cantilever, clamped-clamped, and free-free beam resonators, longitudinal and disk resonators are explored. The developed resonators are first analyzed, both theoretically and with finite element method, and then compared to experimental results. The experimental methods include optical characterization based on Laser Doppler Vibrometer (LDV) and electrical characterization with circuits developed uniquely for this project.

1.3 Dissertation Organization

Chapter 1 gives an introduction to this dissertation work, including the background of filter technology, and the purpose of this work. Chapter 2 gives a literature review. In this chapter, different kinds of microelectromechanical resonators are compared and the benefits of the approach conducted in this work, namely piezoelectric resonators based on single crystal $Al_{0.3}Ga_{0.7}As$, are explained. In chapter 3, details of the fabrication processes used for realizing $Al_{0.3}Ga_{0.7}As$ resonators based on inductively coupled plasma reactive ion etching (ICPRIE) combined with

wet etching release, or focused ion beam etching (FIB) combined with wet etching release process, are presented. In chapter 4, following a theoretical analysis of the piezoelectric properties of $Al_{0.3}Ga_{0.7}As$, analytical models for micro beam resonators including flexural mode resonators and longitudinal mode resonators are compared with finite element results obtained with ANSYS simulation. In chapter 5, the principle of the optical and electrical characterization methods used in this work are described, including impedance measurement, charge amplification, and self-sensing measurement. In chapter 6, the characterization results for flexural mode resonators including cantilever, clamped–clamped beam, and free–free beam resonators are provided. In chapter 7, the results from bimorph cantilever resonators are compared to unimorph cantilever resonators to show the benefits of bimorph configuration. In chapter 8, the measurement results from length extensional mode bar resonators are presented and compared to the results from flexural mode resonators to extract their inherent characteristics. In chapter 9, a discussion of the results from this work is presented, and potential future directions for exploring the full potential of single crystal $Al_{0.3}Ga_{0.7}As$ piezoelectric resonators are described.

Chapter 2

Literature Review

To work as electrical bandpass filters, micromechanical resonators need to transform energy between the mechanical domain and electrical domain. Many different electromechanical transduction mechanisms have been shown to be suitable for excitation and detection of the vibration of microelectromechanical resonators. In this chapter, electrostatic, piezoelectric and electromagnetic microelectromechanical resonators are introduced, compared, and summarized. Finally, the approach conduced in this project is detailed.

2.1 Electrostatic Resonators

Fig. 2.1 shows the configuration of a typical electrostatic resonator. A sinusoidal voltage is applied between the beam and the substrate and the beam is excited by Coulomb forces between the two electrodes. If C is the capacitance of between the beam and the substrate, d is the gap between the beam and the substrate, and V is applied voltage, then the electrostatic force can be calculated as $\frac{1}{2}\frac{CV^2}{d}$. From the expression of electrostatic force two things are clear: electrostatic actuation is inherently nonlinear to the applied force; electrostatic forces are inversely proportional to the gap between the beam and the substrate. In application, a high DC voltage is added between two electrodes of the beam to set a proper working zone;

the gap between two electrodes are very small (often in submicron range) to get high electrostatic forces.

The sensing of small displacement in electrostatic resonators are often implemented by measuring capacitance change between two electrodes. Capacitive sensing has many attractive features such as good sensitivity, excellent temperature stability. Also, the capacitive sensing circuit can be implemented with CMOS circuit, which is especially attractive for electrostatic resonators sensing.

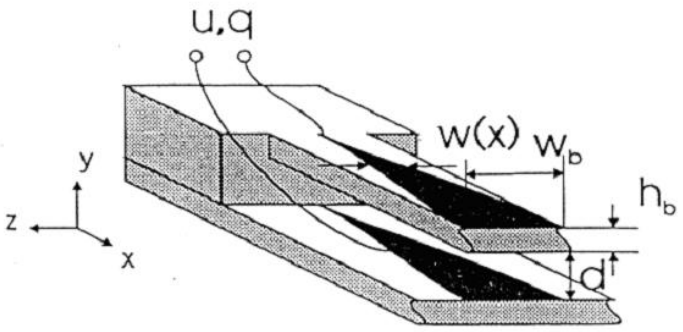

Figure 2.1: Configuration of an electrostatic resonator [13].

Most of the reported electrostatic resonators are based on silicon material due to the low loss nature inherent in this material and also, because of the well developed micromachining technology based on silicon material. Various design schemes such as clamped-clamped beam [14], disk [7, 15], and free-free beam [15] resonators have been reported.

Fig. 2.2 shows an SEM picture of a disk resonator based on single crystal silicon

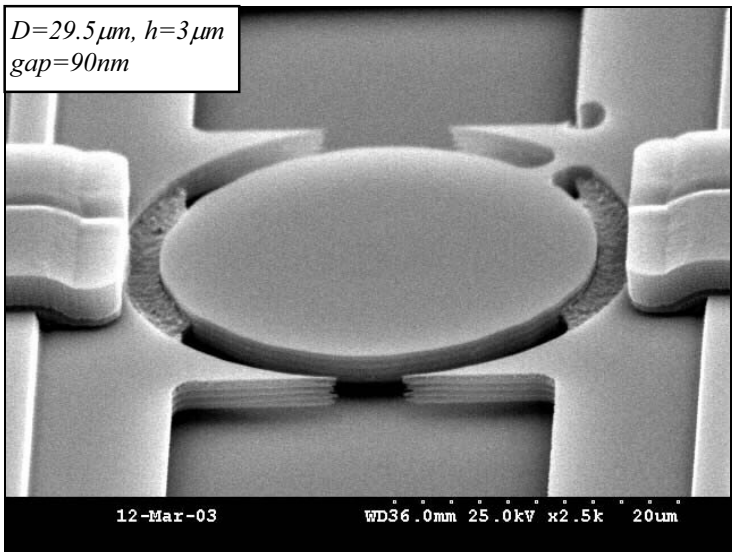

Figure 2.2: SEM of a reported electrostatic disk resonator [7].

fabricated by Ayazi et al. The resonator has diameter of 30 μm and thickness of 3 μm and is supported by a 1.7 μm wide, 2.7 μm long support at one resonance node point. The frequency response of this resonator is given in Fig. 2.3 which shows center frequency of 148 MHz and quality factor of 39,300 in vacuum.

The fabrication process of Si based electrostatic resonators is compatible with standard IC processing, making electrostatic resonators relatively easy to integrate with circuits. The low loss nature of Si and poly-Si contributes to high quality factors with these resonators.

On the other hand, the electrostatic resonators have many drawbacks which will put difficulty in application. First, the transduction strength of electrostatic resonators is weak distributed forces and suffer from a fast degradation; Second, the

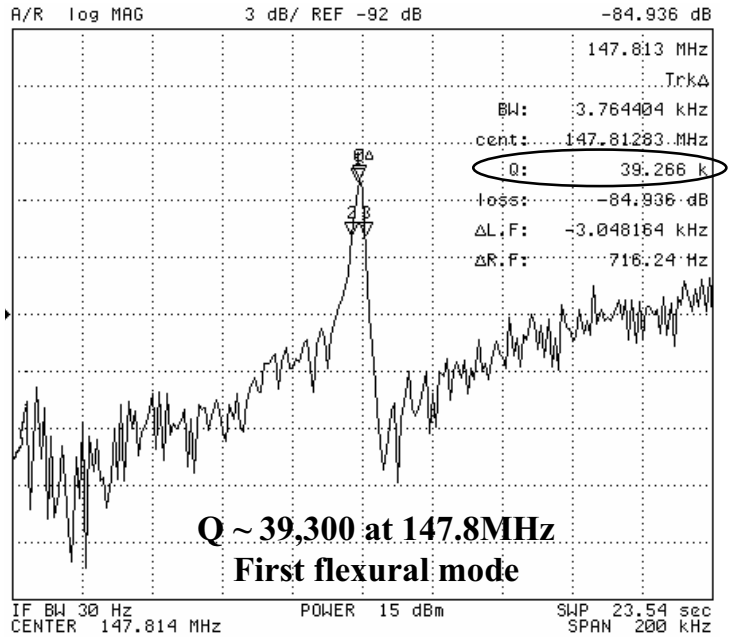

Figure 2.3: Frequency response of the disk resonator [7].

required size of air-gap for electrostatic resonators normally lies in submicron or nanometer range and tends to decrease as the center frequency increase, putting complexity in fabrication process; third, the driving force F is proportional to E^2 and for this reason, the electrostatic resonators are inherently nonlinear. Most often, in order to get a proper working zone, a DC bias voltage higher than 10V is added which makes electrostatic resonators not compatible with traditional CMOS circuits.

2.2 Electromagnetic Resonators

The operational configuration of electromagnetic resonators is shown in Fig. 2.4 [13]. In this configuration, a beam resonator is placed perpendicular to a homo-

geneous magnetic filed. An alternating current along the resonant beam generates a Lorentz force which drives the beam. When the driving frequency matches the resonance frequency of the beam, resonant motion occurs in the beam, which, in turn, induces an electromotive force (EMF) at the output terminal.

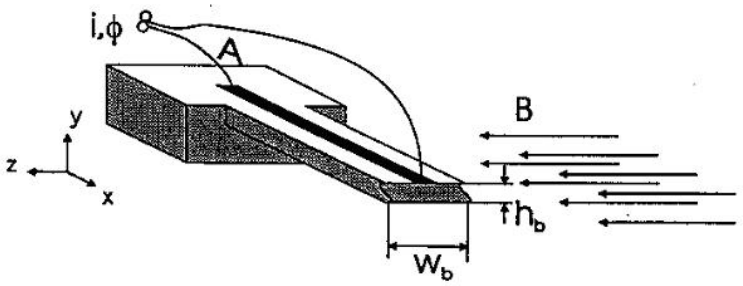

Figure 2.4: Configuration of the electromagnetic resonators.

Electromagnetic beam resonators based on single crystal 3C-SiC films [16] and Si [17] have been reported. Fig. 2.5 shows an SEM picture and frequency response of a 3C-SiC resonator realized by Roukes et al. The beam under test is positioned perpendicular to a strong magnetic field (1 to 8T) in vacuum at cryogenic temperatures. The natural frequency for clamped-clamped and free-free beam resonators are 174 MHz and 178 MHz respectively and their quality factors are about 4,500 and 11,000 respectively.

Electromagnetic resonators showed a good scalability down to nano-scale. The electromechanical coupling factor in this case, is depend on the strength of magnetic field. In order to get enough force to drive the beam, the beam must be placed in

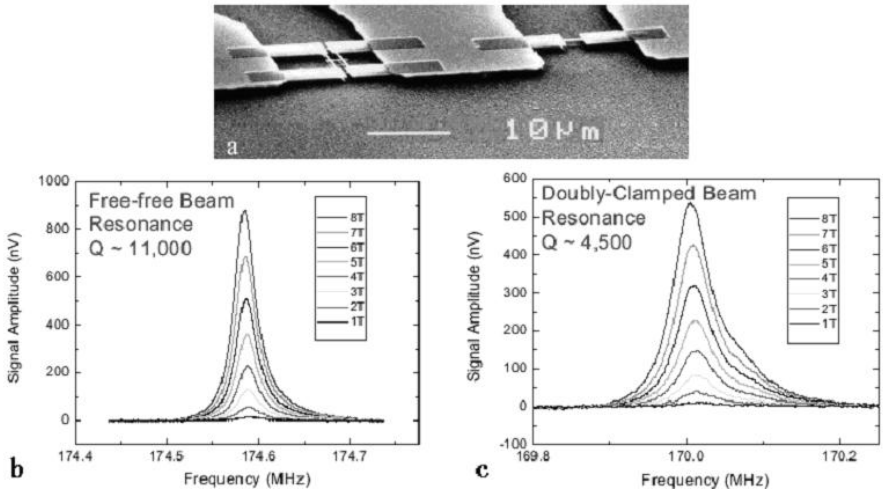

Figure 2.5: (a) SEM micrograph of SiC resonator, (b) frequency spectrum of free-free beam resonator, and (c) frequency spectrum of clamped-clamped beam resonator [16].

a strong magnetic field (larger than 1T) which must be generated by a superconducting solenoid. For this reason, the application of electromagnetic resonators in bandpass filters for communication systems and related applications is not realistic at this moment.

2.3 Piezoelectric Beam Resonators

A piezoelectrically operated resonator consists of a piezoelectric film sandwiched between two electrodes. The piezoelectric film develops a mechanical strain when it is subject to an input voltage by reverse piezoelectric effect, thus performing the function of actuating the resonator; on the other hand, the piezoelectric film generates au output electric voltage when it is subjected to an input mechanical

strain by forward effect, thus sensing the vibration of the resonator.

Piezoelectric resonators based on ZnO [8, 9, 18], PZT [10], and AlN [11, 12] have been reported. Fig. 2.6 shows configuration of a clamped-clamped beam piezoelectric resonator reported by DeVoe [8]. A piezoelectric film (ZnO) is deposited on a Si based elastic beam which is anchored to the substrate at each end. The piezoelectric film provides input moment to drive the beam. On the other hand, the resulting motion is sensed by the piezoelectric film on the other side of the beam. The top electrode is clipped at the quarter length of the beam on both sides to realize a maximum driving moment at driving port, and maximum sensitivity at sensing port.

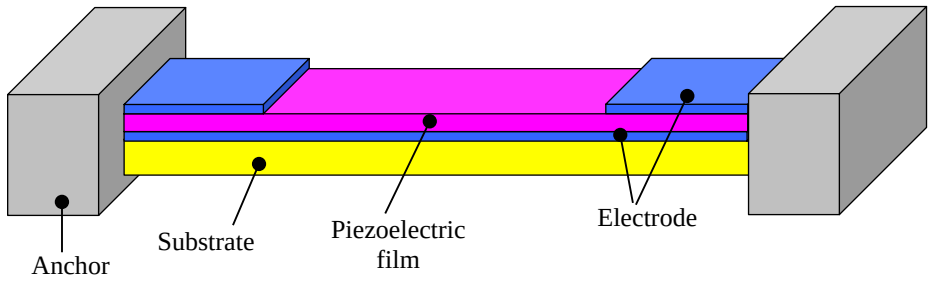

Figure 2.6: Schematic of a piezoelectric clamped-clamped beam resonator.

Clamped-clamped micromechanical resonators using ZnO as piezoelectric layer have been reported with measured center frequencies ranging from 158 kHz to 1.18 MHz and quality factors as high as 3,700 at lower frequencies [8], while resonators with sol-gel PZT as the piezoelectric material have been realized with center frequencies

up to 9.2 MHz and quality factors greater than 1,000 in vacuum and greater than 400 in air [10]. Resonators employing AlN as piezoelectric film showed resonance frequencies above 80 MHz, and quality factors in excess of 20,000 [11]. Recently, Pisano et al. reported ring-shaped piezoelectric resonators based on AlN film with Qs of 2,900 for center frequency of 472.7 MHz in air [12], and Ayazi et al. have reported length longitudinal resonators based on ZnO film deposited on SOI substrate with a resonance frequency as high as 210 MHz with a Q of 4,100 under vacuum [9]. A summary of reported micromechanical resonators is presented in table 2.1.

Because piezoelectric resonators are designed to be driven by driving moment provided by piezoelectric material, piezoelectric resonators provide relatively strong electromechanical coupling force at higher frequency range compared to electrostatic resonators. For instance, DeVoe [8] compared electromechanical coupling factors between a piezoelectric resonators and a comb drive electrostatic resonator, and found the coupling strength of the modeled piezoelectric resonator is an order of magnitude larger than the comb drive case. By further comparison of electromechanical coupling factor of piezoelectric resonators and parallel plate electrostatic resonators with boundary condition of clamped-clamped case, it is shown that

$$\frac{\eta_{piezo}}{\eta_{plate}} \propto \omega_1^2 \tag{2.1}$$

For this reason, bending-mode piezoelectric resonators features better scalability. Also, the low driving voltage and linear relationship between driving voltage and amplitude of vibration makes the piezoelectric resonator a good candidate for the

future on chip band pass filter building elements.

However, the fabrication of piezoelectric resonators were normally not compatible with standard IC fabrication process, and it was also hard to integrate traditional piezoelectric material, including ZnO, PZT ceramics, AlN etc. to traditional IC circuits. Also, the use of metal layers as electrodes limited their attainable quality factors.

2.4 AlGaAs Resonators

The motivation behind this project is to develop piezoelectric micro resonators for high-Q filter arrays with center frequencies in HF and VHF range, high quality factors, low power consumption and motional resistance. The developed resonators should have a good scalability to RF frequency range, and also should have capability of integration with IC circuits in the future.

In order to achieve the goals stated previously, single crystal $Al_{0.3}Ga_{0.7}As$ films grown on GaAs substrates by Molecular Beam Epitaxy (MBE) is chosen as constructing fabrication for the following reasons: first, the high quality of epitaxial $Al_{0.3}Ga_{0.7}As$ thin films may offer low internal loss, thus minimizing the energy loss due to internal damping; second, thin film $Al_{0.3}Ga_{0.7}As$ grown by well-characterized epitaxial growth process is capable of nanometer patterning for future GHz range resonators; third, moderate piezoelectric coupling factor of undoped of $Al_{0.3}Ga_{0.7}As$

Table 2.1: Summary of recently-reported MEMS resonators.

Type	Resonator mode	f_{max}	Q	Material	Ref.
electrostatic	clamped-clamped	34.5 MHz	NA	poly Si	[6]
	free-free beam	92 MHz	8,000 (vacuum)	poly Si	[6]
	contour mode	156 MHz	94,000 (vacuum)	poly Si	[15]
	flexural disk	148 MHz	40,000 (vacuum)	SOI	[7]
electromagnetic	free-free beam	174 MHz	11,000 (vacuum)	3C-SiC	[16]
	clamped-clamped	170 MHz	4,500 (vacuum)	3C-SiC	[16]
	clamped-clamped	70.7 MHz	20,000 (vacuum)	SC Si	[17]
piezoelectric	clamped-clamped	1.18 MHz	930 (vacuum)	ZnO	[8]
	clamped-clamped	9.2 MHz	1,000 (vacuum)	PZT	[10]
	clamped-clamped	80 MHz	20,000 (vacuum)	AlN	[11]
	longitudinal	210 MHz	4,100 (vacuum)	ZnO	[9]
	contour mode	472.7 MHz	2,900 (air)	AlN	[12]

film is suitable of both excitation and sense of the resonator; third; the developed resonators can be integrated into high-speed IC circuits in future; last not least, conductivity of $Al_{0.3}Ga_{0.7}As$ films can be changed by adding dopants during film growth process, giving the possibility of replacing conventional high-loss amorphous metal electrode layers with lattice matched single crystal electrode layers.

Different mode resonators including clamped-clamped beam, cantilever beam, free-free beam resonators, and bar resonators are investigated. The developed resonators are characterized in air or under vacuum in order to minimize the effect of air damping. Optical characterization based on laser Doppler vibrometer (LDV) is conducted on resonators with resonance frequencies lower than 2 MHz. For resonators with center frequencies beyond this region, a customized sensing circuit is developed to characterize these higher frequency resonators.

Chapter 3

Fabrication

In this chapter, a general overview of III-V MEMS technology is given first, followed by fabrication process of resonators developed in this project. Two different fabrication processes based on different sacrificial etching are developed. Resonators based on GaAs sacrificial etching are restricted to certain orientation due to the anisotropic nature of the etching process. Those resonators based on $Al_{0.7}Ga_{0.3}As$ sacrificial etching can be placed in any direction because the wet etching process is isotropic in this case.

3.1 III-V MEMS Summary

3.1.1 General Overview

Si (also including polysilicon, oxide, nitride, etc.) based MEMS are now well understood and widely used in micro sensors and micro actuators. In addition to this, gallium arsenide (GaAs) based MEMS offers some material-related and technological advantages over Si. Some well-known properties of GaAs include direct band gap transition and high mobility of electrons [19]. GaAs is also a good material for high temperature electronics due to its large band gap [19]. GaAs also has piezoelectric properties comparable with those of quartz [19][20], and piezoresistive characteristics with piezoresistive values higher than those of Si [19][23].

Ever since the first report of GaAs integrated circuit in 1974, various III-V material based devices including heterojunction bipolar transistors, stripe lasers and vertical cavity surface emitting lasers, or VCSELs are developed [24]. GaAs thermal based sensors including infrared sensors, themoconverters, gas-flow sensors are under investigations [26]. GaAs pressure sensors based on piezoelectricity, piezoresistivity, piezooptic and resonant tunneling diodes have been investigated in order to take advantage of GaAs intrinsic characteristics [19][27][23]. Another useful III-V material is aluminum nitride. Surface acoustic wave (SAW) devices, thin-film bulk acoustic resonators (TFBAR) [28][29] and solidly mounted resonators [28] based on thin film AlN have been developed to take advantage of wide-band gap, high electrical resistance, high breakdown voltage, and low dielectric loss characteristics of AlN. Other reported micromechanical sensors in III-Vs include fiber optic accelerometers, thermopile devices such as anemometers, and IR-sensors, and microwave effect sensors [30].

3.1.2 Fabrication Techniques

A great number of micromachining techniques have been developed for III-V MEMS micromachining, such as selective etch stops for hetero and homostructure of varying electrical properties, sacrificial layer techniques with etch rate selectivities up to 10^6 , and dry and wet etching for isotropic and anisotropic shaping [30]. Basically, the micromachining techniques are based on two factors. First is the selective

characteristic etching of heterostructures and damaged layers, due to different etch rates of GaAs and its alloys. Second is the unique profile presented by III-V compounds (zinc blende crystals) when preferential etching solutions are applied [26]. For example, sacrificial etching of III-Vs is frequently used in lift-off epitaxy, and etch free standing III-V based micro structures for fluidic self-assembly on a host substrate [30].

Another important technology for III-V micromachining is heteroepitaxy. Heteroepitaxy of III-Vs provide a multitude of combinations of cubic alloys with Ga, Al, and In as group-III elements; and As, P and Sb as group-V elements [30]. Compounds with direct and indirect bandgaps are possible. Most epitaxy layers are lattice matched to the substrates and for this reason, internal strain level is low. Also, the thickness of each layer can be controlled very precisely (one or two monolayers), thus gives more precision in micromachining. For GaAs substrates, the lattice matched alloy by far most commonly used is $Al_xGa_{1-x}As$ [25]. It is also in this system that one may find most work and applications of sacrificial etching [24]. For InP substrates, the most common lattice-matched alloys are the InGaAsP quaternaries and their ternaries.

3.2 Fabrication Process Flows

The developed resonators in this project are based on single crystal $Al_xGa_{1-x}As$ films grown on GaAs substrates by Molecular Beam Epitaxy (MBE). Sequential lay-

ers of $Al_xGa_{1-x}As$ films with different Al more fraction and doping levels are grown on 3-inch (100) GaAs substrates. Depending on sacrificial layers envolved, two different structures are developed.

3.2.1 GaAs as Sacrificial Layer

The constructing material in this case is undoped piezoelectric $Al_{0.3}Ga_{0.7}As$ layer sandwitched between two Si doped $Al_{0.3}Ga_{0.7}As$ electrode layers. GaAs substrate is etched at final step to release free standing structures.

The doping levels of Si in both the top and bottom electrode layers are on the order of 10^{18} atoms/cm^3. The typical measured resistivities of top and bottom $Al_{0.3}Ga_{0.7}As$: Si are 0.05 ohm-cm and 0.07 ohm-cm respectively. The slightly higher resistivity of bottom electrode layer is believed to be due to the Si redistribution during epitaxial growth of the following $Al_{0.3}Ga_{0.7}As$ and $Al_{0.3}Ga_{0.7}As$: Si layers.

The fabrication process consists of Inductively Coupled Plasma Reactive Ion Etching (ICP RIE) of $Al_{0.3}Ga_{0.7}As$ layers, metalizaiton on conductive $Al_{0.3}Ga_{0.7}As$: Si layers to ensure good ohmic contact, and selective wet etching of GaAs substrate to release free standing structures. Fig. 3.1 gives schematics of cross sectional view of fabrication process.

The first step is etching down to bottom $Al_{0.3}Ga_{0.7}As$: Si layers by ICP RIE to get

access to the bottom $Al_{0.3}Ga_{0.7}As$ electrode layer as well as to get rid of parasitic capacitance. Metalization using a multilayer stack of Pd/Ge/Ni/Au (with thickness of 50nm, 40nm, 20nm, 100nm, respectively) is performed on selected top and bottom $Al_{0.3}Ga_{0.7}As$: Si electrode areas using a lift-off process, followed by rapid thermal annealing at 380 $^{\circ}C$ for 30 sec to provide a good ohmic contact. Next, regions of the top $Al_{0.3}Ga_{0.7}As$: Si layer are patterned by ICP RIE to define top electrode geometries. The full $Al_{0.3}Ga_{0.7}As$ stack layers are patterned by ICP RIE to define the structural beam elements. Finally the patterned beams are released by bulk wet etching of GaAs substrate. Since the beam is released by wet etching process, the supercritical drying is required to prevent the beams from adhering to the substrate due to capillary forces.

The use of ICP enables extremely high ion flux and at the same time, keep the ion energy low to reduce surface damage. With optimized ICP etching process, the resulting sidewalls are smooth and vertical. The etch selectivity among doped and undoped $Al_{0.3}Ga_{0.7}As$ and GaAs substrate is poor, therefore timed etching with endpoint detection is required to accurately control etch stops. The anisotropic nature of GaAs wet etching makes it impossible to release free standing structure in <110> direction. Only structures oriented at 15° to 45° with respect to <110> direction could be released using this technology. Fig. 3.2 gives SEM image of a typical developed cantilever beam resonator with beam length of 60 μm. The island structure due to anisotropic etching of GaAs substrate is clearly visible from the figure. The resulting sidewalls of ICP etching is shown to be straight and smooth,

rendering nanoscale resonator fabrication capability with this fabrication process. The round curves on the edge of the beam, and the anchor points are due to the poor quality of employed mask and low resolution from contact lithogrphy process. The future patterning of beam structures with projection lithograpy process and thin photoresist should be able to overcome this problem.

In addition to ICP RIE , focused ion-beam (FIB) milling is used to etch $Al_{0.3}Ga_{0.7}As$ layers. Although not as effective as ICP RIE, the FIB process provides the potential to realize nano-scale piezoelectric $Al_{0.3}Ga_{0.7}As$ resonators for ultra-high frequency applications for future work. Fig. 3.3 shows the SEM image of a typical beam structure fabricated by FIB/GaAs wet etching release method. The constructing three different doping levels of $Al_{0.3}Ga_{0.7}As$ layers are clearly visible. The resulting sidewalls in this case is also clean and smooth. One important thing in FIB fabrication is the redepotion of etched material on the sidewalls which will potentially lead to short circuit and lower the attainable quality factor. One can partly solve this problem by lowering ion current level for etching, and using gas assisted FIB etching.

3.2.2 $Al_{0.7}Ga_{0.3}As$ as Sacrificial Layer

In order to get free standing structures in <110> direction where the maximum electromechanical coupling factor lies, resonator fabrication process based on sacrificial wet etching of $Al_{0.7}Ga_{0.3}As$ has been developed.

The typical starting material from substrate is 0.5 μm $Al_{0.3}Ga_{0.7}As$ as etch stop layer, 2 μm $Al_{0.7}Ga_{0.3}As$ as sacrificial layer, followed by Si doped $Al_{0.3}Ga_{0.7}As$ layers as bottom electrode layer, piezoelectric $Al_{0.3}Ga_{0.7}As$ layer, and again Si doped $Al_{0.3}Ga_{0.7}As$ as top electrode layer. The fabrication step is similar to the case of GaAs as sacrificial layer, except for the final release step. In this case, the free standing structures are obtained by selective etching between $Al_{0.7}Ga_{0.3}As$ and $Al_{0.3}Ga_{0.7}As$. The sacrificial etching of $Al_{0.7}Ga_{0.3}As$ is isotropic. Therefore, structures in any orientation can be released. Fig. 3.4 gives the schematics of fabrication process. Fig. 3.5 gives the SEM image of a 200 μm long clamped-clamped beam after release.

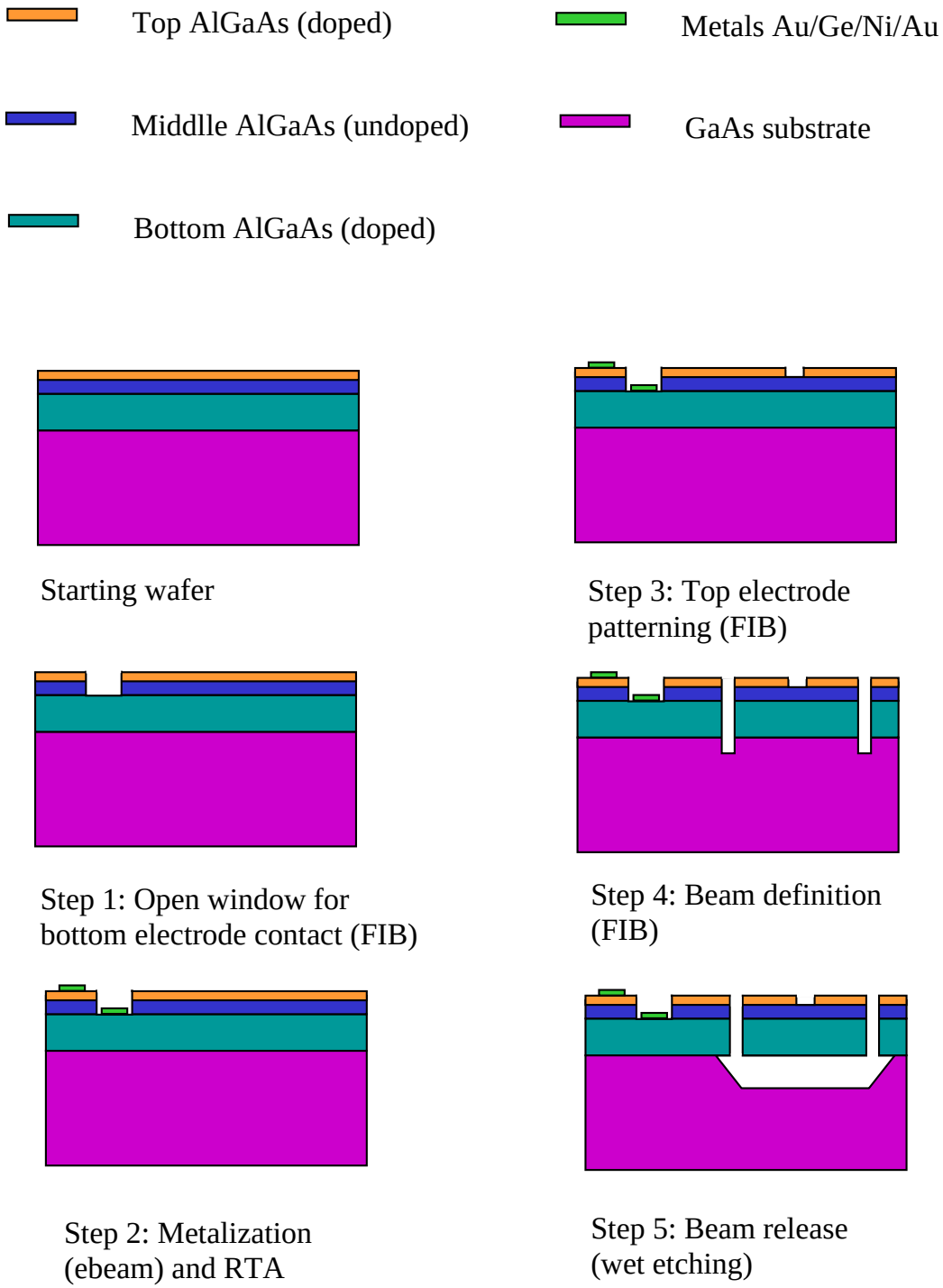

Figure 3.1: Fabrication process of resonators by GaAs sacrificial etching.

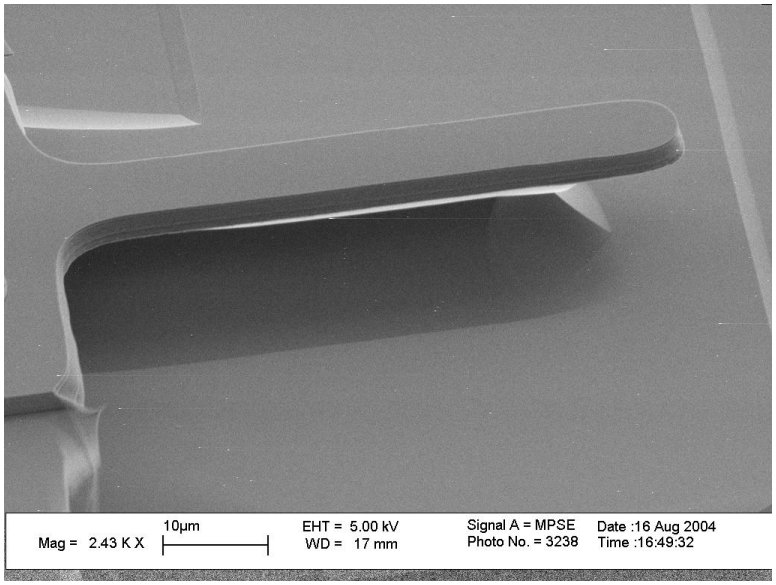

Figure 3.2: SEM image of a fabricated clamped-clamped beam resonator.

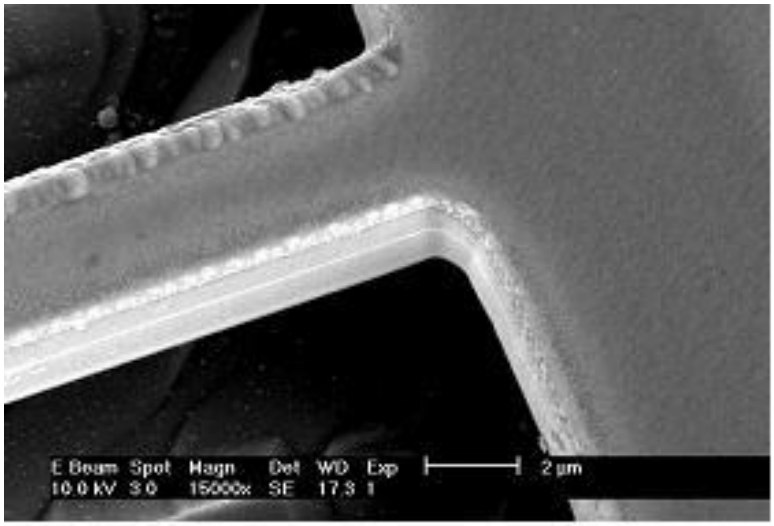

Figure 3.3: SEM picture of a beam fabricated by FIB/Wet etching release.

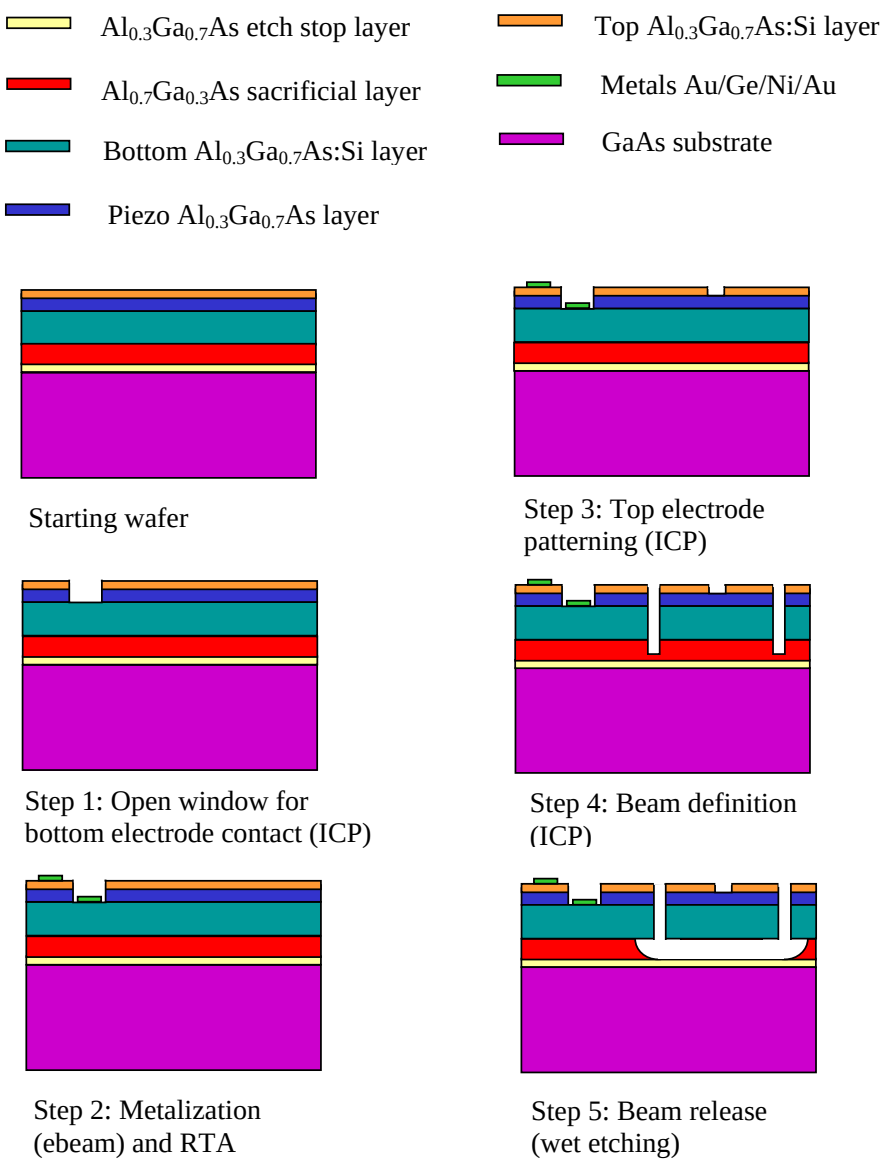

Figure 3.4: Fabrication process of resonators by $Al_{0.7}Ga_{0.3}As$ sacrificial etching.

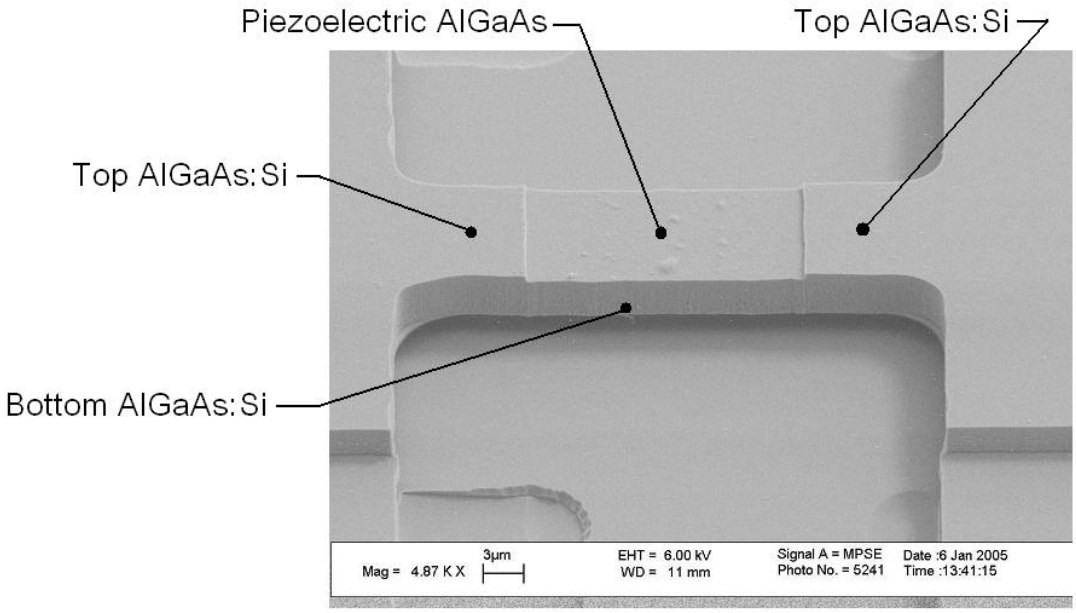

Figure 3.5: SEM image of fabricated clamped-clamped beam resonator.

Chapter 4

Design and Modeling of $Al_{0.3}Ga_{0.7}As$ Microresonators

The use of $Al_{0.3}Ga_{0.7}As$ as a piezoelectric material has received little attention in the literature. Thus, before designing and fabricating $Al_{0.3}Ga_{0.7}As$ based resonators, the piezoelectric properties of $Al_{0.3}Ga_{0.7}As$ were first evaluated to investigate the potential actuation and sensing modes, and effectiveness with respect to resonator orientation. Next, flexural mode resonators with various boundary conditions such as cantilever beam, clamped-clamped beam, and free-free beam resonators are analyzed and compared to simulated results obtained from finite element analysis. Finally, in-plane length-extensional mode resonators are introduced and their resonance frequencies and mode shapes are predicted by analytical mode and finite element analysis.

4.1 Piezoelectric Properties of $Al_{0.3}Ga_{0.7}As$

Piezoelectric materials generate an output voltage when subject to an input mechanical stress through the direct piezoelectric effect. Similarly, the material develops an output mechanical stress when an input electric voltage is applied across its surfaces by the converse piezoelectric effect. The linear constitutive relations between mechanical and electrical parameters are given by

$$S_1 = s_{11}^E T_1 + d_{31} E_3 \tag{4.1}$$

$$D_3 = d_{31}T_1 + \epsilon_{33}^T E_3 \tag{4.2}$$

where T_1 and S_1 are the mechanical stress and strain in x-axis respectively, E_3 and D_3 are electric field and electric displacement in the z-axis, s_{11}^E is the mechanical compliance at constant electric field, d_{31} is the piezoelectric linear coupling coefficient describing the relationship between electric field in the z-axis and strain in the x-axis, and ϵ_{33}^T is the permittivity of the piezoelectric element at constant stress.

For a (100) GaAs wafer, let the direction normal to (100) surface be the x_3 axis, let the $[0\bar{1}1]$ direction be the x_1 axis (ϕ=0), and let ϕ be a rotation of the coordination system around the x_3 axis. This gives [20]

$$d_{ik}(\phi) = \frac{d_{14}}{2}\begin{pmatrix} 0 & 0 & 0 & 2a_2 & -2b_2 & 0 \\ 0 & 0 & 0 & 2b_2 & -2a_2 & 0 \\ -b_2 & b_2 & 0 & 0 & 0 & 2a_2 \end{pmatrix} \tag{4.3}$$

where $-d_{14} = 2.69 \pm 1.13x\, pC/N$ for $Al_xGa_{1-x}As$, and $a_2 = \sin 2\phi$, and $b_2 = \cos 2\phi$. For the materials used in this project, the most natural way of applying an electric field is across the thickness of piezoelectric film, i.e., x_3 axis. For this reason, d_{3k} is the main parameter of concern. From the tensor form of d_{ik}, it is obvious that by adding voltage between top and bottom electrode layers, one can activate the flexural, longitudinal, as well as face shear mode vibration piezoelectrically. The electromechanical coupling factor d_{31} is shown in Fig. 4.1 to show the actuation effectiveness in each direction. Transduction is most efficient when the beam is along a $\langle 110 \rangle$ direction, i.e. $\phi = \frac{n\pi}{2}$, while there will be no transduction in the $\langle 100 \rangle$ direction, i.e. $\phi = \frac{n\pi}{2} + \frac{\pi}{4}$.

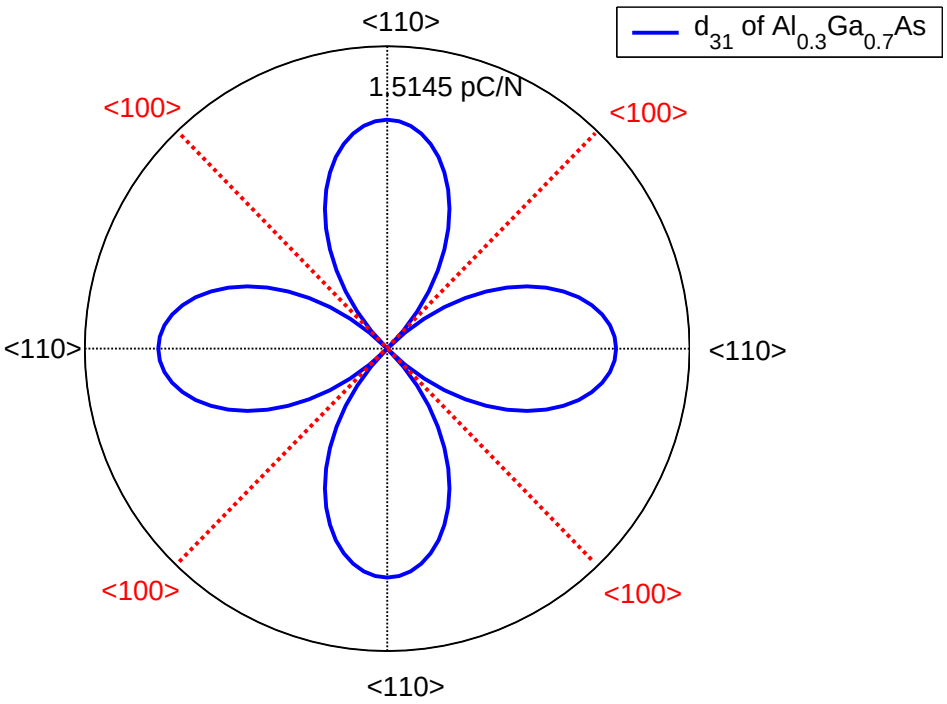

Figure 4.1: Theoretical d_{31} values of $Al_{0.3}Ga_{0.7}As$.

4.2 $Al_{0.3}Ga_{0.7}As$ Flexural Mode Resonators

Flexural vibration of resonators are widely used for low frequency resonators because they are relatively easy to implement and also can give a relatively large amplitude of vibration. To date, clamped-clamped beam resonators have been extensively exploited due to the relative ease of fabrication and ability to attain large frequency with same geometry compared to other beam designs such as cantilever beam resonators. However, for the case of clamped-clamped beam designs, larger stiffness often comes at the cost of increased anchor dissipation and, for this reason, lower resonator Q. As the beam dimension shrinks, i.e., when target frequency goes higher, this restriction limits the application of clamped-clamped resonators in filter

implementation area.

The free-free beam configuration offers as an alternative to clamped-clamped beam resonators at high frequency. Instead of anchoring the two ends of the resonator to the substrate directly like in clamped-clamped beam design, the free-free beam is supported by support beams at its node points, and the effects of energy loss throught the anchors are greatly suppressed. The support beams can operate in different modes, such as torsional or flexural modes. The mechanical impedance of the system is minimum when the resonance frequency of designed free-free beam matches with that of support beams, leading to maximum attainable Q factors.

4.2.1 Analytical Model of Flexural Mode Resonators

Consider a viscously damped beam resonator vibrating in the flexural mode with small transverse movements. When the beam is subject to an axial force of N, and a driving load of $P(x,t)$, the partial differential equation for flexural mode vibration of the beam is in the following form [21]

$$EI\frac{\partial^4 v(x,t)}{\partial x^4} - N\frac{\partial^2 v(x,t)}{\partial x^2} + \rho A\frac{\partial^2 v(x,t)}{\partial t^2} + c\frac{\partial v(x,t)}{\partial t} = P(x,t) \qquad (4.4)$$

where $v(x,t)$ is the transverse deflection of the beam, E the Young's modulus, I the moment of inertia, c the viscous damping parameter, ρ the density of the beam and A the cross-sectional area of the beam. By assuming that separation of space and time coordinates is possible, the resonance frequencies for beams with different

boundary conditions can be calculated by

$$f_i = \frac{\lambda_i^2}{2\pi L^2}\sqrt{\frac{Et^2}{12\rho}} \tag{4.5}$$

where λ_i is a function of boundary conditions, t is the thickness of the beam, L is the length of beam.

Material properties of $Al_{0.3}Ga_{0.7}As$ resonators are listed in table 4.1 [25]. The resonators are all in the plane of {100} in this work. In order to extract the theoretical resonance frequencies of resonators at different orientation, the Young's modulus in {100} need to be calculated first. The Young's modulus is given by [22]

$$\frac{1}{E} = S_{11} - 2(S_{11} - S_{12} - \frac{1}{2}S_{44})[\cos^2(\phi)\sin^2(\phi) + 1] \tag{4.6}$$

Where ϕ is the angle respect to $\langle 110 \rangle$ direction. Based on this equation, the Young's modulus in {100} plane is shown in Fig. 4.2. Listed in Fig. 4.3 is the calculated resonance frequency of flexural mode beam resonators in $\langle 110 \rangle$ direction with different beam lengths assuming the constructing materials of 2 μm $Al_{0.3}Ga_{0.7}As$: Si as bottom electrode layer, 1 μm $Al_{0.3}Ga_{0.7}As$ as piezoelectric layer, and 0.5 μm $Al_{0.3}Ga_{0.7}As$: Si as top electrode layer.

4.2.2 Finite Element Analysis of Flexural Mode Beam Resonators

Finite element analysis of flexural mode beam resonators was conducted to verify the analytical models using ANSYS 5.7.1. To simplify the problem, a 2-dimensional analysis was conducted for different boundary condition problems. The

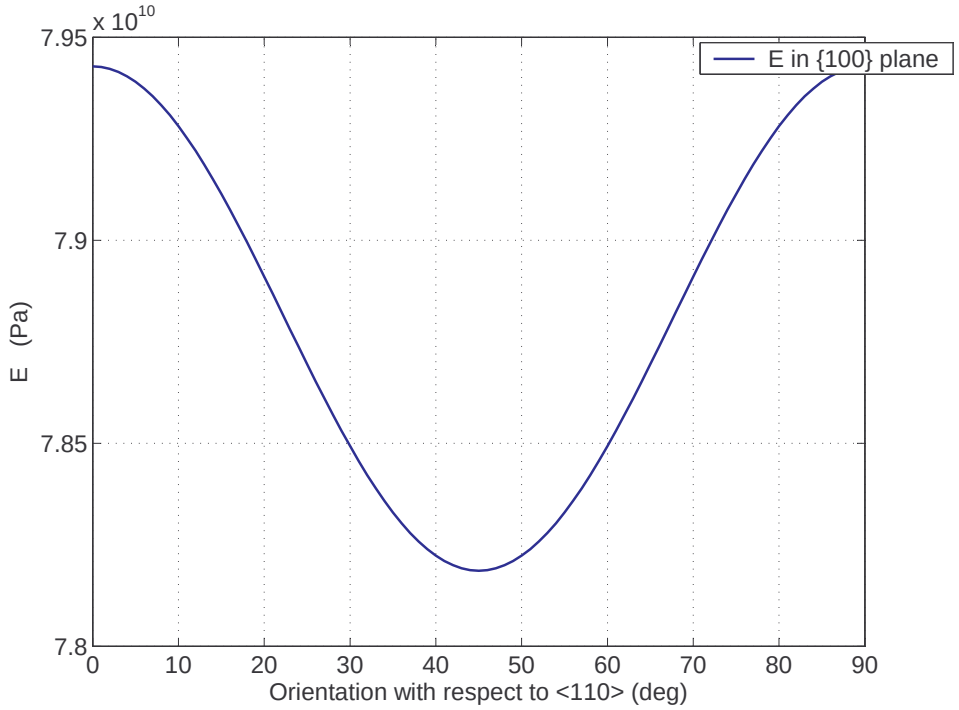

Figure 4.2: Young's modulus of $Al_{0.3}Ga_{0.7}As$ in $\{100\}$ plane.

plot shown in Fig. 4.4 shows excellent agreement between analytical model and ANSYS simulation results for all designs. The increased error between two methods at small beam length scale results from the failure of *Euler-Bernoulli* beam theory. To further verify the result of ANSYS simulation, the mode shape of each boundary condition case is extracted. Fig. 4.5–Fig. 4.7 show the simulated mode shapes of cantilever, clamped-clamped, and free-free beams, respectively.

Table 4.1: Material properties of $Al_{0.3}Ga_{0.7}As$.

Elastic stiffness constant C_{ij}	$C_{11} = 119.22$ GPa $C_{12} = 54.76$ GPa $C_{44} = 59.25$ GPa
Elastic compliance constant S_{ij}	$S_{11} = 1.179\times10^{-11}$ /Pa $S_{12} = 0.376\times10^{-11}$ /Pa $S_{44} = 1.686\times10^{-11}$ /Pa
Density	4.88×10^3 kg/m^3
Thermal expansion coefficient α_{th}	$6.04 \times 10^{-6}/^{\circ}C$
Dielectric constant ε	10.071

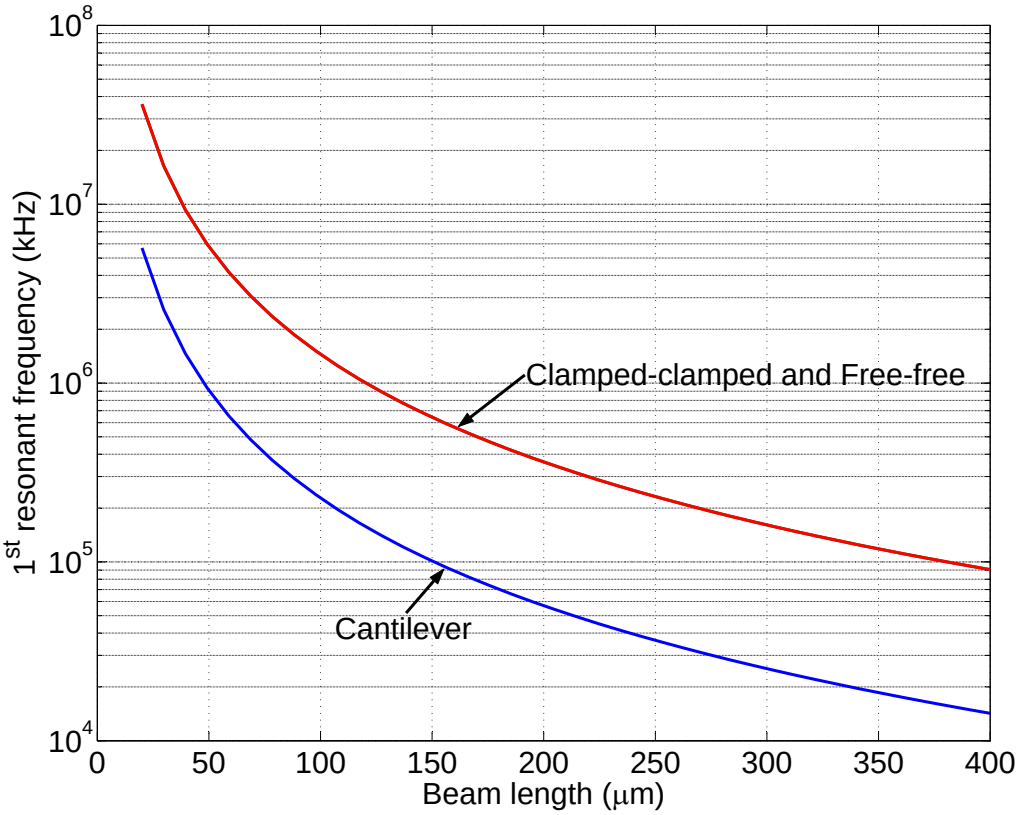

Figure 4.3: Resonance frequencies of flexural mode resonators.

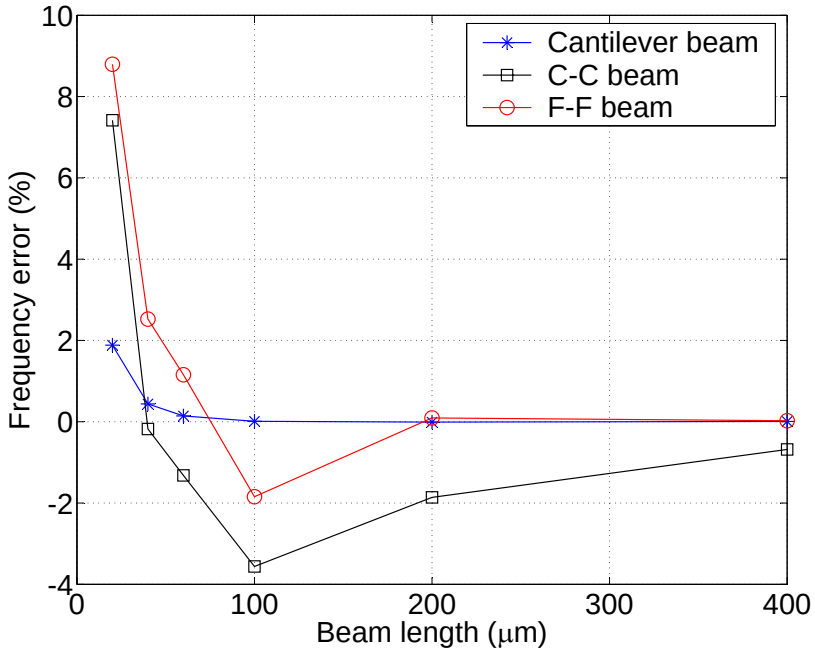

Figure 4.4: Frequency error between analytical model and ANSYS simulation.

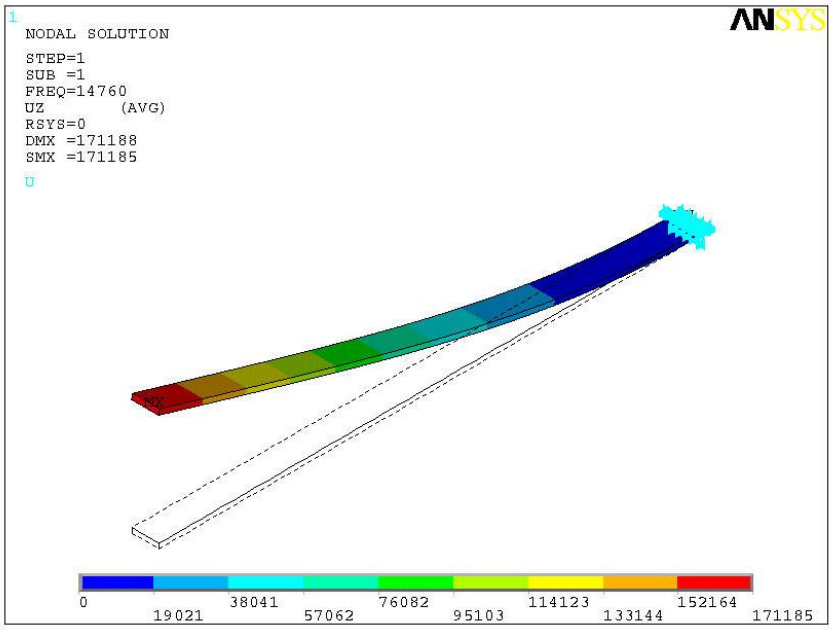

Figure 4.5: First mode shape of 400 μm long cantilever beam.

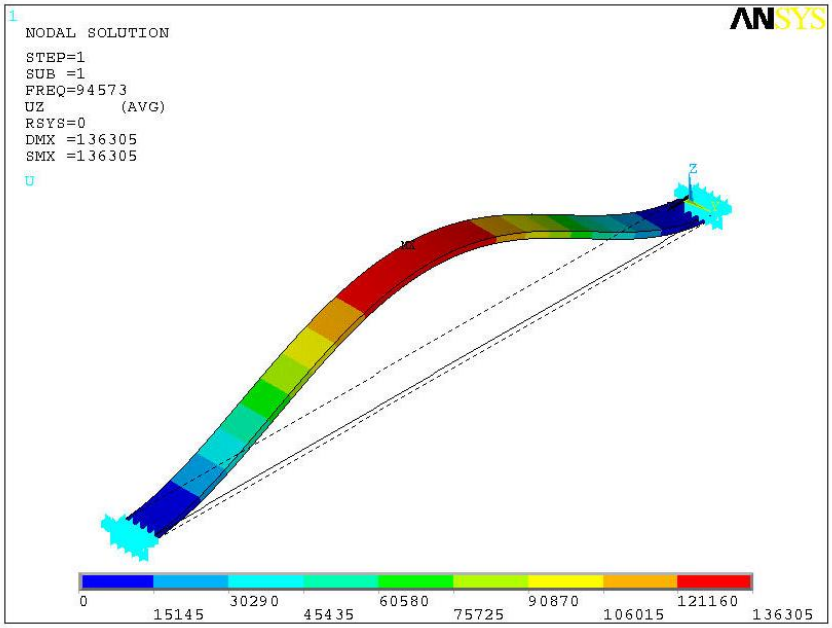

Figure 4.6: First mode shape of 400 μm long clamped-clamped beam.

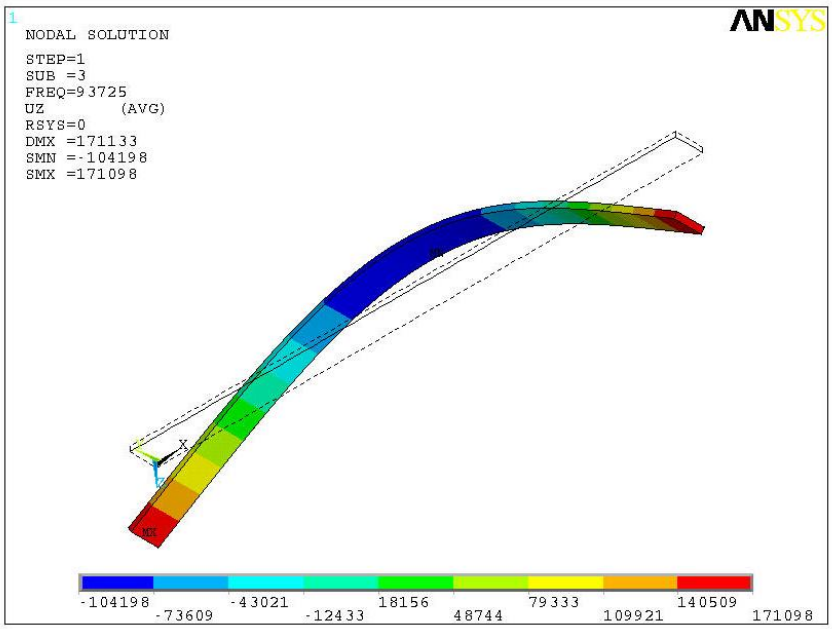

Figure 4.7: First mode shape of 400 μm long free-free beam.

4.3 In-Plane Length-Extensional Mode Resonators

Flexural mode resonators are relatively easy to implement and also can give a relatively high degree of vibration. The large amplitude of vibration will also result in a large degree of air damping if the flexural mode resonators are not operated under vacuum conditions. Also, the large degree of displacement in flexural mode resonators can result in nonlinear behavior which will limit the applicable driving voltage. For these reasons, flexural beam resonators must be placed in vacuum to achieve high quality factors, and the input voltage must be restricted to avoid nonlinearities, thereby reducing the achievable power handling.

In order to avoid the problem encountered by flexural mode resonators, in-plane length extensional mode resonators (bar resonators) were also developed in this work. The combination of small displacements, and shear damping mechanism in bar resonators (in contrast to squeeze film damping mechanism in flexural mode resonators) are expected to result in resonators with high attainable quality factors even in atmospheric pressure. Therefore, vacuum packaging of extensional mode resonators may not be necessary.

Consider an elastic bar of length L with uniform cross-sectional area of A. If $f(x,t)$ denotes the external force per unit length, $u(x,t)$ denotes the axial displacement, then the equation of motion for the forced longitudinal vibration of the bar can be

expressed as [21]

$$EA\frac{\partial^2 u}{\partial x^2}(x,t) + f(x,t) = \rho A\frac{\partial^2 u}{\partial t^2}(x,t) \tag{4.7}$$

The definition of E and ρ is the same as flexural mode resonators. Again, by assuming that separation of space and time coordinates is possible, the resonance frequency and mode shape can be extracted. Specifically, for bars with free-free boundary conditions, the resonance frequencies are given by

$$f_n = \frac{n}{L}\sqrt{\frac{E}{\rho}} \tag{4.8}$$

From this equation, it is clear that resonance frequency of bar resonators only depends on material properties and length of the beam structure. The immunity of resonance frequency to beam width and thickness is amenable to the control of resonance frequency in fabrication process. In order to verify the analytical model, ANSYS simulation of free-free bar resonators was conducted. Fig. 4.8 gives the comparison of theoretical and ANSYS simulated resonance frequencies of bar resonators. The deviation between theoretical and simulated results is less than 2% over the full range of frequencies. From the analytical model, the modal shape of bar resonators can be extracted. Fig. 4.9 and 4.10 gives the normalized 1^{st} and 3^{rd} mode shape together with corresponding strain. For reference, Fig. 4.11 and Fig. 4.12 gives the mode shape of a 400 μm long free-free bar resonator at 1^{st} and 3^{rd} resonance frequencies simulated by ANSYS.

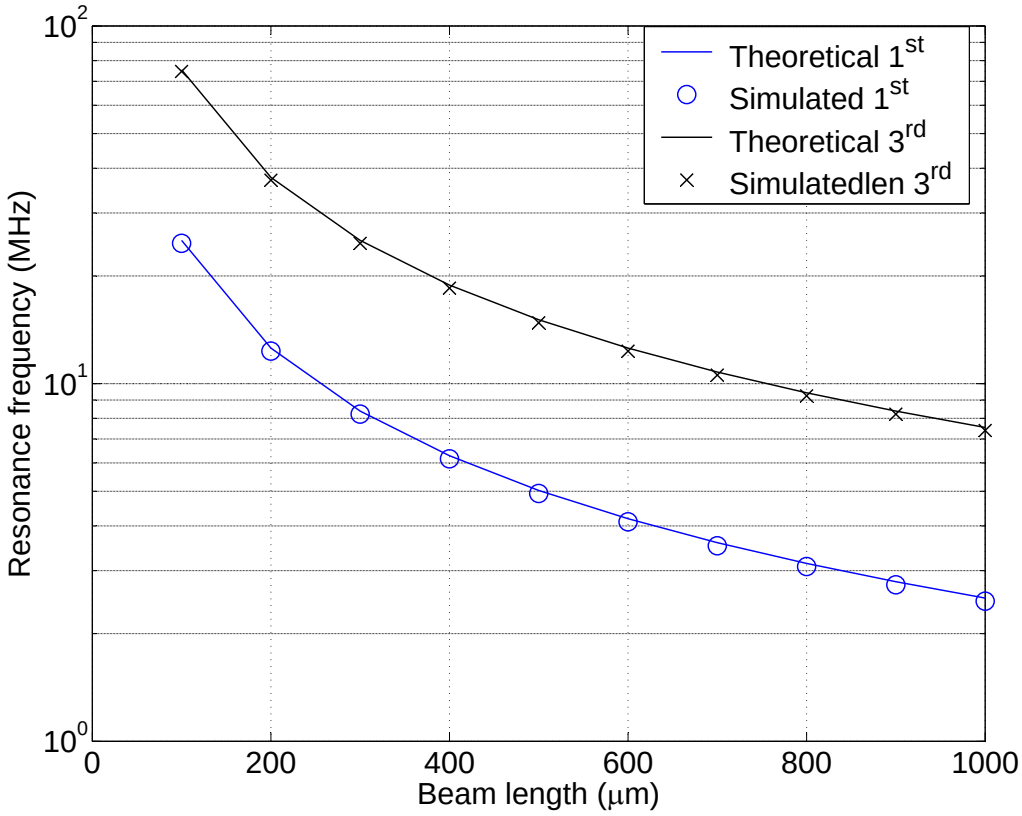

Figure 4.8: Theoretical and simulated resonance frequencies of free-free bar resonators.

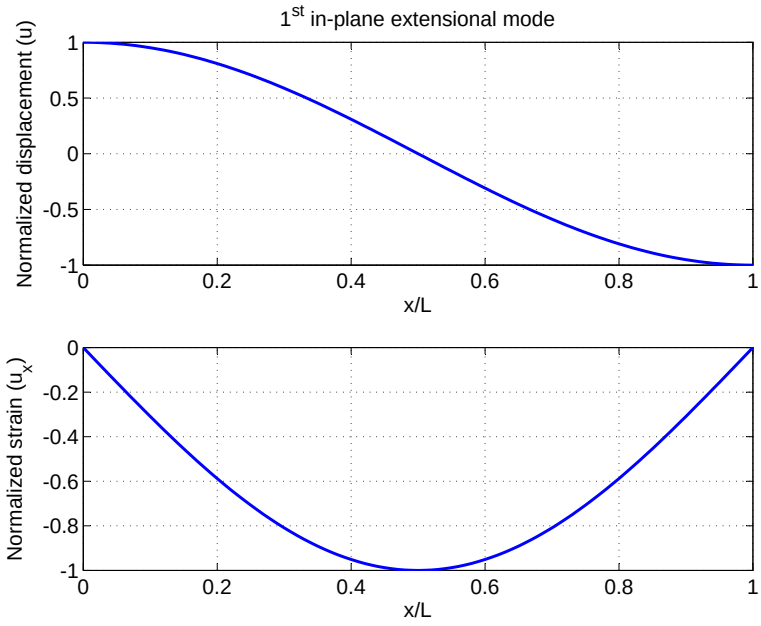

Figure 4.9: Displacement and strain of the resonator at 1^{st} extensional mode.

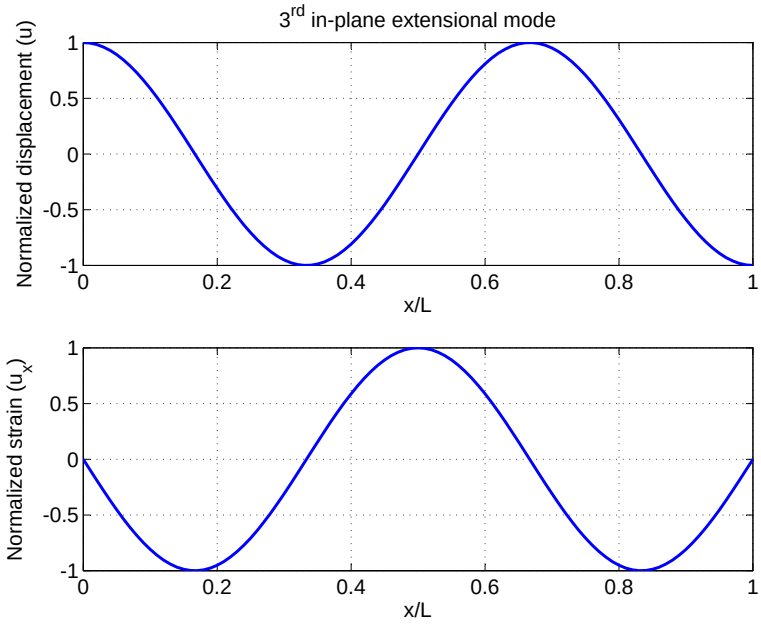

Figure 4.10: Displacement and strain of the resonator at 3^{rd} extensional mode.

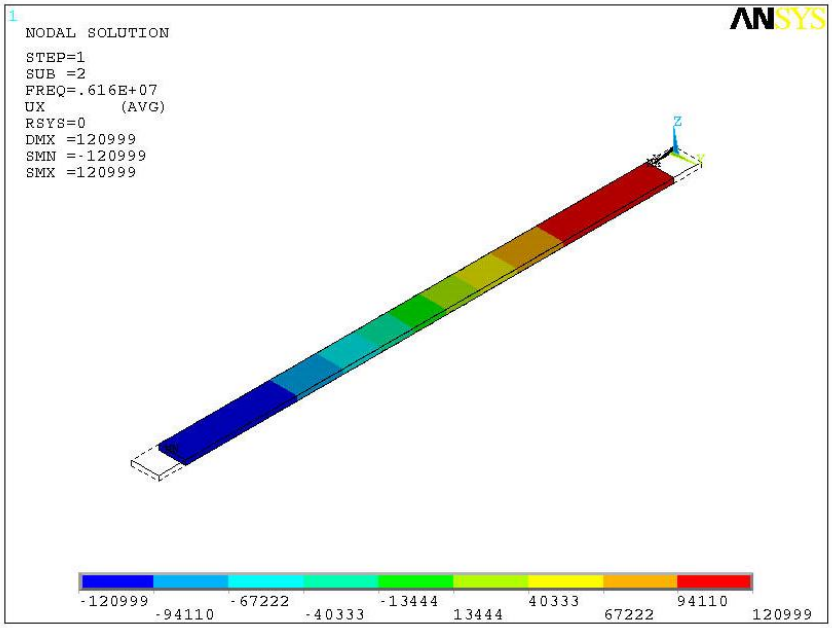

Figure 4.11: ANSYS simulated 1^{st} mode shape of a 400 μm f-f bar resonator.

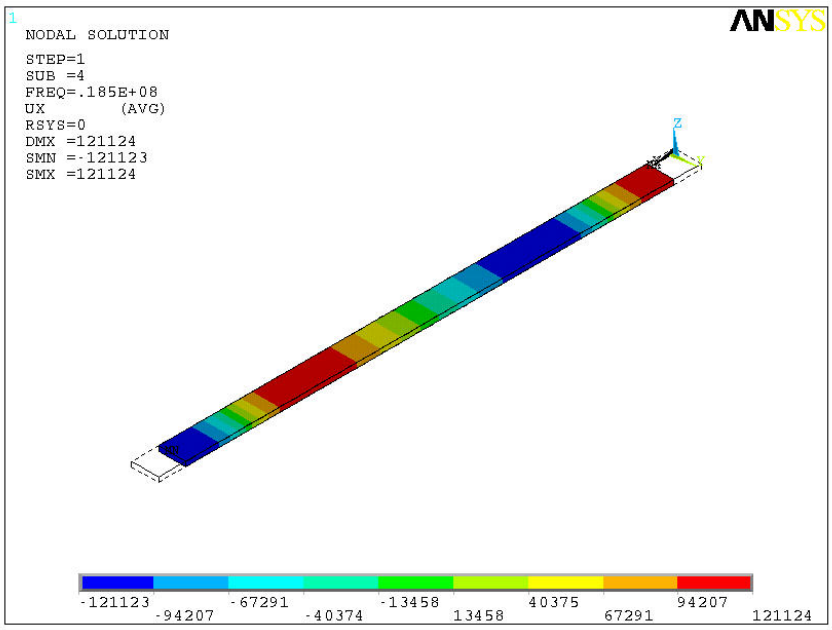

Figure 4.12: ANSYS simulated 3^{rd} mode shape of a 400 μm f-f bar resonator.

Fig. 4.13 shows a schematic of a length extensional mode free-free bar resonator. The resonator is supported at its center points by two support tethers. It is clear from the figure that all odd number of modes can be excited from the configuration given in Fig. 4.13. However, since the top electrode covers the full bar surface, the higher order vibration modes will produce an attenuated output because the charge output in different areas will partially cancel each other.

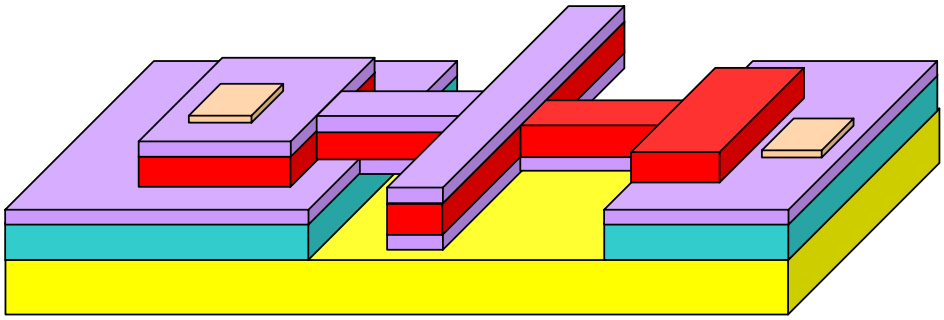

Figure 4.13: Schematics of length extensional mode resonators.

In order to avoid the flexural mode vibration, the top and bottom $Al_{0.3}Ga_{0.7}As$: Si layers have the same thickness, making the central line of piezoelectric layer coincide with the neutral line of the whole structure. A typical thickness configuration is 0.5 μm $Al_{0.3}Ga_{0.7}As$: Si as the bottom electrode layer, 4 μm $Al_{0.3}Ga_{0.7}As$ as the piezoelectric layer, and 0.5 μm $Al_{0.3}Ga_{0.7}As$: Si as the top electrode layer.

Chapter 5

Characterization Approaches

In this chapter, the experimental apparatus and characterization methods used for measuring the performance of fabricated piezoelectric resonators are presented. Two different methods, i.e. optical characterization and electrical characterization, are developed. Optical characterization based on laser Doppler vibrometry is suitable for flexural mode resonators with a frequency range of 2 MHz or below. For devices with higher center frequencies or in-plane vibration modes, direct electrical characterization is necessary. Three different configurations, namely electrical impedance analysis, charge amplification, and self sensing circuits were evaluated. Based on the unique properties of piezoelectric resonators developed in this project, a self sensing circuit topology was chosen to perform electrical characterization of fabricated resonators.

5.1 Optical Characterization by LDV

An optical measurement method, consisted of a single point laser Doppler vibrometer (LDV) mounted on a high magnification probe station and connected to a network analyzer (HP 4395A) was employed to characterize low frequency flexural mode resonators. The schematic setup for optical measurement is shown in Fig. 5.1.

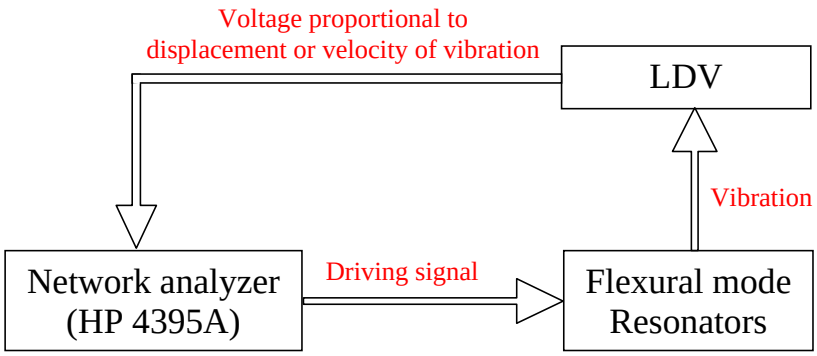

Figure 5.1: Schematics of optical measurement setup.

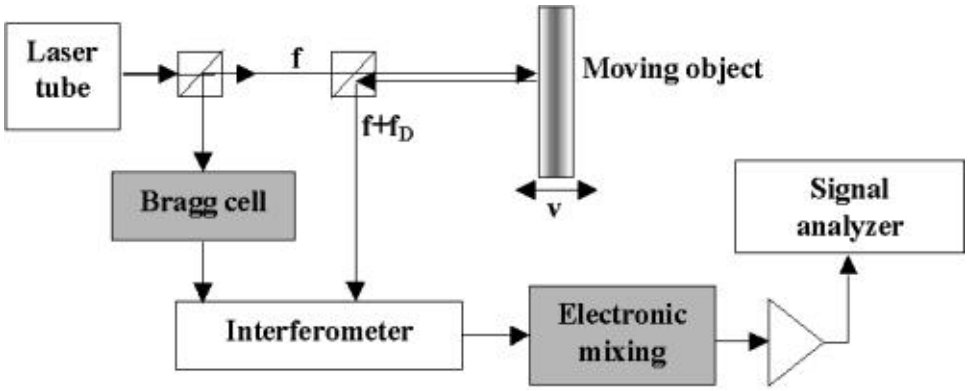

Figure 5.2: Schematics of LDV[32].

The key element in this setup is the LDV. which is an optical instrument employing laser interferometry to perform non-contact displacement and velocity measurement. The schematics of LDV is shown in Fig. 5.2.

Besides the merit of non-contact measurements, optical measurement based on LDV is also not affected by properties of the test surface and environmental conditions such as temperature or pressure. One important factor of LDV measurement is that

it is electrically inert and do not introduce mechanical artifacts. For this reason, one can easily determine whether the observed behavior is purely mechanical, purely electrical, or inherently electro-mechanical [31]. For flexural resonators with resonance frequencies smaller than 2 MHz, optical characterization yields stable results with high sensitivity.

The LDV employed in this work is OFV-511 fiber optic single point LDV from Polytec PI. This LDV is easy to work with probe station with integrated C-mount. The LDV is equipped with velocity and displacement decoder, and can provide output voltage proportional to either the displacement or the velocity of the vibration of the target. For the resonators developed in this work, the frequency range is normally beyond the frequency range of displacement decoder even for those low frequency resonators. Also, the vibration amplitude is often in the range of nanometer scale. For this reason, velocity output is often used instead of displacement output.

5.2 Electrical Characterization

Although, optical characterization showed a high resolution and stable results over frequency range up to 2 MHz, in order to characterize higher resonance frequency flexural mode resonators or non-flexural mode resonators, a true electrical characterization method must be explored.

5.2.1 Electrical Equivalent Circuit of $Al_{0.3}Ga_{0.7}As$ Resonators

Interfacing Piezo Film to Electronics

The first step of an interface circuit design is to understand the piezo film as a part of an electrical circuit. Fig. 5.3 shows a simplified equivalent circuit of piezo

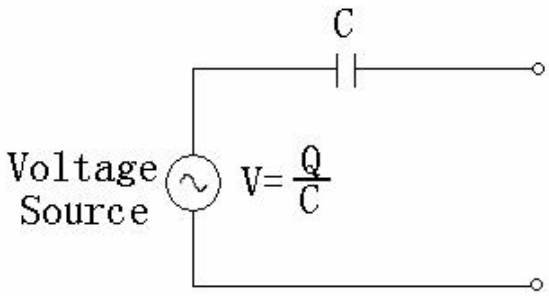

Figure 5.3: Simplified equivalent circuits of piezo film.

film. It consists of a series capacitance with a voltage source. The series capacitance represents piezo film capacitance, which is proportional to the active electrode area A and inversely proportional to the film thickness d and can be calculated by the following equation:

$$C_f = \frac{\varepsilon_r \varepsilon_0 A}{d} \tag{5.1}$$

Where ε_r is relative permittivity of the piezoelectric film. The voltage source amplitude is equal to the open circuit voltage of piezo film and inversely proportional to the piezo film capacitance. This simplified equivalent circuit is suitable for most applications but is of limited value for very high frequency applications.

Butterworth-Van Dyke-Dye's Model for Piezoelectric Resonators

The simplified equivalent circuit of piezo film is of limited use for the resonators near the resonance frequency. Instead, Butterworth-Van Dyke-Dye's model is used to develop electrical equivalent circuit of $Al_{0.3}Ga_{0.7}As$ resonators.

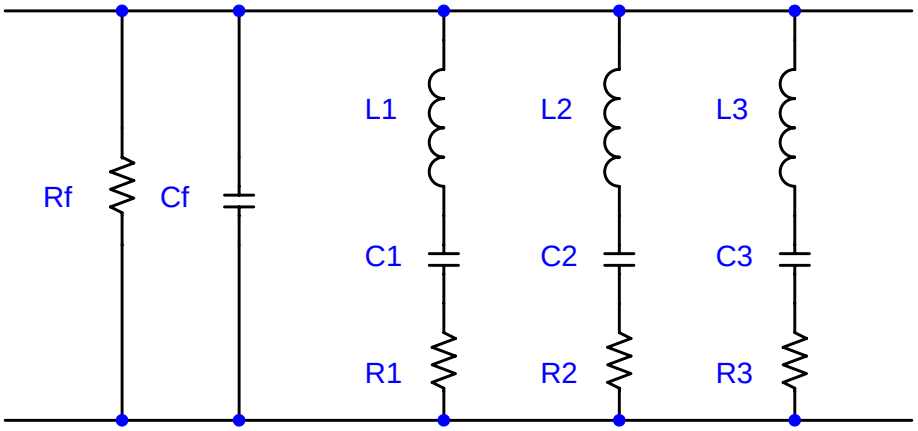

Figure 5.4: Equivalent circuits of resonators.

Fig. 5.4 shows the equivalent circuit of piezoelectric resonators. In this model, R_f and C_f represent the resistance and capacitance of piezo film. Each $R_nC_nL_n$ branch represents mechanical behavior of the resonator close to nth resonance frequency. Assuming pure second-order system behavior from a given resonance mode, the conductance between output current I_2 and input voltage V_1 near the modal resonance can be written as:

$$\frac{I_2(j\omega)}{V_1(j\omega)} = (j\omega)\frac{1}{M\omega_i^2(1-(\omega/\omega_i)^2 + j(\omega/\omega_i)(1/Q))}\eta^2 \tag{5.2}$$

Where M, Q, and ω_i are generalized mass, quality factor, and resonane frequency of the i^{th} mode respectively. By comparing this conductance with the conductance of $R_1L_1C_1$ branch which is given in eq. (5.3), one can obtain the values of circuit elements as

$$Y_1(j\omega) = \frac{j\omega C_1}{1 - \omega^2 L_1 C_1 + j\omega R_1 C_1} \tag{5.3}$$

$$C_1 = \frac{\eta^2}{K} \tag{5.4}$$

$$R_1 = \frac{\sqrt{KM}}{Q\eta^2} \tag{5.5}$$

$$L_1 = \frac{M}{\eta^2} \tag{5.6}$$

Here η stands for the electromechanical coupling factor, K stands for modal stiffness and can be calculated as

$$\eta = \frac{I(j\omega)}{j\omega X(j\omega)} \tag{5.7}$$

$$K = M\omega_1^2 \tag{5.8}$$

Where $I(j\omega)$ and $X(j\omega)$ is output current and modal displacement of the resonator respectively.

5.2.2 Impedance Analysis

The impedance change of piezoelectric resonators near resonance frequencies can act as a characteristic method for resonators. From equivalent circuit of piezoelectric resonators, the theoretical impedance curve for resonators near resonance frequencies can be obtained. Taking a 200 μm long 20 μm wide bar resonator with constructing material of 0.5 μm/ 4 μm/ 0.5 μm as an example, the simulated

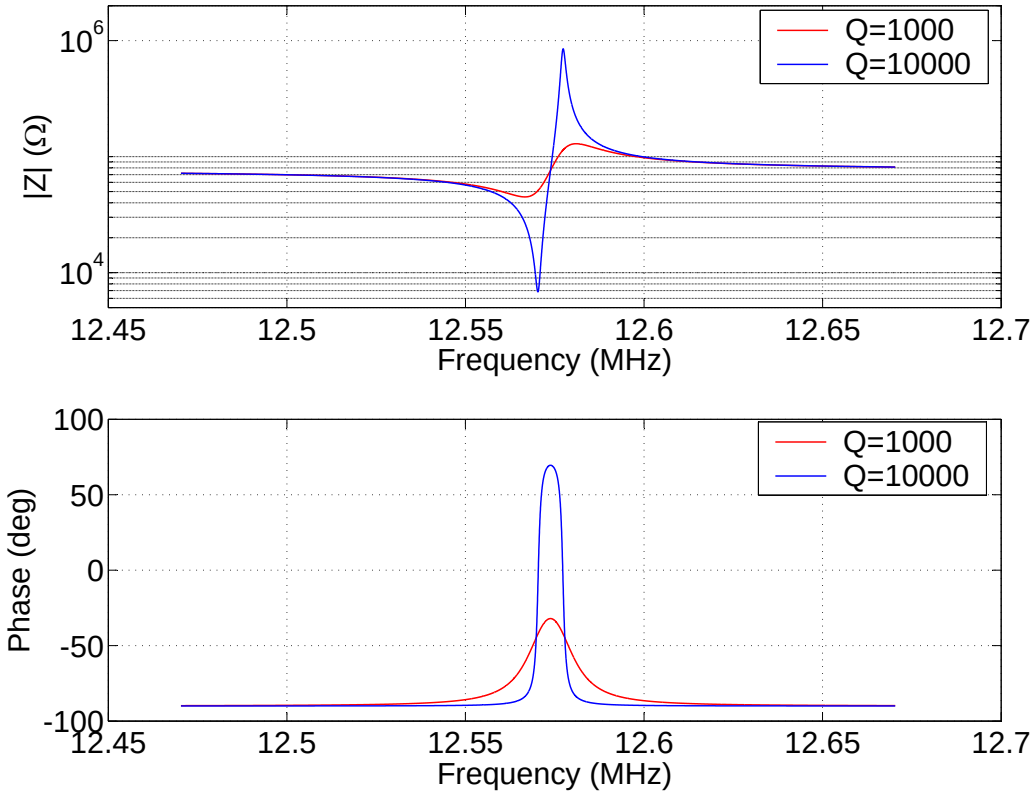

Figure 5.5: Theoretical impedance curve of a 200μm long bar resonator.

impedance curve near first resonance frequency is shown in Fig. 5.5. Two different measurement methods, namely RF I–V method and network analysis method is available for impedance measurement of developed resonators.

The network analysis method measures the reflection coefficient value of the unknown device and calculate the impedance of unknown device from the following equation:

$$Z_x = Z_0 \frac{1-\Gamma_x}{1+\Gamma_x} \quad (-1 \leq \Gamma \leq 1) \tag{5.9}$$

Where, Z_0 is the characteristic impedance of the measurement circuit (in this case, $Z_0 = 50\Omega$), and Z_x is impedance of unknown device. The measured value of Γ_x varies from -1 to +1 according tho the impedance value Z_x. If Z_x equals Z_0, there is no reflection, i.e., $\Gamma_x = 0$, if the unknown device is open or short circuit, the reflection coefficient is -1 or +1 respectively. The highest accuracy of impedance measurement is obtained when when Z_x equals Z_0. The accuracy of impedance measurement is decreased when Z_x is away from Z_0.

In contrast, the principle of RF I–V method is based on linear relationship between voltage and current. For this reason, the theoretical impedance measurement sensitivity is constant, regardless of measured impedance. Taking a resistive impedance as an example, the impedance measurement sensitivity of both methods is shown in Fig. 5.6. The simplified diagram for RF I–V method is given at Fig. 5.7. Compared to network analysis measurement method, RF I–V measurement provides better accuracy and wider impedance range.

Although, the impedance measurement method is straightforward and easy to implement, the impedance accuracy provided by Impedance analyzer is from 2 Ω to 5 kΩ. The estimated impedance of fabricated resonator near resonance frequency is beyond this range. Therefore, impedance measurement can not be used as a characterizing method in this project.

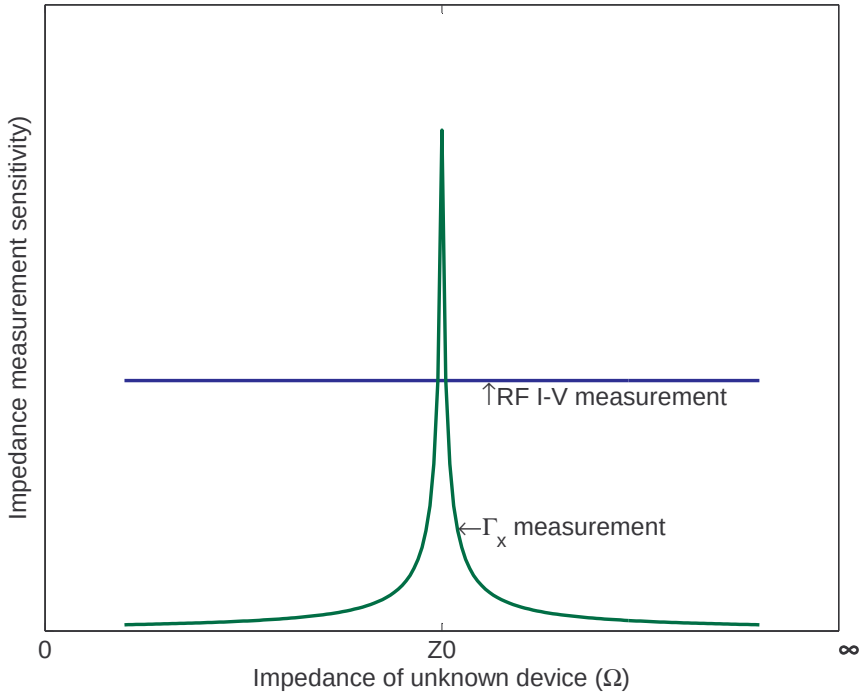

Figure 5.6: Impedance sensitivity of both methods.

5.2.3 Charge Amplifier

Charge amplifier produce an output voltage that is proportional to the charge input. Fig. 5.8 shows an equivalent circuit for a piezoelectric resonator connected to a charge amplifier. Where

Q_r = Charge generated by piezoelectric film

R_r = Resistance or resonator

C_r = Capacitance of resonator

R_f = Feedback resistance

C_f = Freedback capacitance

V_{out} = Voltage output of the charge amplifier

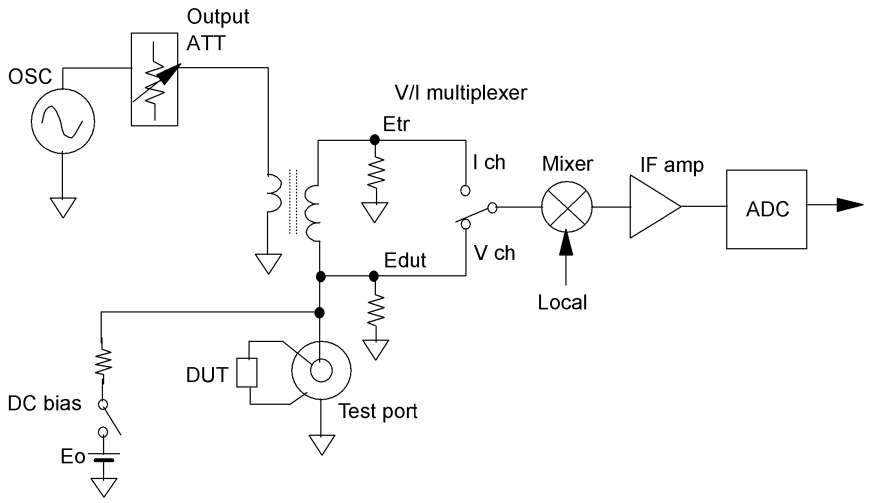

Figure 5.7: Block diagram of RF I–V method [35].

The output voltage is dependent on the ratio of the input charge to the feedback capacitance as shown in Equation (5.10). Note that the capacitance due to the sensor, cable, and amplifier do not affect the system sensitivity, major advantage of charge amplifier.

$$V_{out} = \frac{Q_r}{C_f} \tag{5.10}$$

Although, the cable capacitance does not affect the system sensitivity, low noise, shielded cable should be used to reduce charge generated by cable motion and to reduce electrical noise induced by RFI and EMI.

The high cutoff frequency of charge amplifier must be set to higher than resonance

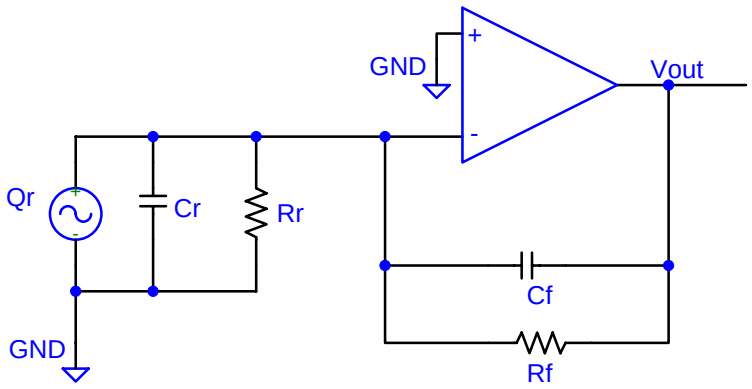

Figure 5.8: Schematics of charge amplifier circuit.

frequency of resonator and is defined by the following equation.

$$f_h = GB \times \frac{C_f}{C_r} \tag{5.11}$$

For the resonators developed in this project, the moderate electromechanical coupling factor together with the parasitic capacitance will prohibit us from getting a good signal out of charge amplifier. A typical output from the charge amplifier connected with a clamped–clamped beam resonator is shown in Fig. 5.9.

5.2.4 Self-Sensing Circuit [36]

Fig. 5.10 shows schematics of the so called self-sensing actuator (SSA) circuit. In this figure, C_p represents the capacitance of piezoelectric film, and voltage V_p represents the voltage output generated from the strain of the beam. When $C_m = C_p$, we can get

$$V_1 - V_2 = \frac{C_p}{C_p + C_r} V_p \tag{5.12}$$

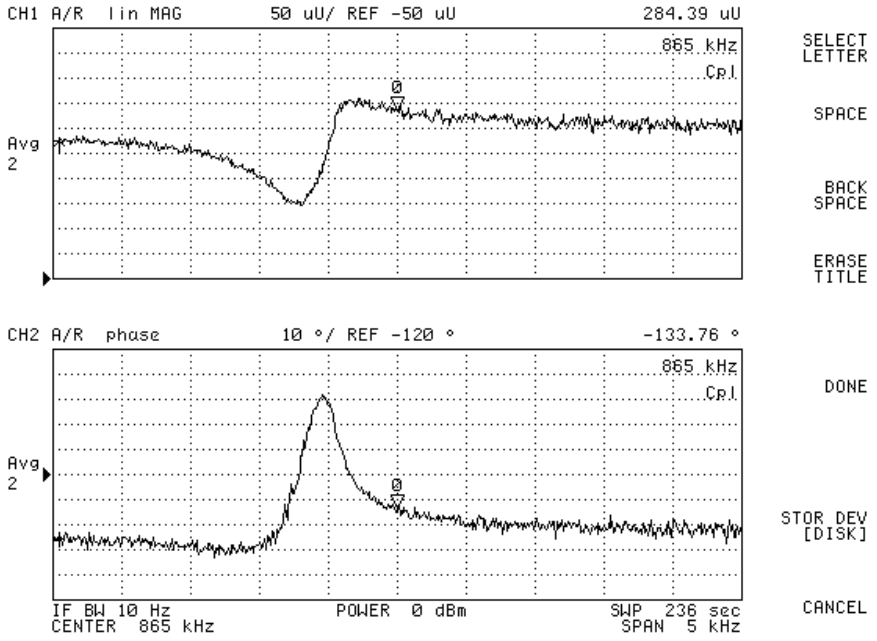

Figure 5.9: Output of charge amplifier connected to a 120 μm C–C beam.

For the initial implementation, the capacitors used in SSA are all discrete devices. In order to get an exact matching of capacitance in eq. (5.12), the capacitor C_m in Fig. 5.10 is fabricated on chip with similar geometrical size to the measured resonator to have a better control over the capacitance values. In self sensing circuit, the piezoelectric film is performing dual function of sensing and actuation. Self-sensing circuit can be used to characterize one port resonators such as cantilever resonators or one port longitudinal bar resonators. With the self sensing circuit design, the problems associated with parasitic capacitance can be alleviated to some extent. Therefore, the self-sensing circuit was chosen as the primary electrical characterization method in this project.

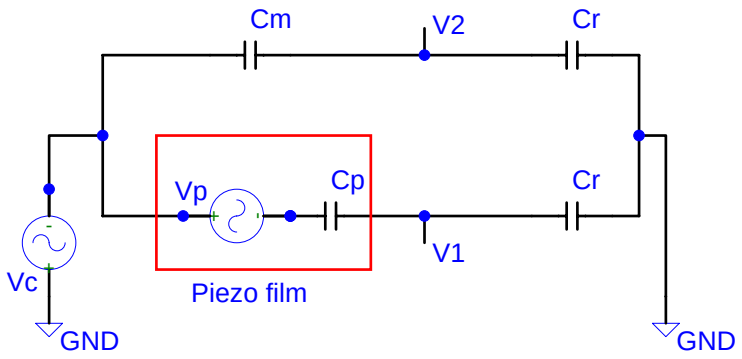

Figure 5.10: Schematics of self-sensing circuit.

In order to accommodate the impedance mismatch due to variations between each component in the self-sensing circuit, a potentiometer is used as one of the feedback resistors in the following differential amplifier. The schematic of the differential voltage amplifier is shown in Fig. 5.11. The selected operational amplifier (AD8138 from Analog Devices) features a large input impedance with high common-mode rejection ratio (CMRR) for best performance of the circuit. Fig. 5.12 gives the frequency response of the self sensing circuit with a 3 dB bandwidth of around 70 MHz. The effect of impedance mismatch is clearly shown in Fig. 5.13 for the case of testing a 200 μm long bar resonator.

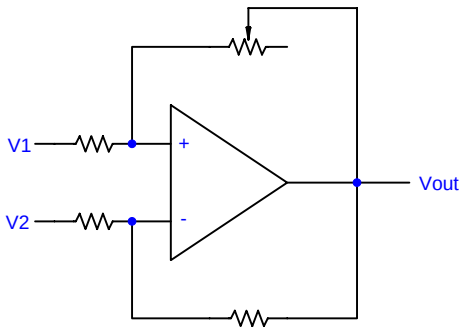

Figure 5.11: Schematics of differential voltage amplifier.

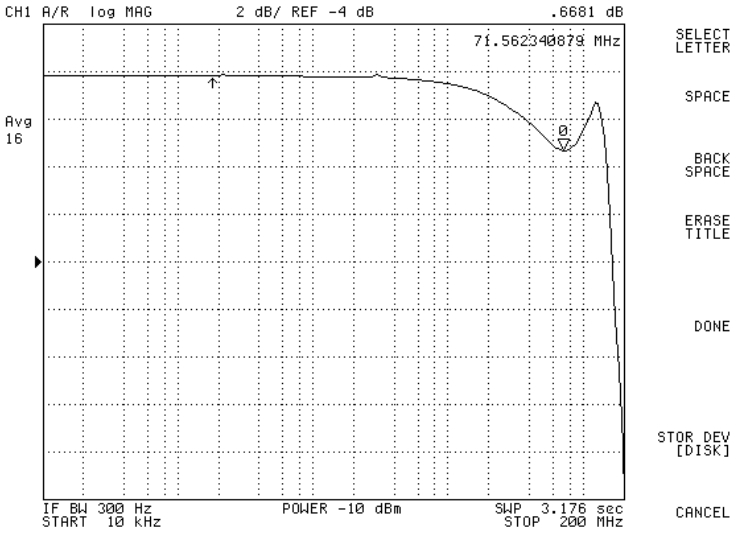

Figure 5.12: Frequency response of self sensing circuit.

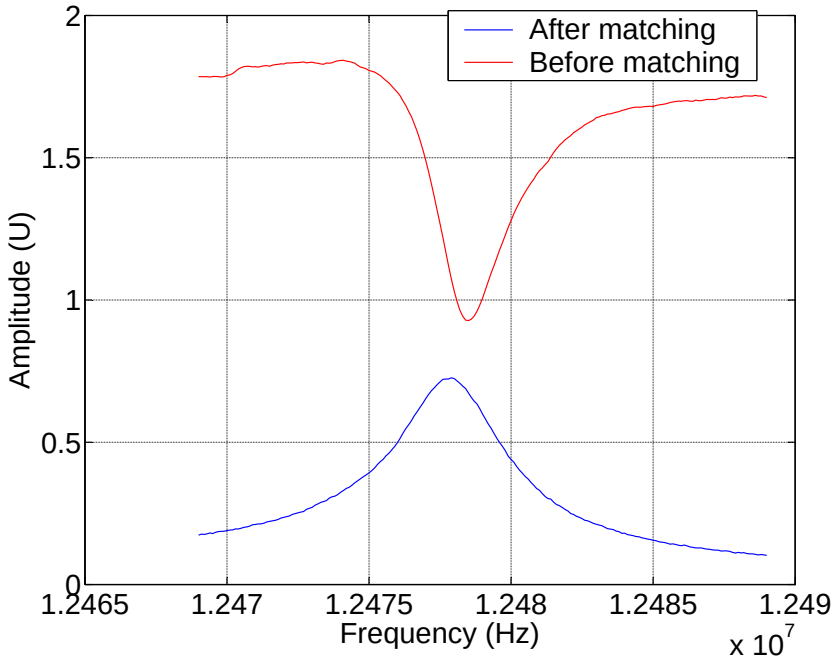

Figure 5.13: Output of self sensing circuit before/after impedance matching.

Chapter 6

Unimorph Flexural Mode Resonator Characterization Results

In this chapter, the results from developed flexural mode resonators are presented. First, the d_{31} values of $Al_{0.3}Ga_{0.7}As$ in different orientations are calculated by quasi-static deflection measurement of cantilever beam and resonance curve matching of clamped-clamped beam. Both results showed good matching to theoretical predictions. Next, measurement results of cantilever beam, clamped-clamped beam, and free-free beam resonators including resonance frequency, quality factors, linearity, and temperature stability are provided.

6.1 Extraction of $Al_{0.3}Ga_{0.7}As$ Film d_{31} Values from Low Frequency Resonators

Although, the d_{31} values for bulk $Al_{0.3}Ga_{0.7}As$ material has been reported, the d_{31} values of thin film $Al_{0.3}Ga_{0.7}As$ at different orientations are still remained a question. The quasi-static and dynamic response of developed low frequency flexural mode resonators provided a method of characterizing d_{31} values in different angles.

6.1.1 d_{31} Values from Quasi-Static Measurement

The quasi-static deflections of cantilever beams have been investigated in order to extract the d_{31} values at different orientations. The calculation of d_{31} values

was performed from measured quasi-static deflections of cantilever beams combined with an analytic model for the quasi-static response of multilayer piezoelectric microactuators [34]. Consider a uniform width cantilever beam consisted of m different layers. By employing the principle of static equilibrium and strain compatibility, the deflection of the cantilever beam as a function of distance from the anchor point x can be computed as

$$\delta(x) = \frac{x^2}{2r} = x^2 \left[\frac{d_{31}\mathbf{D}\mathbf{A}^{-1}\mathbf{C}}{2 - \mathbf{D}\mathbf{A}^{-1}\mathbf{B}} \right] \tag{6.1}$$

Where r stands for radius of curvature, **A, B, C, D** are matrices and can be expressed as

$$\mathbf{A} = \begin{bmatrix} \frac{1}{A_1E_1} & \frac{-1}{A_2E_2} & 0 & \cdots & 0 \\ 0 & \frac{1}{A_2E_2} & \frac{-1}{A_3E_3} & 0 & \cdots \\ \cdots & 0 & \cdots & \cdots & 0 \\ 0 & \cdots & 0 & \frac{1}{A_{m-1}E_{m-1}} & \frac{-1}{A_mE_m} \\ 1 & 1 & \cdots & 1 & 1 \end{bmatrix} \tag{6.2}$$

$$\mathbf{B} = \begin{bmatrix} t_1 & + & t_2 \\ t_2 & + & t_3 \\ & \cdots & \\ t_{m-1} & + & t_m \\ & 0 & \end{bmatrix} \tag{6.3}$$

$$\mathbf{C} = \begin{bmatrix} \mathbf{E}_2 & - & \mathbf{E}_1 \\ \mathbf{E}_3 & - & \mathbf{E}_2 \\ & \cdots & \\ \mathbf{E}_m & - & \mathbf{E}_{m-1} \\ & 0 & \end{bmatrix} \tag{6.4}$$

$$\mathbf{D} = \frac{1}{\sum_{i=1}^{m} E_i I_i} \left[\left(\frac{t_1}{2}\right) \left(t_1 + \frac{t_2}{2}\right) \cdots \left(\sum_{i=1}^{m-1} t_i + \frac{t_m}{2}\right) \right] \tag{6.5}$$

Where A_i, E_i, t_i, I_i is cross sectional area, Young's modulus, thickness and moment of inertia of ith layer, and $\mathbf{E}_i$ is the electrical field applied to ith layer. A sinusoical voltage signal with a fixed frequency is generated by a function generator and added to the electrode layers of cantilevers to stimulate quasi-static vibration of the cantilevers. The displacement at the tip of cantilevers are measured by LDV and used to calculate the d_{31} factors of piezoelectric $Al_{0.3}Ga_{0.7}As$ film.

6.1.2 d_{31} Values from Resonance Matching

Another approach conducted to extract d_{31} values of $Al_{0.3}Ga_{0.7}As$ film is resonance matching. In this method, d_{31} values are calculated by matching the measured resonance curves of resonators with the theoretical predictions. For the works presented here, the resonators used is clamped-clamped beam resonators with constructing material of 2 μm $Al_{0.3}Ga_{0.7}As$: Si as bottom electrode layer, 1 μm $Al_{0.3}Ga_{0.7}As$ as piezoelectric layer, and 0.5 μm $Al_{0.3}Ga_{0.7}As$: Si as top electrode layer. The top electrode is clipped at quarter length of the beam on both sides to get a maximum driving moment. The clamped-clamped beams are oriented from

15° to 45° with respect to ⟨110⟩ direction per the restriction imposed by GaAs sacrificial wet etching release step. The output from the LDV is proportional to the velocity of the beam vibration. The transfer function between the driving voltage V1 and the output voltage from LDV V2 is given by [8]

$$T(j\omega) = \frac{V2(j\omega)}{V1(j\omega)} = kj\omega\frac{Z(j\omega)}{V1(j\omega)} \tag{6.6}$$

Where k is the sensitivity of LDV, $Z(j\omega)$ is generalized beam displacement. If we denote $F(j\omega)$ as the mechanical force, then the transfer function can be expressed as

$$T(j\omega) = kj\omega\frac{Z(j\omega)}{F(j\omega)}\frac{F(j\omega)}{V1(j\omega)} \tag{6.7}$$

The fist term in eq. (6.7) is the term describing the force–displacement transfer function of the clamped-clamped beam. By assuming linear second order behavior, this term can be written as

$$\frac{Z(j\omega)}{F(j\omega)} = \frac{1}{M\omega_1^2\left[1-(\omega/\omega_1)^2 + j(\omega/\omega_1)(1/Q)\right]} \tag{6.8}$$

Where M, Q, and ω_1 are generalized mass, quality factor, and resonance frequency respectively. Assuming a clamped-clamped beam with dimension of length L, width b, thickness h, the generalized mass M can be calculated as

$$M = \int_0^L \rho bh\phi^2(x)dx \cong 1.036\rho bhL \tag{6.9}$$

Where ρ is material density, and $\phi(x)$ is the mode shape function for clamped-clamped beam, and can be expressed as

$$\phi(x) = \sinh(\beta x) - \sin(\beta x) + \alpha[\cosh(\beta x) - \cos(\beta x)] \tag{6.10}$$

In eq. (6.10), βL and α are constants for clamped-clamped beam and are given by $\beta L = 4.73$ and $\alpha = -1.018$ for the first resonance mode.

The second term in eq. (6.7) is electromechanical coupling factor for the drive electrode and can be calculated as [8]

$$\frac{F(j\omega)}{V1(j\omega)} = \frac{d_{31} E h_e}{2} \int_0^l b_1''(x)\phi(x)dx \tag{6.11}$$

Where E is Young's modulus, h_e is the distance between the center plane of piezoelectric layer and neutral axis of the beam. For the case of quarter length clipped clamped-clamped beam, the following equation stands.

$$\int_0^l b_1''(x)\phi(x)dx = \frac{-4.92b}{L} \tag{6.12}$$

Therefore, the second term in eq. (6.7) can be written as

$$\frac{F(j\omega)}{V1(j\omega)} = \frac{-2.46 d_{31} E h_e b}{L} \tag{6.13}$$

The overall transfer function $T(j\omega)$ becomes

$$T(j\omega) = \frac{-j\omega k d_{31} E h_e b/L}{M\omega_1^2 \left[1 - (\omega/\omega_1)^2 + j(\omega/\omega_1)(1/Q)\right]} \tag{6.14}$$

The value of ω_1 and Q can be obtained by measurement, other parameters except for d_{31} are known. Therefore, by comparing the theoretical resonance curve with the measured curve, one can obtain the electromechanical coupling factor, in this case d_{31}. As an example, Fig. 6.1 gives the frequency response of optical measurement and matched curve.

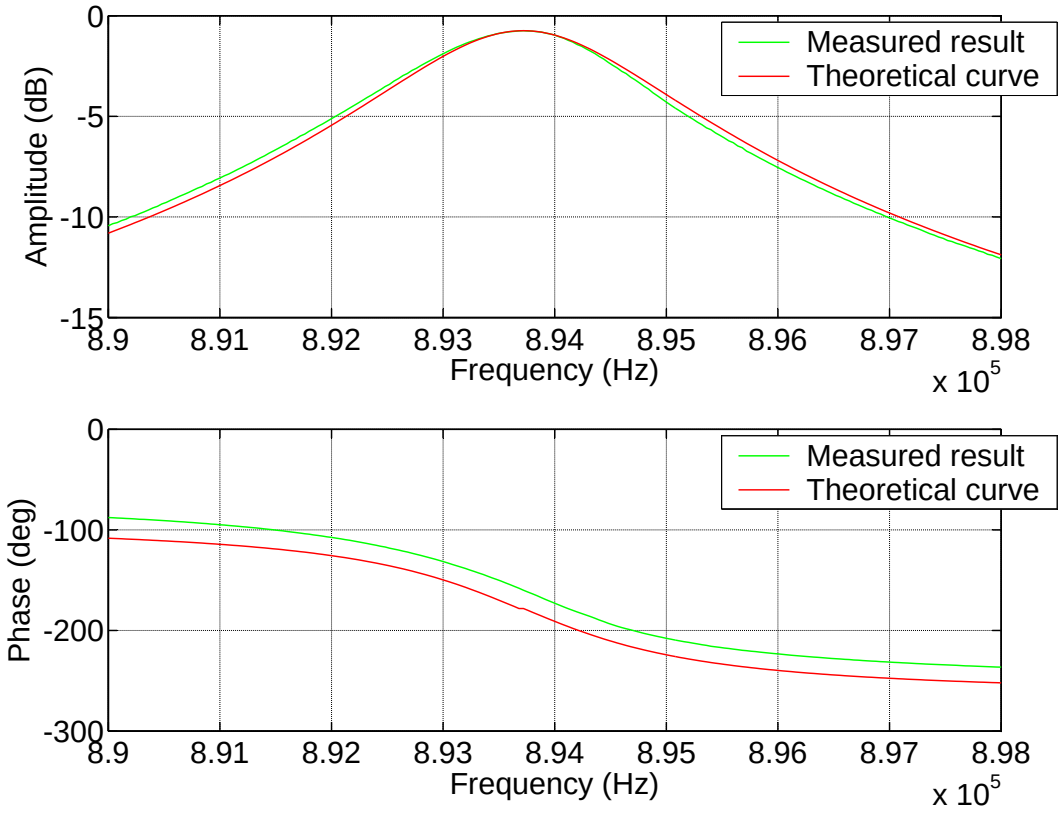

Figure 6.1: Theoretical and measured frequency response of a 400 μm long c-c beam.

6.1.3 d_{31} Measurement Results

Fig. 6.2 summarizes the theoretical and measured d_{31} values at different orientations by both methods. Although slightly different from theoretical predictions, the measured values compare favorably with the theoretical bulk value.

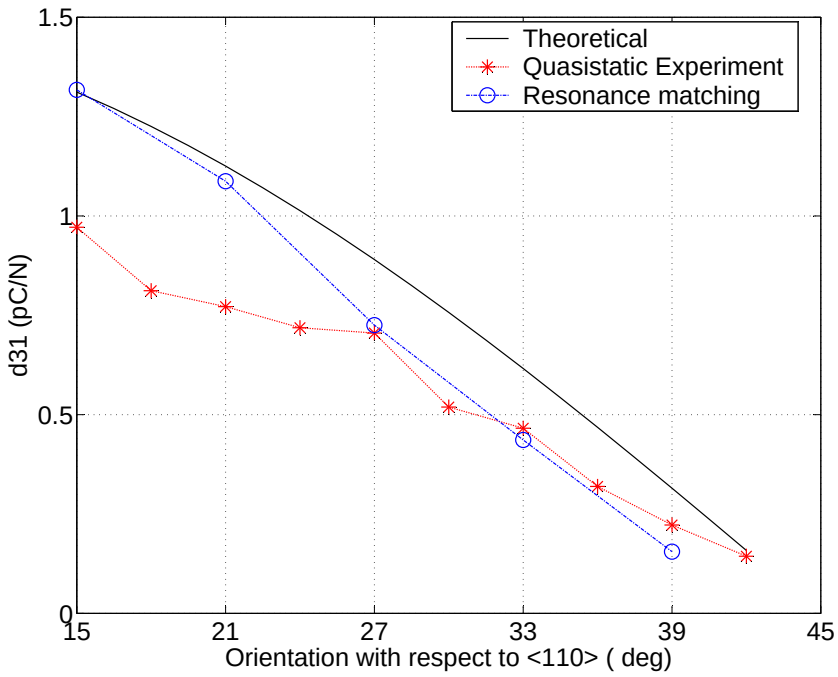

Figure 6.2: d_{31} values at different orientations.

6.2 Unimorph Cantilever Beam Resonators

Low frequency unimorph flexural mode cantilever resonators are developed with constructing material of 0.5 μm $Al_{0.3}Ga_{0.7}As$: Si/ 1 μm $Al_{0.3}Ga_{0.7}As$/ 2 μm $Al_{0.3}Ga_{0.7}As$: Si. The developed cantilever resonators have resonance frequencies smaller than 2 MHz. Therefore, optical characterization is conducted for the measurement task.

6.2.1 Resonance Frequency

The resonance frequency of cantilever resonators are measured by LDV combined with network analyzer and compared with theoretical predictions. Fig. 6.3 gives the results of measured resonance frequencies of cantilevers at atmospheric pressure in comparison with theoretical values.

In general, the measured resonance frequencies showed a good matching to theoretical predictions for those beams with length larger than 100 μm. For those beams with smaller lengths, the discrepancy between measured values and theory can be explained by the failure of *Euler-Bernoulli* beam equation.

6.2.2 Dynamic Response

The dynamic responses of cantilever resonators are measured by LDV. Fig. 6.4 gives the frequency response of a 100 μm long cantilever beam resonator at atmospheric pressure near the resonance frequency. In comparison, Fig. 6.5 gives the

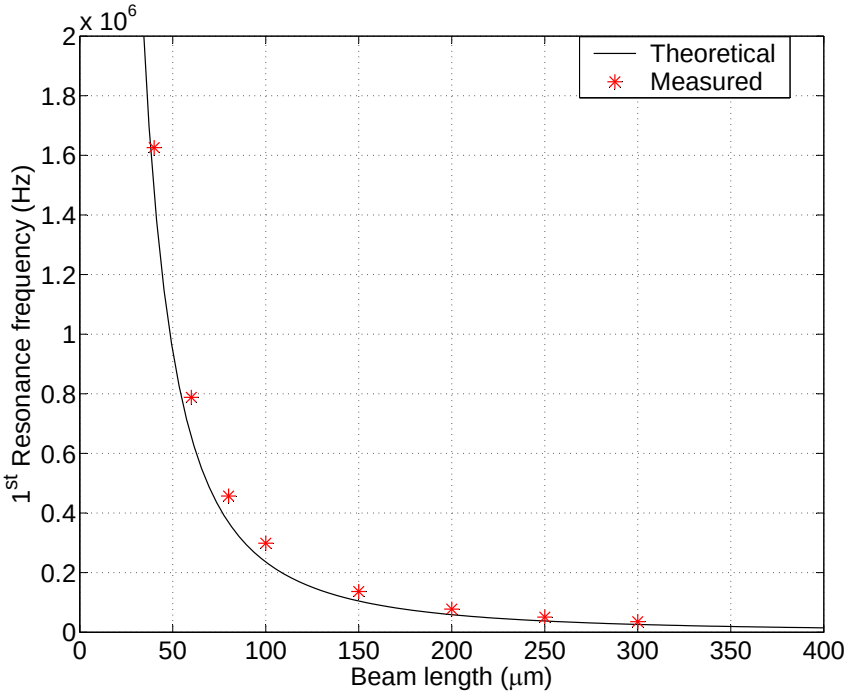

Figure 6.3: Theoretical and experimental resonance frequencies of cantilever beams.

measured dynamic response of the same resonator at vacuum to exclude the effect of air damping. As evident from the figures, the resonance displacement amplitude at vacuum is about 6.5 times of that in 1 atm, and quality factor showed an increase from 105 at 1 atm to 2,064 in vacuum.

The quality factors of developed cantilever beam resonators have been measured and results are shown in Fig. 6.6. At atmospheric pressure, air damping is a dominant factor defining attainable quality factor. From the figure it is clear that at atmospheric pressure, the quality factor is linear with center frequency of the resonators. At vacuum level of 1.7×10^{-4}, the effect of air damping is negligible compared to

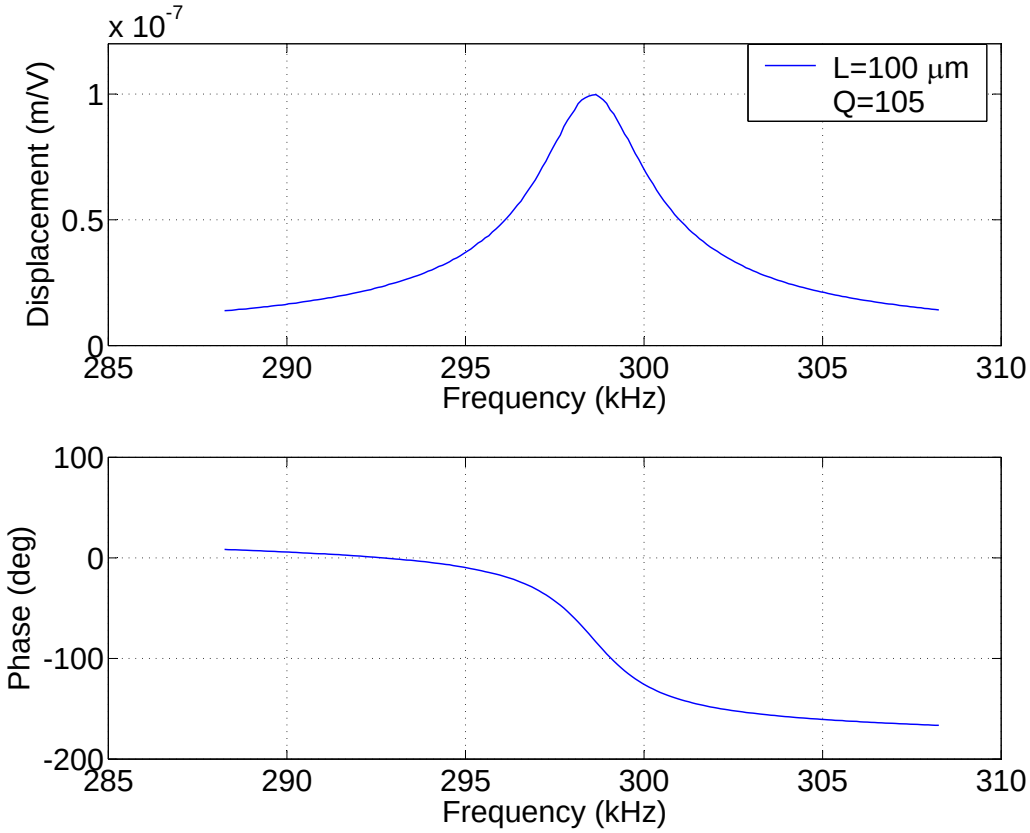

Figure 6.4: Frequency response of a 100 μm long cantilever beam at 1 atm.

thermoelastic damping and anchor loss. For this reason, at this vacuum level the quality factors did not show a dependence on center frequencies.

Because the attainable quality factors of cantilever resonators at atmospheric pressure are low, they must be operated in vacuum in order to achieve high enough quality factors. The packaging requirement makes the application of cantilever resonators to filter industry less friendly.

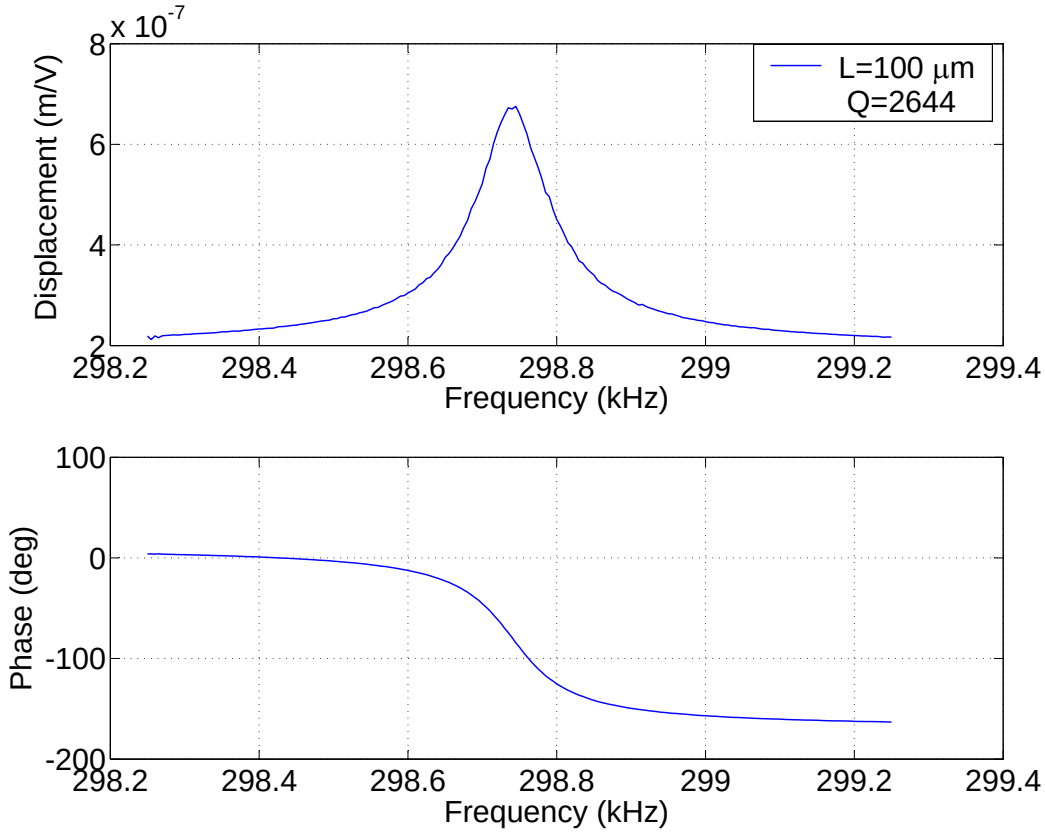

Figure 6.5: Frequency response of a 100 μm long cantilever beam in vacuum.

6.2.3 Linearity

To test working voltage range for the low frequency cantilever beam resonators, the output linearity of fabricated cantilever beam resonators has also been explored. For example, as shown in Fig. 6.7, a 100 μm cantilever beam with a resonance frequency of 298.65 kHz is driven at different driving voltage levels with a quasi-static frequency fixed to 10 kHz in this case. The displacement at the tip of the cantilever beam is measured at 1 atm by LDV. The measured result suggested a good linearity up to 1.5 V_{p-p} inputs. At increased voltages, the beam started to

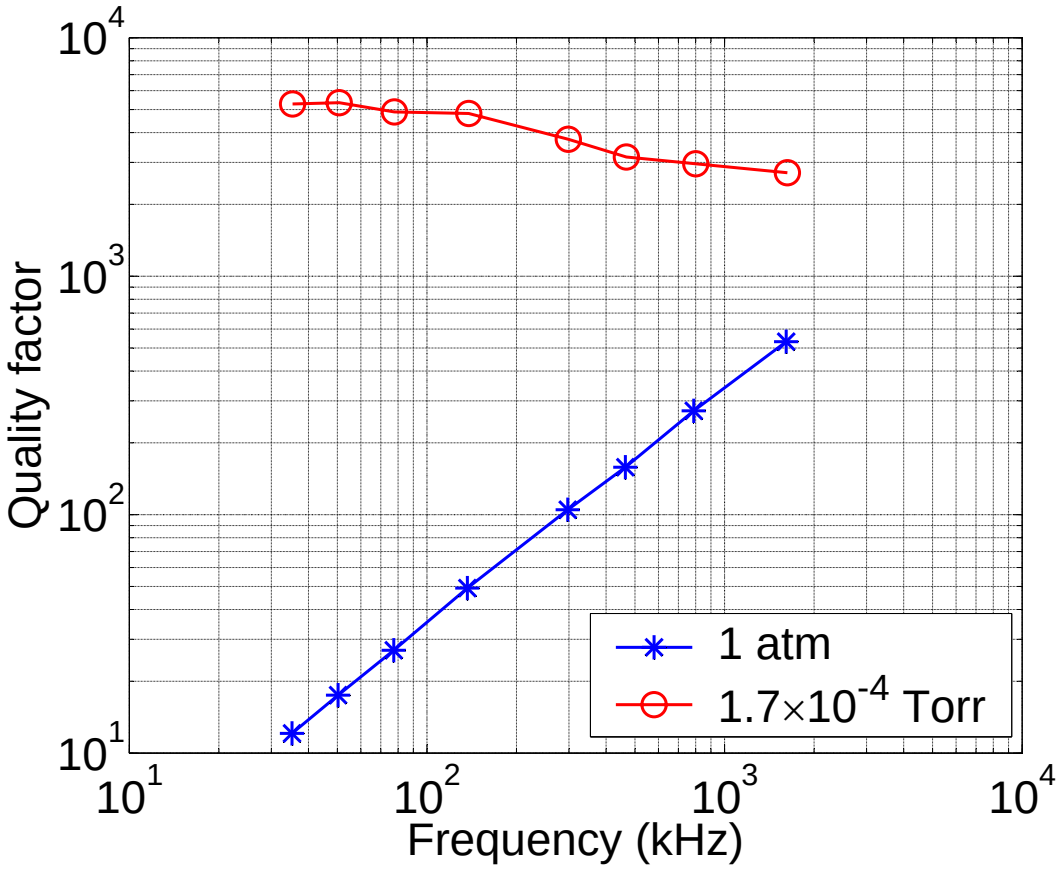

Figure 6.6: Quality factor vs. 1^{st} mode resonance frequency for fabricated cantilever beam resonators.

show nonlinearity. It is clear from this experiment, the driving voltage for these low frequency cantilever beam resonators should be restricted to 1.5 V_{p-p} or under. In comparison, Fig. 6.8 gives the displacement of the same beam driven at resonance frequency. Compared to quasi-static frequency activation, the displacement is 2 orders of magnitude higher. But the linear range is remained to 1.5 V_{p-p} or under.

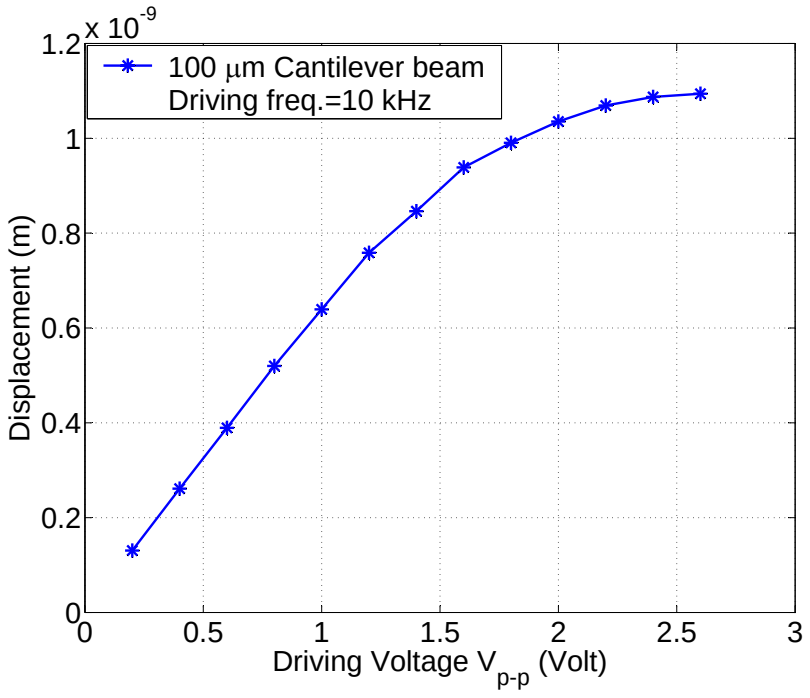

Figure 6.7: Quasistatic displacement vs. driving signal for a 100 μm long cantilever beam.

6.2.4 Temperature Stability of resonance frequency

The temperature stability of resonance frequency is inspected. Fig. 6.9 gives the resonance frequency of a 100 μm long cantilever beam resonator at different temperature levels. The temperature is controlled by heating the wafer chuck holding the cantilever beam chip. The measurement result gives a TCF value of -53.9 ppm/$^{\circ}C$.

In order to analyze the temperature dependence of resonance frequency, the theo-

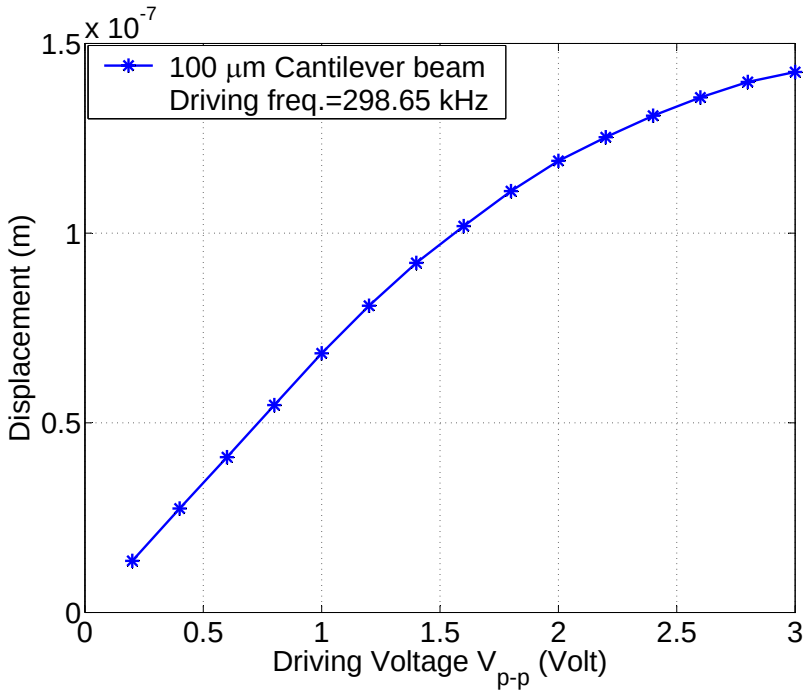

Figure 6.8: Resonance displacement vs. driving signal for a 100 μm long cantilever beam.

retical resonance frequency of cantilever beam resonators are rewritten in eq. 6.15.

$$f = \frac{1.8731^2 t}{2\pi L^2}\sqrt{\frac{E}{12\rho}} \tag{6.15}$$

The temperature dependence of resonance frequency is determined by the temperature dependence of E, ρ, t, L as given by eq. 6.16.

$$\frac{\partial f}{\partial T} = \frac{\partial f}{\partial t}\frac{\partial t}{\partial T} + \frac{\partial f}{\partial L}\frac{\partial L}{\partial T} + \frac{\partial f}{\partial E}\frac{\partial E}{\partial T} + \frac{\partial f}{\partial \rho}\frac{\partial \rho}{\partial T} \tag{6.16}$$

The temperature dependency of t, L, ρ is shown in the following equations.

$$\frac{\partial t}{\partial T} = \alpha_{Tf} \times t \tag{6.17}$$

$$\frac{\partial L}{\partial T} = \alpha_{Tf} \times L \tag{6.18}$$

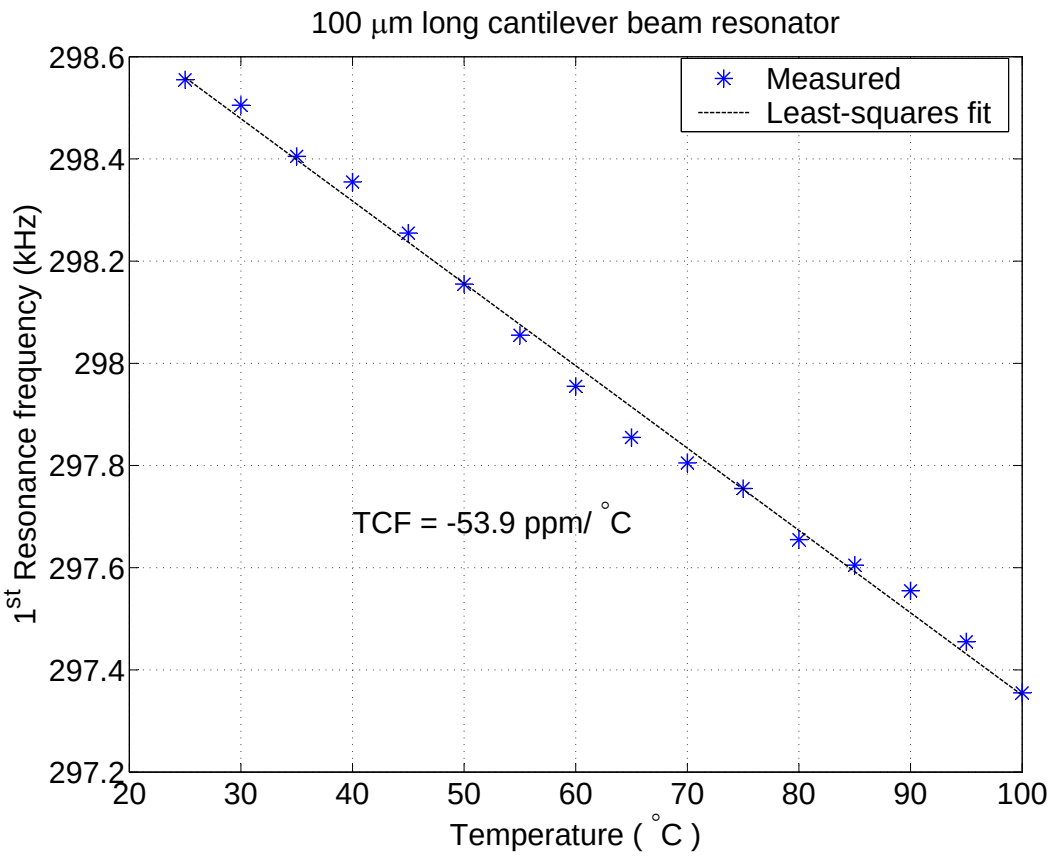

Figure 6.9: Resonance frequency of a 100 μm cantilever beam as a function of temperature.

$$\frac{\partial \rho}{\partial T} = -3\alpha_{Tf} \times \rho \tag{6.19}$$

Where α_{Tf} is thermal expansion coefficients of $Al_{0.3}Ga_{0.7}As$) and have value of $6.04 \times 10^{-6}/°C$. Finally, eq. 6.20 can be obtained.

$$\frac{\partial f/\partial T}{f} = \frac{1}{2}\frac{\partial E}{\partial T}\frac{1}{E} + \frac{1}{2}\alpha_{Tf} \tag{6.20}$$

The dependence of Young's modulus on temperature is not reported. Actually, the measurement of resonance frequency of cantilever beam resonators at different temperatures provides a method of extracting the temperature dependence of Young's

modulus on temperature, which from the measurement suggested the following value for $Al_{0.3}Ga_{0.7}As$.

$$\frac{\partial E}{\partial T}\frac{1}{E} = -56.92 \ \times 10^{-6}/^{\circ}C \tag{6.21}$$

6.3 Unimorph Clamped-Clamped Beam Resonators

Cantilever resonators are easy to implement and have larger amplitude compared to other configurations which will lead to higher signal to noise ratio (SNR). However, compared to other resonators with the same geometry but different boundary conditions, the resonance frequency of cantilever resonators are much lower. Therefore, cantilever resonators have a limited use in the microwave filter implementation area. Clamped-clamped resonators have resonance frequencies 5.3 times higher than those of cantilever resonators with same geometry and they are also easy to implement. For these reasons, the implementation of filters by clamped-clamped resonators are more realistic.

In this project, clamped-clamped beam resonators are fabricated from a 0.5 μm $Al_{0.3}Ga_{0.7}As$: Si/ 1 μm $Al_{0.3}Ga_{0.7}As$/ 2 μm $Al_{0.3}Ga_{0.7}As$: Si stack. Two different fabrication method, i.e. GaAs sacrificial etching and $Al_{0.7}Ga_{0.3}As$ sacrificial etching, have been explored. Those beams based on GaAs sacrificial etching are positioned at different orientation to measure the d_{31} values at different direction. Those beams based on $Al_{0.7}Ga_{0.3}As$ etching, are only positioned at $\langle 110 \rangle$ direction in order to take advantage of highest d_{31} values in this direction.

6.3.1 Resonance frequency

Fig. 6.10 gives the theoretical and measured resonance frequencies of clamped-clamped resonators with different lengths. In general, they exhibit good matching with a difference smaller than 3.8% for those beams having lengths in the range of 200 μm to 80 μm. Those beams outside of this range showed about 12% difference with theoretical predictions. This can be explained by two factors: for those having length larger than 200 μm, the internal stress must be considered when calculating the resonance frequency; for those with length smaller than 80 μm, failure of *Euler-Bernoulli* beam theory is a likely reason for the discrepancy.

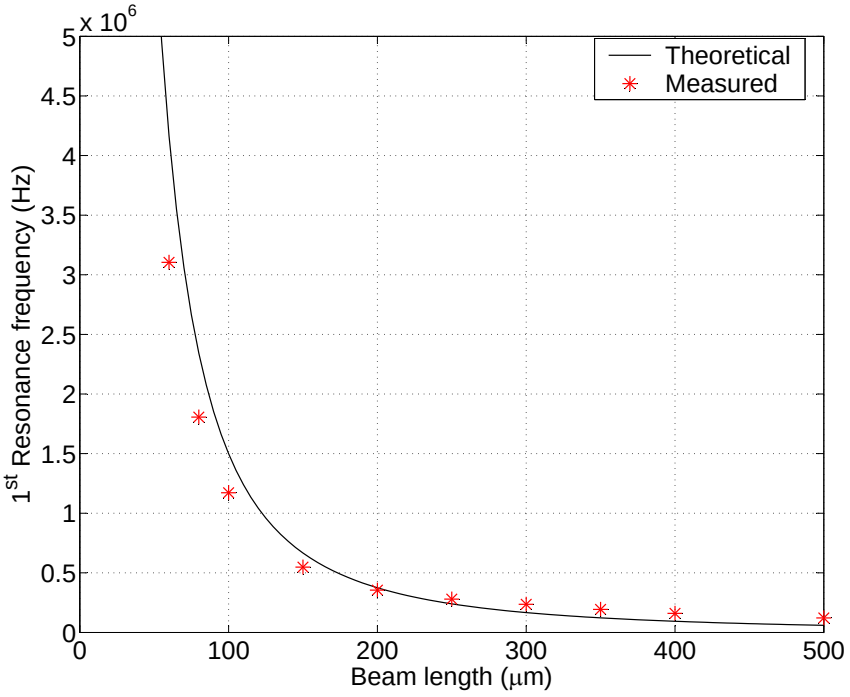

Figure 6.10: Theoretical and experimental resonance frequencies of clamped-clamped beams.

6.3.2 Dynamic Response

Fig. 6.11 shows frequency response of 100 μm long clamped-clamped beam resonators at different orientations. As expected, beams oriented closer to $\langle 110 \rangle$ direction showed higher amplitude of vibration. Another trend clear from the figure is that beams oriented closer to $\langle 110 \rangle$ direction showed a slightly higher resonance frequency. This can be explained by the following facts: first, the constituting material of $Al_{0.3}Ga_{0.7}As$ is anisotropic and the Young's modulus itself is changing with direction, i.e., the Young's modulus E at the direction of $\langle 110 \rangle$ is highest and decreases when the orientation changes to $\langle 100 \rangle$ direction; second, the extent of undercut is most severe when the orientation is along $\langle 100 \rangle$ direction, making the beam oriented closer to $\langle 110 \rangle$ direction has a shorter beam length, thus result in higher resonance frequency.

Fig. 6.12 gives measured quality factors of clamped-clamped resonators at atmospheric pressure and in vacuum. Similar to cantilever resonators, the attainable quality factors at atmospheric pressure is quite low due to the effect of air damping.

6.3.3 Linearity

The driving voltage range for linear behavior of developed clamped-clamped beam resonators are extracted by examining displacement of the center point of the beam at both quasi-static and resonance frequency. Similar to the cantilever beam resonators, clamped-clamped beam resonators should operate in a driving voltage

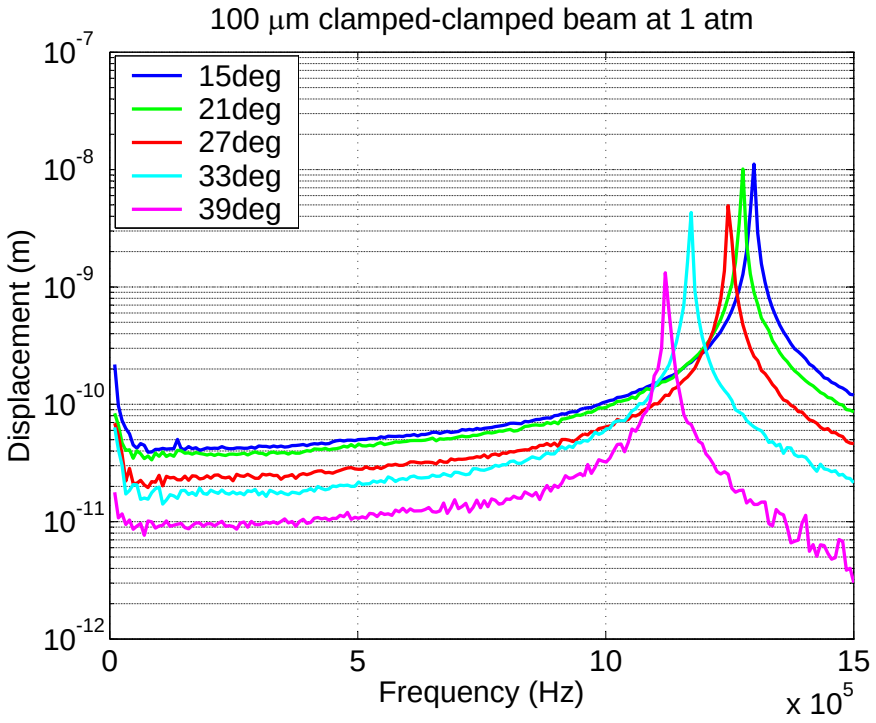

Figure 6.11: Frequency response of 100 μm long clamped-clamped beam resonators at different orientations. (Optical measurement).

range of 1.5 V_{p-p} or smaller.

6.3.4 Temperature Stability of Resonance Frequency

The resonance frequency temperature sensitivity of clamped-clamped $Al_{0.3}Ga_{0.7}As$ beam resonators has been analyzed and compared to the measured value in order to analyze the temperature stability of beam resonators. Fig. 6.15 gives the measured resonance frequency of a 150 μm clamped-clamped beam resonator at different temperatures.

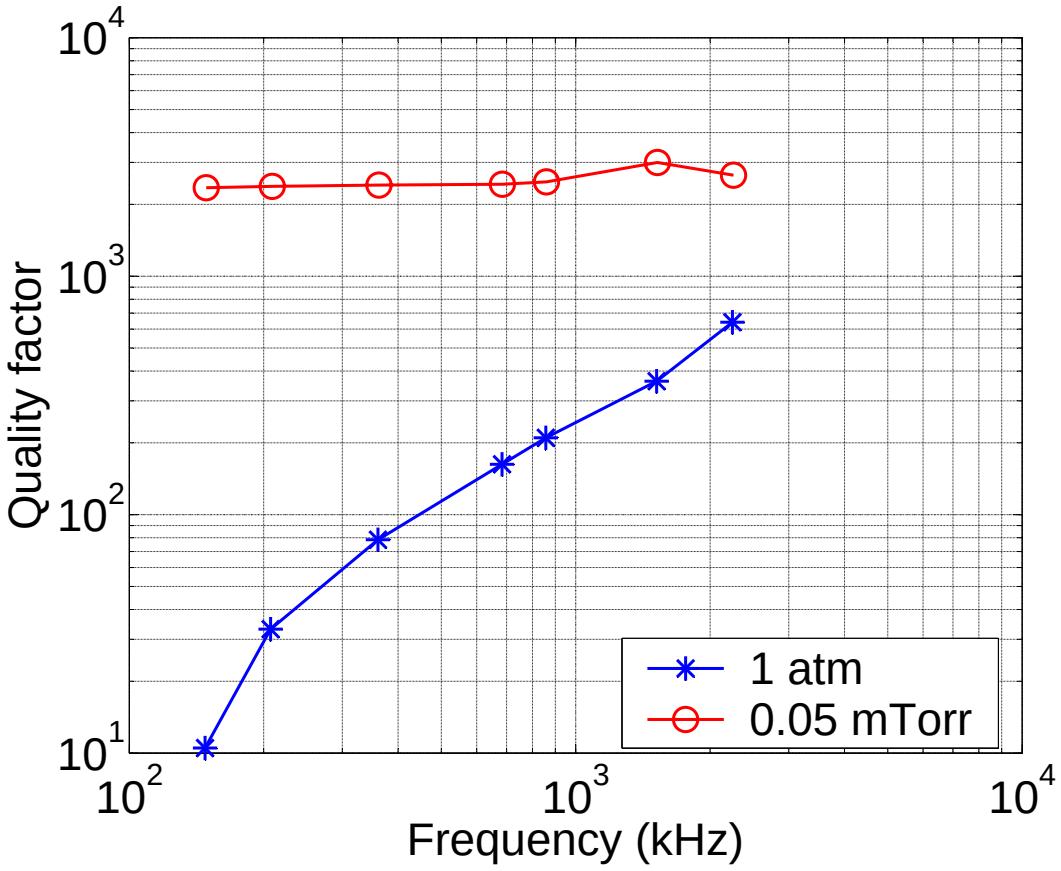

Figure 6.12: Quality factors vs. 1^{st} mod resonance frequency for fabricated clamped-clamped beam resonators.

In order to analyze the temperature dependence of clamped-clamped beam resonance frequency, the equation for the resonance frequency including the effect of residual stress is given in eq. 6.22.

$$f = \frac{3.56t}{L^2}\sqrt{\frac{E}{12\rho}}\sqrt{1+\frac{0.295\sigma L^2}{Et^2}} \tag{6.22}$$

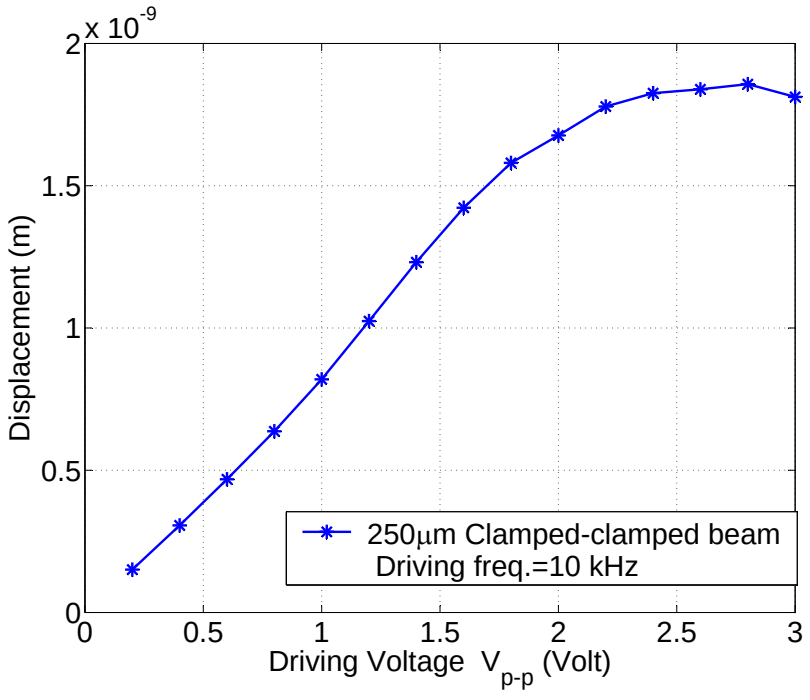

Figure 6.13: Quasistatic displacement vs. driving signal for a 250 μm long clamped-clamped beam.

Here σ represents internal stress. The temperature sensitivity of natural frequency can be calculated from the following equation.

$$\frac{\partial f}{\partial T} = \frac{\partial f}{\partial t}\frac{\partial t}{\partial T} + \frac{\partial f}{\partial L}\frac{\partial L}{\partial T} + \frac{\partial f}{\partial E}\frac{\partial E}{\partial T} + \frac{\partial f}{\partial \rho}\frac{\partial \rho}{\partial T} + \frac{\partial f}{\partial \sigma}\frac{\partial \sigma}{\partial T} \tag{6.23}$$

By taking partial differential of Eq. 6.23, the following equations are obtained:

$$\frac{\partial f}{\partial t} = \frac{f}{t} \times \frac{1}{1 + \frac{0.295\sigma L^2}{Et^2}} \tag{6.24}$$

$$\frac{\partial f}{\partial L} = \frac{f}{L} \times \frac{-2 - \frac{0.295\sigma L^2}{Et^2}}{1 + \frac{0.295\sigma L^2}{Et^2}} \tag{6.25}$$

$$\frac{\partial f}{\partial E} = \frac{f}{E} \times \frac{1}{2(1 + \frac{0.295\sigma L^2}{Et^2})} \tag{6.26}$$

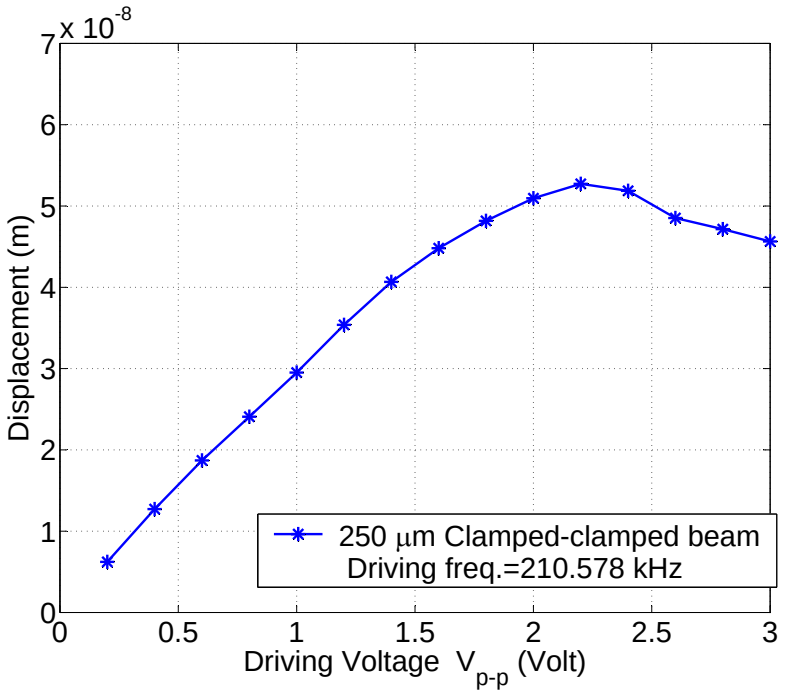

Figure 6.14: Resonance displacement vs. driving signal for a 250 μm long clamped-clamped beam.

$$\frac{\partial f}{\partial \rho} = -\frac{1}{2}\frac{f}{\rho} \tag{6.27}$$

$$\frac{\partial f}{\partial \sigma} = \frac{1}{2}\frac{f}{\sigma} \times \frac{\frac{0.295\sigma L^2}{Et^2}}{1+\frac{0.295\sigma L^2}{Et^2}} \tag{6.28}$$

Assuming the change in internal stress is mainly due to thermal mismatch between the $Al_{0.3}Ga_{0.7}As$ thin film and GaAs substrate, the temperature dependency of 5 parameters is shown in following equations:

$$\frac{\partial t}{\partial T} = \alpha_{Tf} \times t \tag{6.29}$$

$$\frac{\partial L}{\partial T} = \alpha_{Ts} \times L \tag{6.30}$$

$$\frac{\partial E}{\partial T} = -4.84 \times 10^{-3}\, GPa/^{\circ}C \tag{6.31}$$

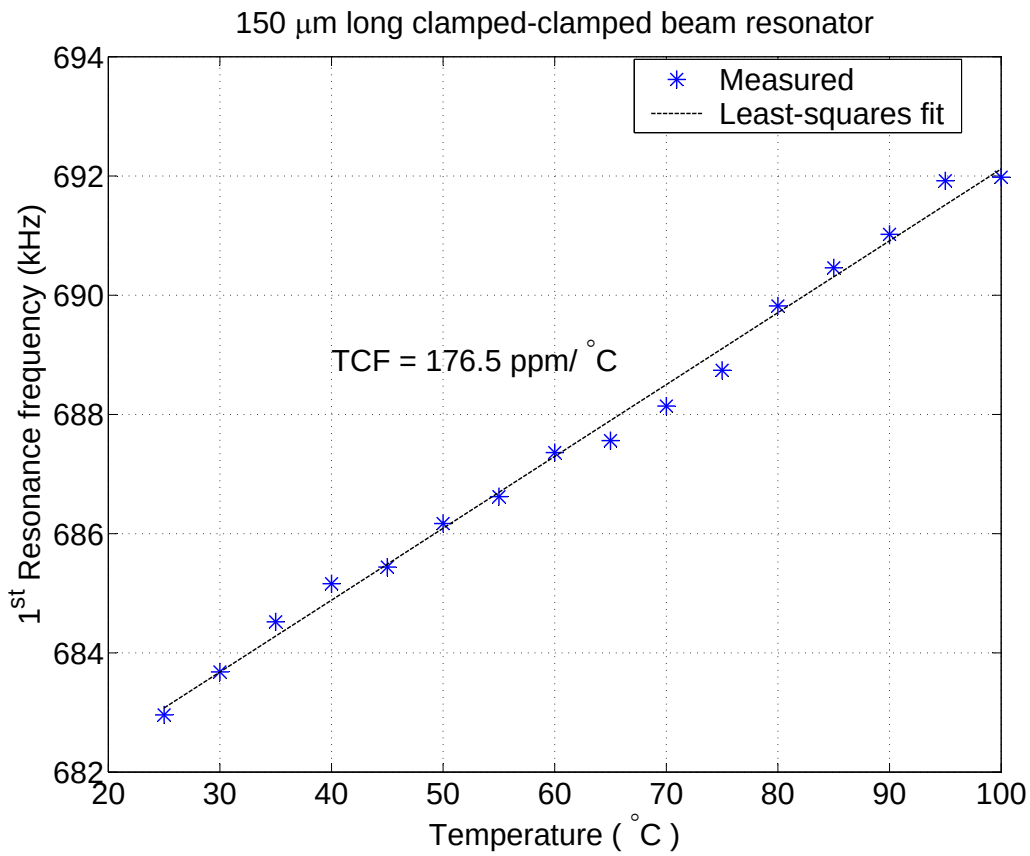

Figure 6.15: Resonance frequency of a 150 μm long clamped-clamped beam as a functiong of temperature.

$$\frac{\partial \rho}{\partial T} = -(\alpha_{Ts} + 2 \times \alpha_{Tf}) \times \rho \tag{6.32}$$

$$\frac{\partial \sigma}{\partial T} = (\alpha_{Tf} - \alpha_{Ts}) \times \frac{E}{1-\nu} \tag{6.33}$$

In conclusion, the following equation is obtained to calculate the temperature dependency of resonance frequency of clamped-clamped beam resonator.

$$\begin{aligned} \frac{\partial f/\partial T}{f} &= \frac{1}{1+\frac{0.295\sigma L^2}{Et^2}} \times \alpha_{Tf} - \frac{2+\frac{0.295\sigma L^2}{Et^2}}{1+\frac{0.295\sigma L^2}{Et^2}} \times \alpha_{Ts} \\ &+ \frac{1}{2(1+\frac{0.295\sigma L^2}{Et^2})} \frac{\partial E/\partial T}{E} + \frac{1}{2}(\alpha_{Ts} + 2\alpha_{Tf}) \end{aligned}$$

$$+ \quad \frac{1}{2}\frac{\frac{0.295\sigma L^2}{Et^2}}{1+\frac{0.295\sigma L^2}{Et^2}}\frac{\partial\sigma/\partial T}{\sigma}$$

By putting in the corresponding material properties of constructing material and estimated internal stress level of -80 MPa, the calculated TCF is $234\,ppm/°C$. The discrepancy between the theoretical prediction is believed to be mainly due to the error in internal stress measurement and other factors affecting the internal stress level with temperature change.

6.4 Unimorph Free-Free Beam Resonators

Cantilever and clamped-clamped resonators developed in this project showed quality factors of less than 3,500 for resonance frequencies in the 100 kHz–2 MHz range when placed in vacuum. The energy losses through their anchors is the main factor limiting the attainable quality factors in vacuum. In order to alleviate the high loss associated with these beams, free-free beam designs are explored.

6.4.1 Free-Free Beam Design

The schematic of the free-free beam structure used in this work is shown in Fig. 6.16. The designed structure consists of a free-free beam supported by 4 support beams attached at the resonant beam's node points. The support beams are designed to work in their fundamental torsional mode. In theory, the highest quality factor will occur when the resonance frequency of free-free beam matches with the torsional resonance frequency of the support beams [16].

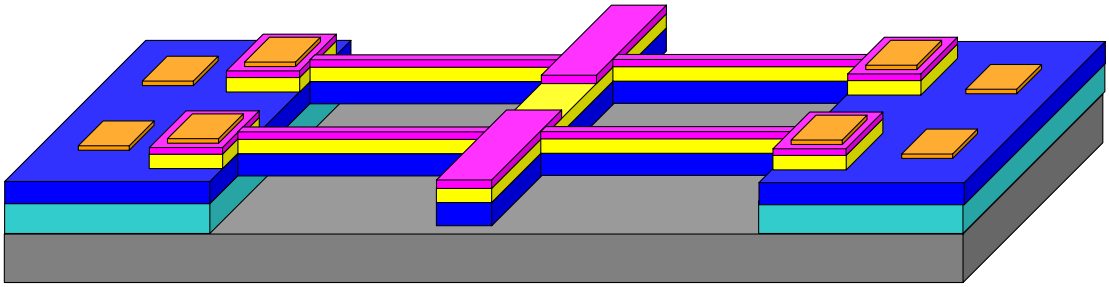

Figure 6.16: Schematics of the free-free beam structure used in this work.

The resonance frequency of the free-free beam is calculated form the following equation.

$$f_i = \frac{\lambda_i^2}{2\pi L^2}\sqrt{\frac{Et^2}{12\rho}} \tag{6.34}$$

The definition of each parameters are given previously. For the first resonance frequency, the eigenvalue λ_1 has the value of 4.730. The expression of the generalized modal shapes of the free free beams are given in eq. 6.35.

$$r(\xi) = \sin(\lambda_i\xi) + \sinh(\lambda_i\xi) + \gamma(\cos(\lambda_i\xi) + \cosh(\lambda_i\xi)) \tag{6.35}$$

Where

$$\gamma_i = \frac{\sin(\lambda_i) - \sinh(\lambda_i)}{\cosh(\lambda_i) - \cos(\lambda_i)} \tag{6.36}$$

The normalized first modal shape of the free-free beam is plotted in Fig. 6.17. The nodal points for the first mode free-free beams are located in $\xi = 0.2242$ and $\xi = 0.7759$. The torsional support beams must join the free-free beams in nodal points in order to insure impedance matching and minimal energy losses.

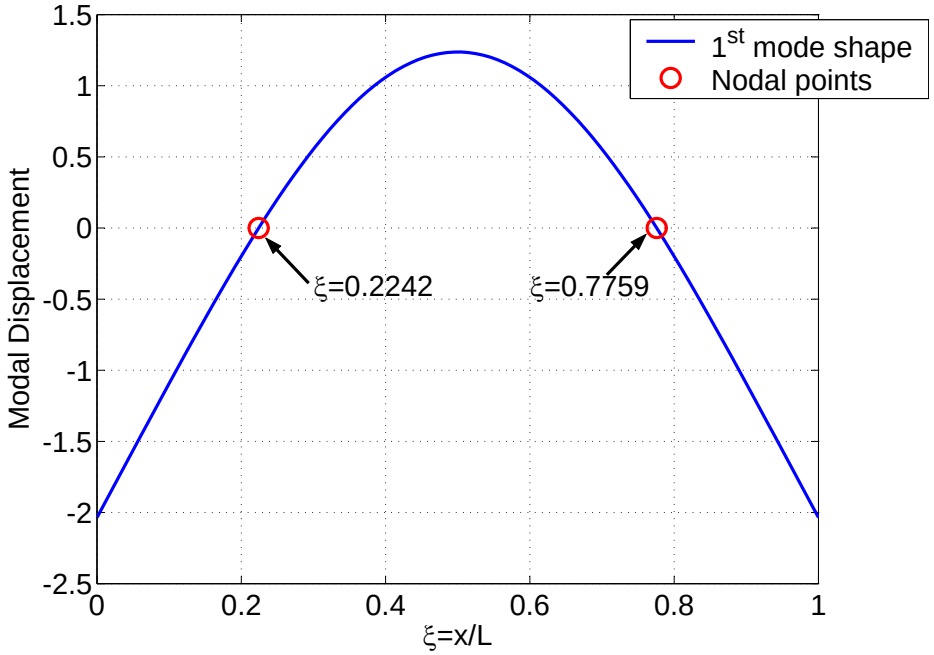

Figure 6.17: Length normalized 1^{st} mode shape of a free-free beam.

The supporting beams are designed to work on their first resonant torsional mode. Consider a clamped-clamped torsional beam, the torsional resonance frequency can be calculated as

$$f_i = \frac{\lambda}{2\pi L}\sqrt{\frac{GJ}{\rho J_p}} \tag{6.37}$$

Where λ_i is eigenvalues and has values of $\lambda_i = n\pi$ for nth mode, G is shear modulus of elasticity of the material and can be obtained by $G = \frac{E}{2(1+\nu)}$, J is the torsional moment of inetia, J_p is the polar moment of inertia.

The free-free beams developed are fabricated from 0.5 μm $Al_{0.3}Ga_{0.7}As$: Si/ 1 μm $Al_{0.3}Ga_{0.7}As$/ 2 μm $Al_{0.3}Ga_{0.7}As$: Si heterostructures. The fabrication is the same as that of clamped-clamped beams. The SEM image of full structure after release is

shown in Fig. 6.18. Resonators with frequencies ranging from 400 kHz to 2.5 MHz have been fabricated. The length of the torsional support beams ranged form 30% to 130% of the optimal value to evaluate the effect of imperfect support impedance matching between the resonant beam and torsional support beams.

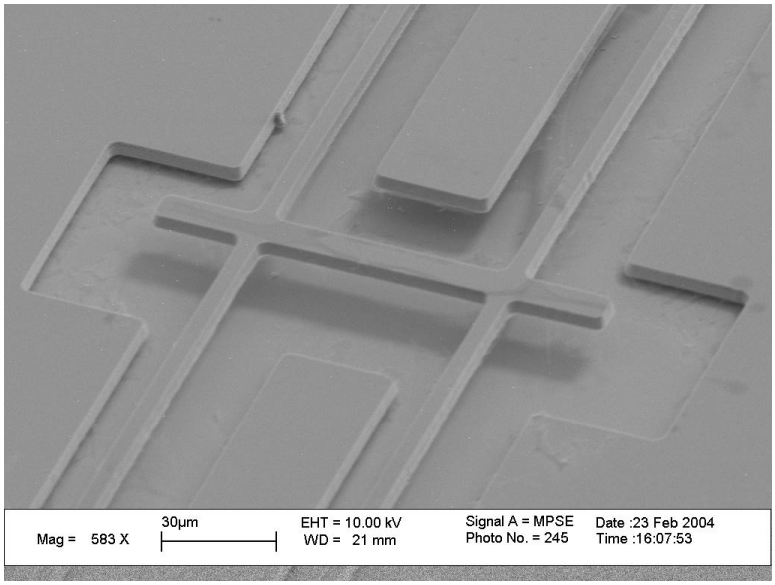

Figure 6.18: SEM of a 100μm long free-free beam after release.

6.4.2 Dynamic Response

The developed free-free beam resonators were first characterized by LDV. In order to investigate the effect of torsional support on the quality factor, the quality factors of free-free beam with different support beams were measured. Fig. 6.19 summarized the quality factors of free-free beam at different support beam length. The designed free-free beam resonance frequency is 2 MHz. However, due to the effect of smaller length to width ratio (in this case 4), and attached support beams, the measured resonance frequency shifted to 2.3 MHz. The increased resonance frequency means the length of support beam should be decreased for impedance matching. Thus, highest quality factor is obtained when support beams are somewhat shorter than the theoretical value. The displacement spectra of different points of free-free shown in Fig. 6.20. As expected, the edge of the free-free beam showed greater displacement compared to the center point of free-free beam. Also, the node point showed approximately no movement at resonance frequency confirming the free-free beam modal shpape. Plotted in Fig. 6.21 is the frequency response of the displacement at the edge of resonant beam in high vaccum. The measured quality factor is 11,341. Compared to quality factors obtained from cantilever and clamped-clamped beam resonators, the quality factor of free-free beam is much higher. The increased Q values are expected due to reduced anchor losses compared to the previous configurations.

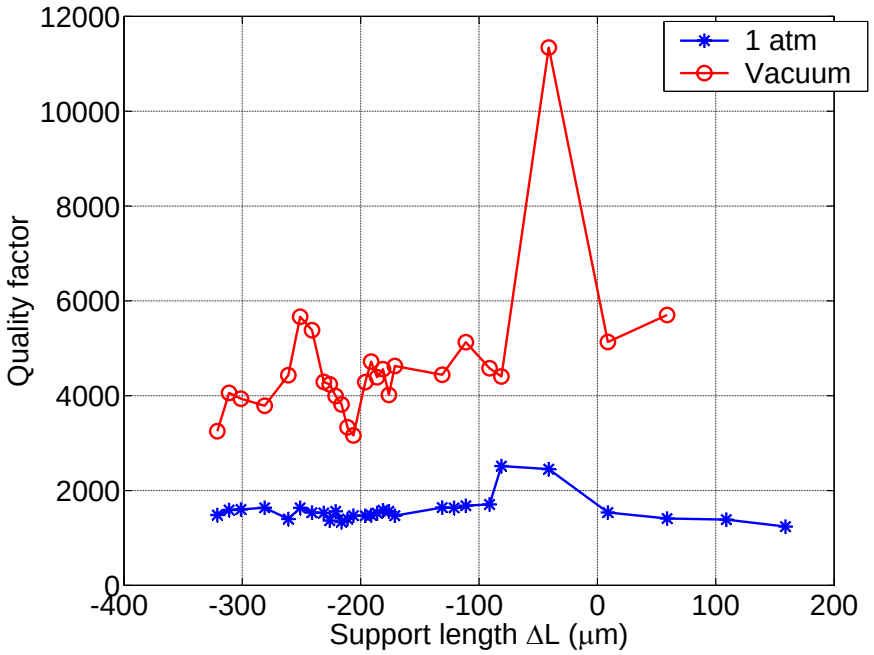

Figure 6.19: Quality factors of free-free beams vs. support beam length.

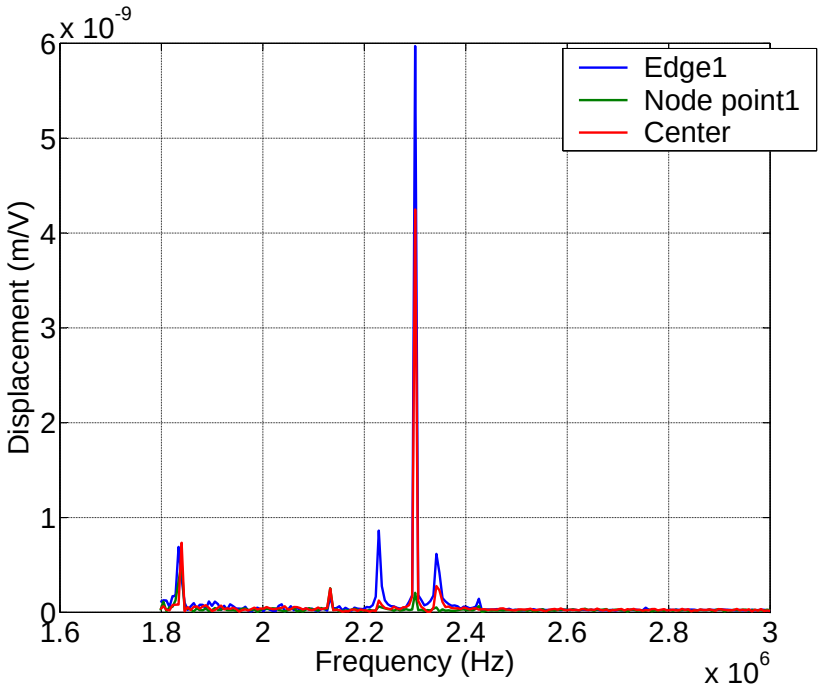

Figure 6.20: Displacement spectra of a 200 μm long free-free beam.

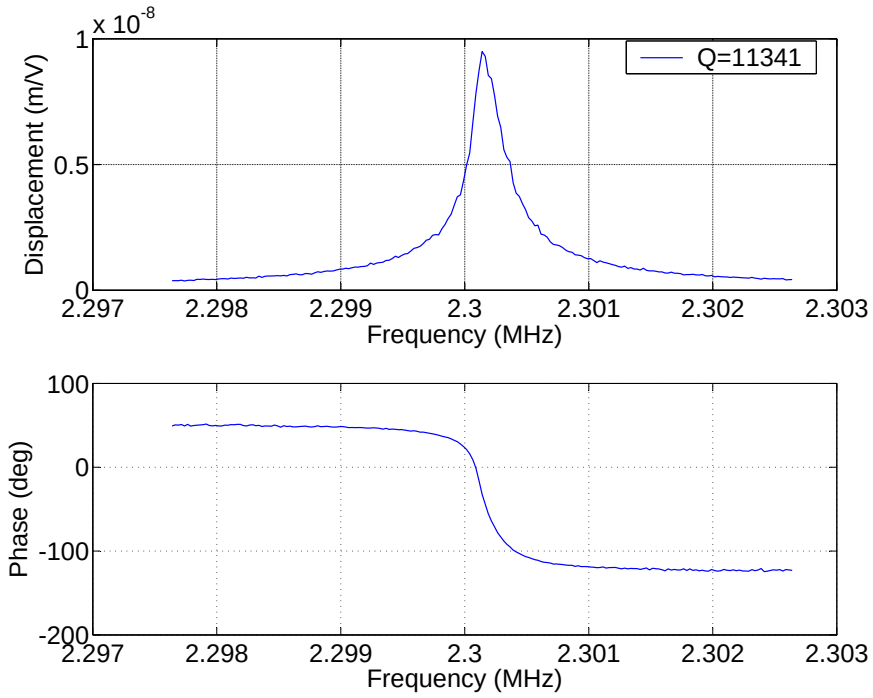

Figure 6.21: Dynamic response of the displacement at the edge of a 200μm long free-free beam.

6.4.3 Linearity

The linearity of free-free beam resonators is inspected. Fig. 6.22 gives displacement of center point of free-free beam at resonance frequency. The displacement showed linear response to driving voltage of 1.5 V_{p-p}.

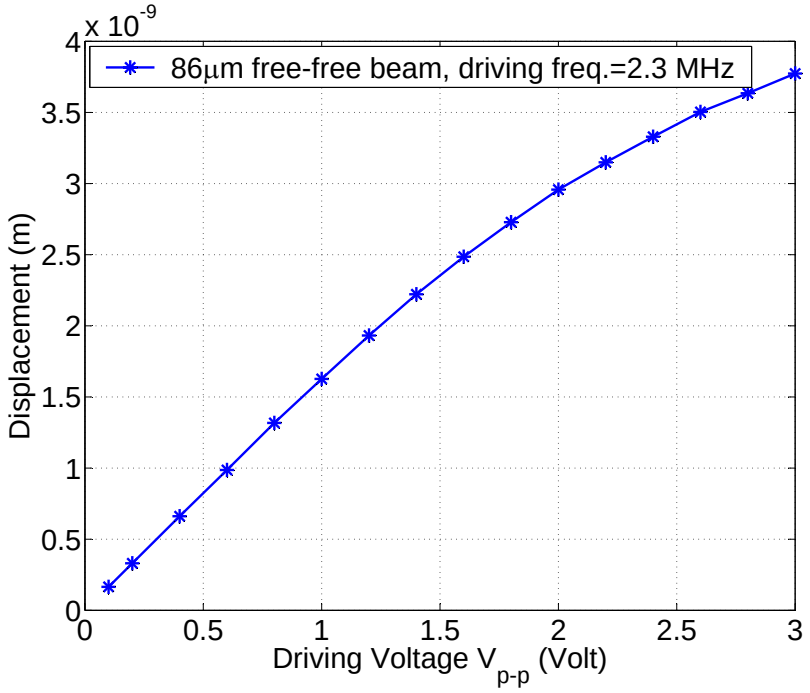

Figure 6.22: Displacement vs. driving signal for a 200μm long free-free beam.

The linearity of the free-free beam structure showed similar characteristics compared to cantilever and c-c beam configurations.

6.4.4 Temperature Stability of Resonance Frequency

The resonance frequency of developed free-free beam resonator is measured at different temperature in order to investigate temperature stability of resonance frequency. Fig. 6.23 gives the measured results with TCF of $-53.68\,ppm/°C$. Again, most of this value is from temperature dependence of Young's modulus of thin film $Al_{0.3}Ga_{0.7}As$.

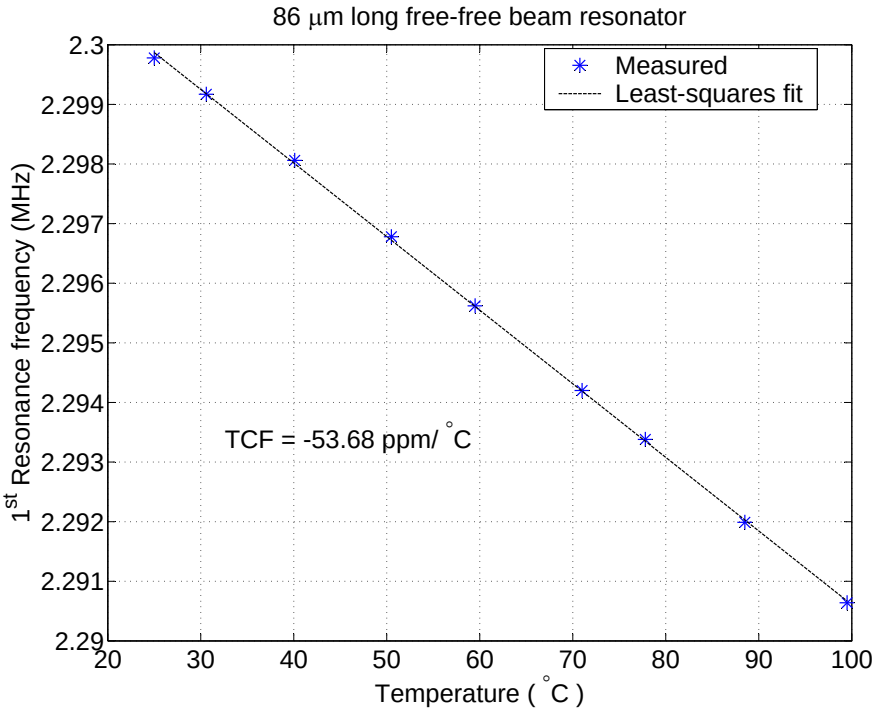

Figure 6.23: Resonance frequency of an $86\mu m$ long free-free beam as a function of temperature.

Chapter 7

Piezoelectric Bimorph Cantilevers

Although, piezoelectric cantilevers have limited use in high-frequency filter implementations, they are a good candidate for micro actuators. Piezoelectric actuators are widely studied for their inherent characteristics including high force and large bandwidth. Micro actuators based on piezoelectric materials have been demonstrated by using a variety of thin film materials, including ZnO [34] and PZT [41]. In these examples, the piezoelectric micro actuators are all based on unimorph configurations, where a single piezoelectric layer is positioned with an offset from the beam's neutral axis to provide bending momentum to the actuator. In comparison, true bimorph design commonly consists of two identical piezoelectric layers positioned symmetrically about the neutral axis. Despite of the increased efficiency provided by bimorph configurations compared to unimorph with identical geometry, reported piezoelectric micro actuators are all based on unimorph configurations due to the constraints imposed by fabrication processes. The implementation of bimorph micro actuators require three electrodes to provide electrical potentials to two separate piezoelectric layers. The fabrication of bimorph micro actuators with common piezoelectric thin films such as ZnO and PZT is prohibited by thermal budgets which preclude the integration of more than two electrodes, or poor substrate conditions imposed by electrode materials which prevent further growth of

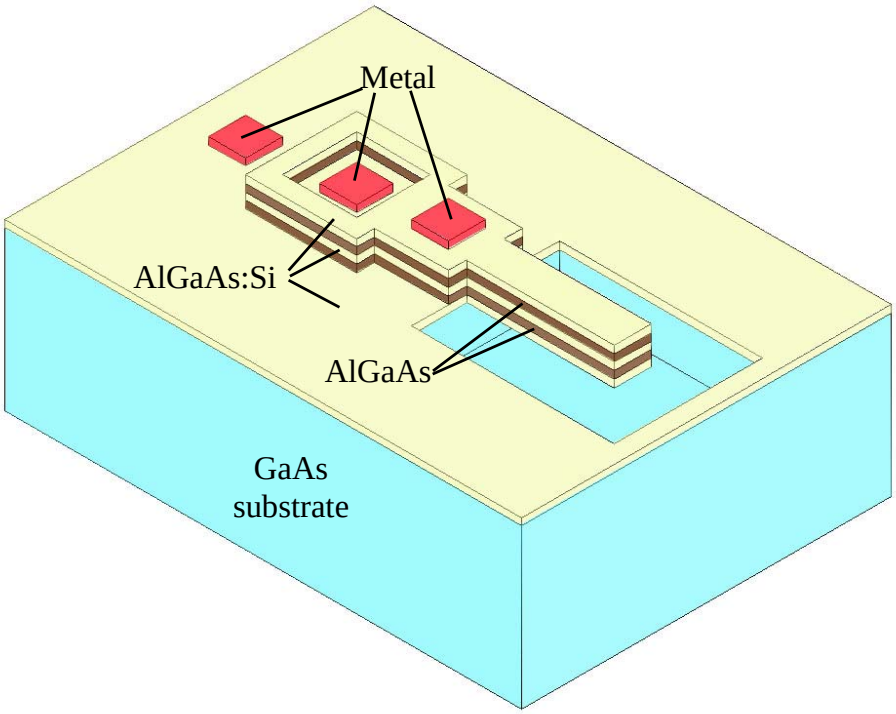

Figure 7.1: Schematic of bimorph $Al_{0.3}Ga_{0.7}As$ actuators.

high quality piezoelectric films.

In contrast, the fabrication process developed in this project can be used to realize bimorph piezoelectric micro actuators based on single crystal $Al_{0.3}Ga_{0.7}As$ material. Fig. 7.1 gives schematic view of developed bimorph micro actuators. From bottom to top, the deposited heterostructure consists of 0.5 μm $Al_{0.3}Ga_{0.7}As$: Si, 1μm $Al_{0.3}Ga_{0.7}As$, 0.5 μm $Al_{0.3}Ga_{0.7}As$: Si, 1μm $Al_{0.3}Ga_{0.7}As$, and 0.5 μm $Al_{0.3}Ga_{0.7}As$: Si. The fabrication process is similar to that of unimorph cantilevers except for patterning of additional electrode layers by ICP. Fig. 7.2 shows schematic cross-section and SEM image of a typical bimorph cantilever beam.

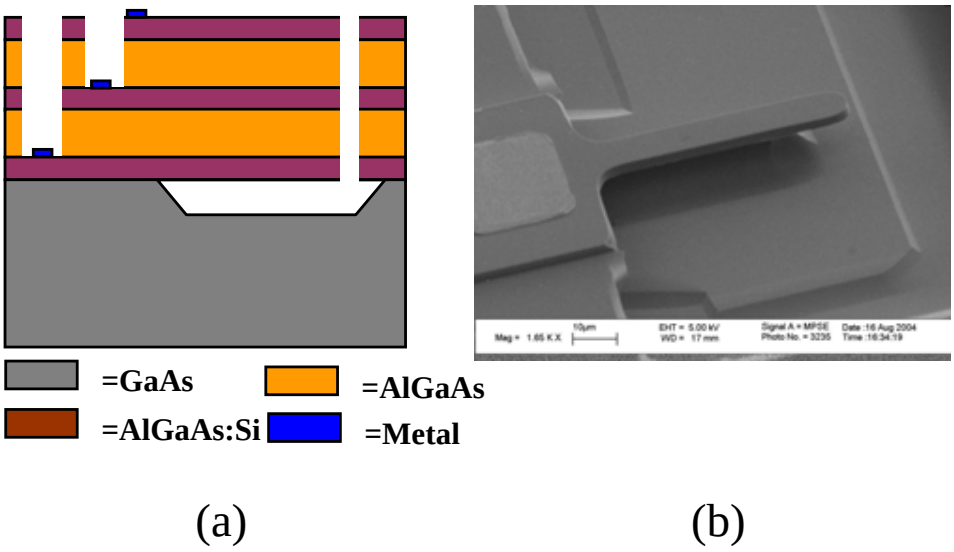

Figure 7.2: (a) Schematic of bimorph cantilever cross-section, and (b) SEM image of a fabricated bimorph cantilever.

7.1 Resonance Frequency

Cantilever bimorph actuators are fabricated with lengths ranging from 500 μm to 20 μm with fixed width of 10 μm. The corresponding measured resonance frequencies are from 9.1 kHz to 5.7 MHz with good agreement with theoretical predictions as shown in Fig. 7.3. The low frequency bimorph resonators are characterized by LDV for quasistatic and broadband response. Measured resonance frequencies matched well with theoretical predictions, with deviations of 3.6% or less.

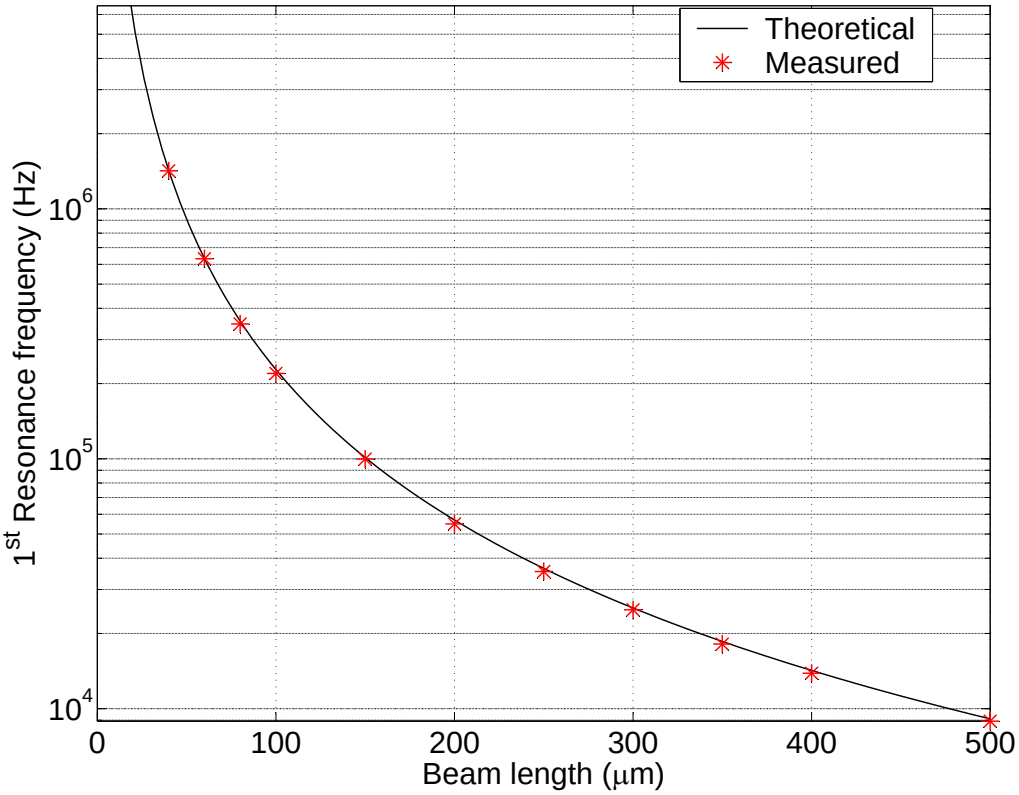

Figure 7.3: 1^{st} Resonance frequency of bimorph cantilevers.

7.2 Dynamic Response

Typical frequency response spectra for the fabricated bimorph actuators are shown in Fig. 7.4 for the case of 150 μm long cantilever beam in vacuum to reduce air damping. The middle electrode layer for the bimorph resonator is grounded, and a sweeping sinusoidal input is added to the top electrode only, the bottom electrode only, and top and bottom electrode at the same time. As expected, the bimorph excitation resulted in increased vibration amplitude compared to the top or bottom excitation only configuration.

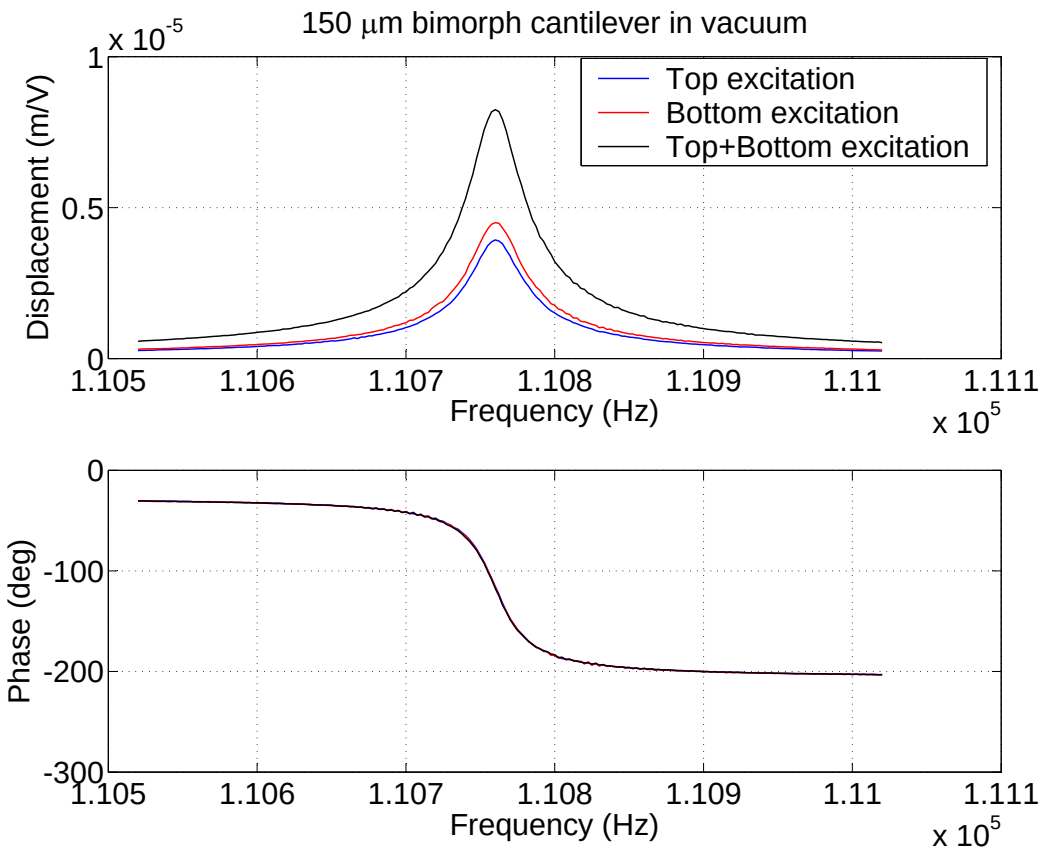

Figure 7.4: Frequency response of a 150 μm long cantilever beam in vacuum.

7.3 Displacement and Gain

For comparison of bimorph and unimorph excitation, Fig. 7.5 gives the displacement of bimorph cantilevers at resonance under vacuum for different driving conditions. Fig. 7.6 summarizes the quasistatic (5 kHz) displacement of bimorph cantilevers at different driving condition. For both case, bimorph actuation provided 80–120% of increased displacement compared to top piezoelectric layer only, or bottom piezoelectric only actuation of the same device.

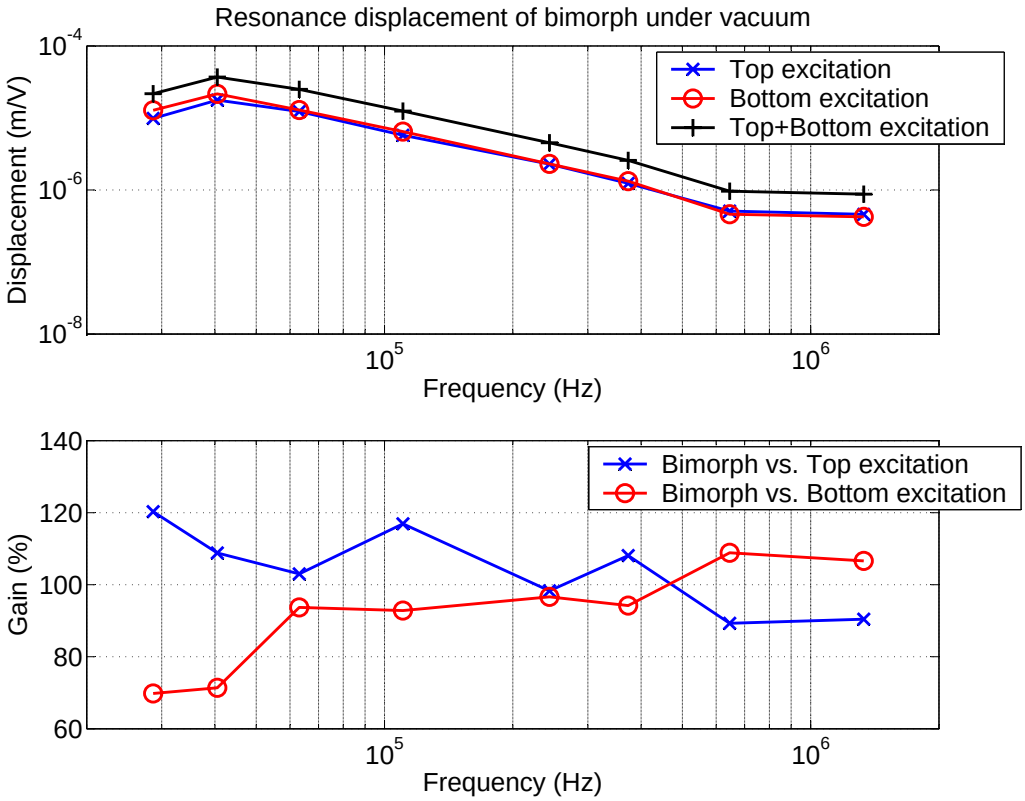

Figure 7.5: (a) Displacement of bimorph cantilever beams at resonance under vacuum for varying driving condition, and (b) displacement gain.

7.4 Linearity

The linearity of the bimorph cantilevers are investigated in order to define the driving voltage range for the proper activation of the developed actuators. Fig. 7.7 gives the displacement of a 100 μm long bimorph cantilever actuator at different driving levels when placed in atmospheric pressure. Both the quasistatic and resonance displacement results are suggesting driving voltage of less than 3.5 V peak-peak in order to avoid nonlinearity in the beam. The working voltage range for

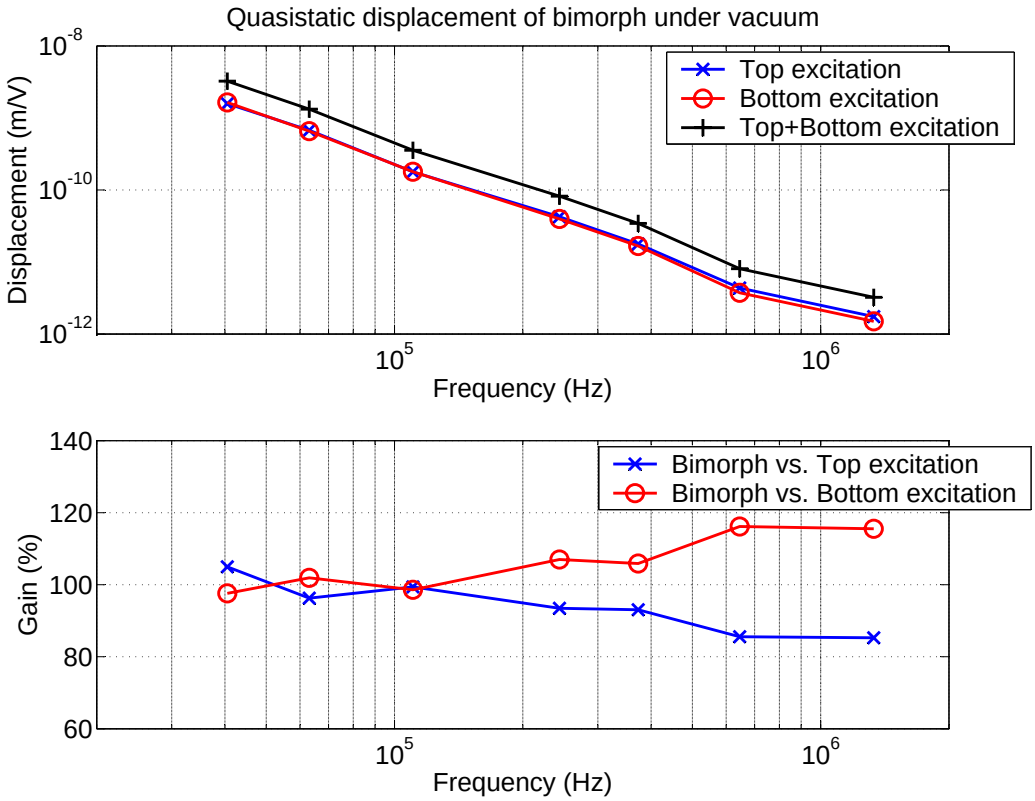

Figure 7.6: (a) Quasistatic displacement, and (b) displacement gain for a range of bimorph cantilever lengths.

bimorph canitlevers are much higher than those of unimorph cantilevers which is 1.5 V_{p-p}. The possible reason for this phenomenon comes from symmetrical actuation in bimorph actuators whereas the unimorph cantilevers features an asymmetrical actuation.

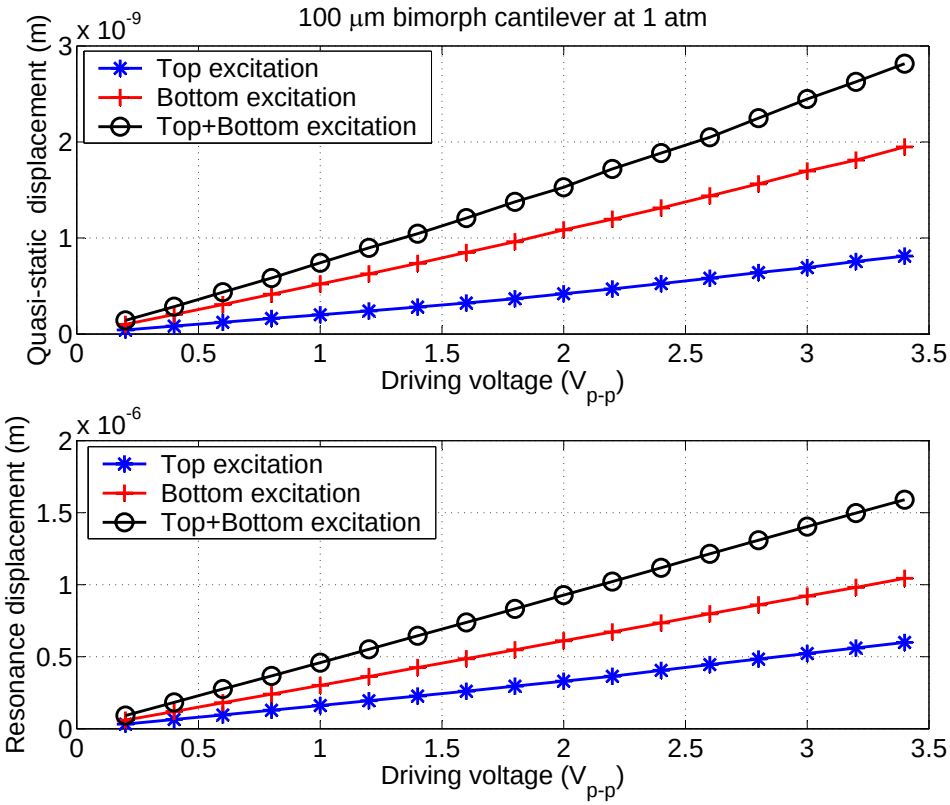

Figure 7.7: (a) Displacement of bimorph cantilever beams at resonance under vacuum for varying driving condition, (b) displacement gain.

7.5 Temperature Stability

The resonance frequency of developed bimorph cantilever actuators are measured at different temperatures in order to investigate the effect of temperature change on the resonance frequency of the actuators. Fig. 7.8 gives the resonance frequency of a 100 μm long cantilever beam at temperature range of $30°C$ to $100°C$. The experiment result showed a TCF of $-50.6\,ppm/°C$ with most of this coming from the temperature dependence of Young's modulus for the $Al_{0.3}Ga_{0.7}As$ film.

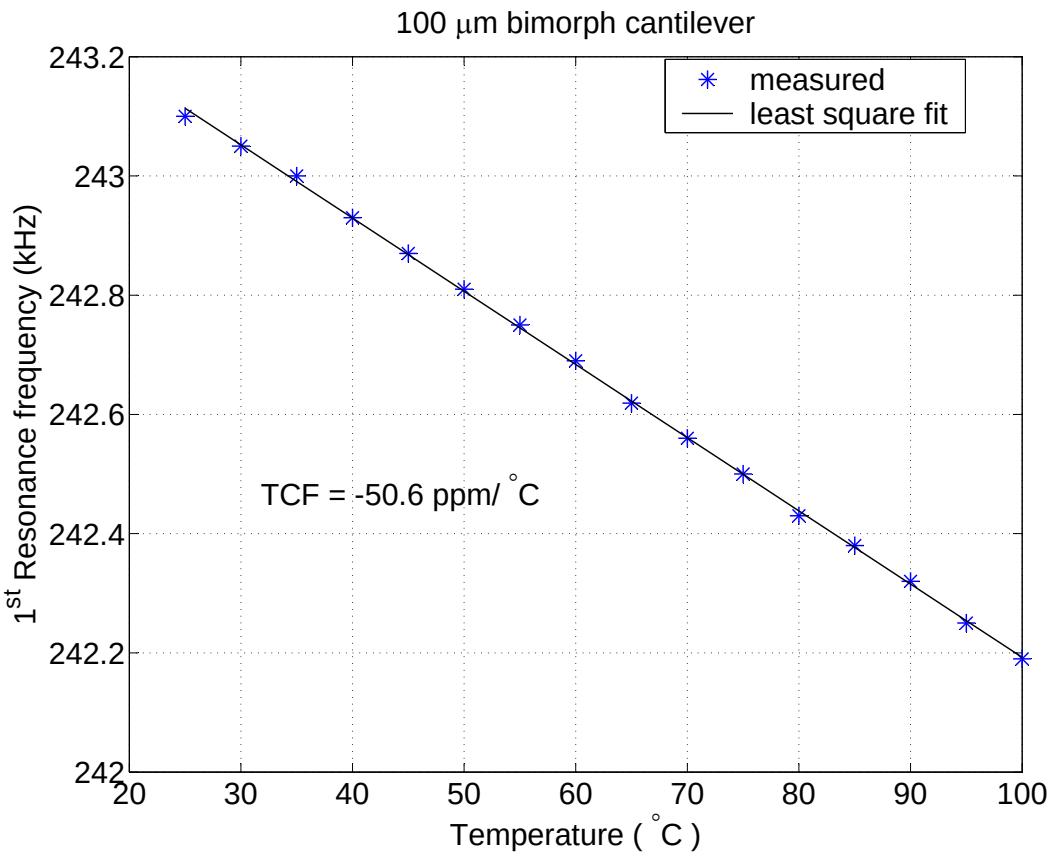

Figure 7.8: Resonance frequency of a 100 μm long bimorph cantilever beam at different temperatures.

7.6 Quality Factors

The effect of increased interfacial layers are investigated by comparing the quality factors of bimorph and unimorph cantilevers. All quality factors are measured under vacuum to reduce the effect of air damping. The bimorph configuration had 5 different layers whereas unimorph configuration had 3 different layers. The effect of increased interfacial layers can be found from Fig. 7.9 where the quality factors for bimorph and unimorph cantilevers under vacuum are shown. It is clear

from the figure that bimorph cantilevers did not show a reduced quality factors compared to geometrically same unimorphs, which means the increased interfacial layers had little impact on the quality factors.

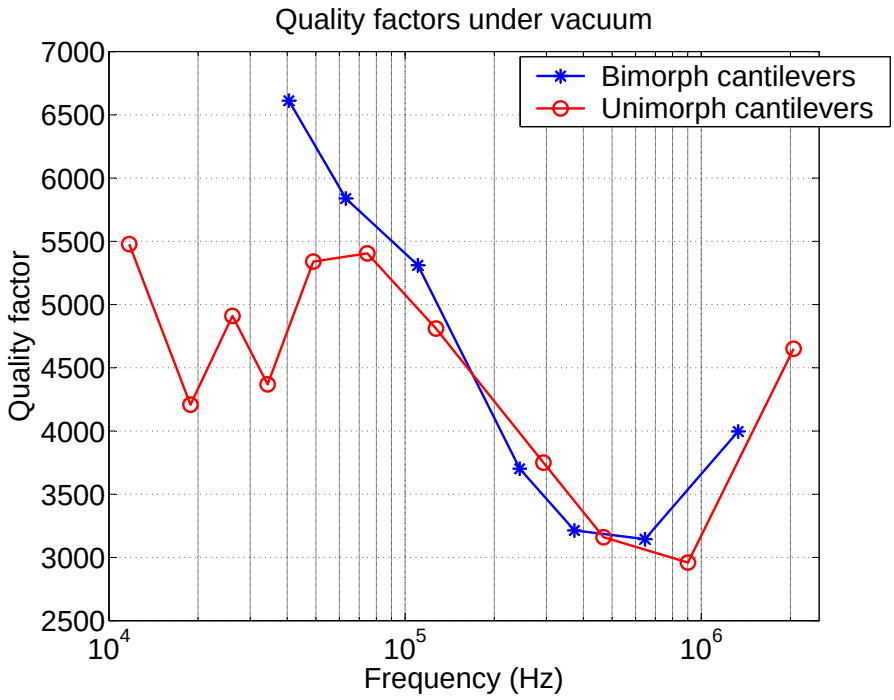

Figure 7.9: Measured quality factors for bimorph and unimorph cantilevers under vacuum.

The quality factors of the bimorphs at different pressure are measured to see the effect of air damping as shown in Fig. 7.10. It is clear from this figure that air damping has very little effect on the quality factor of bimorph actuators when vacuum level is lower than 10^{-2} Torr.

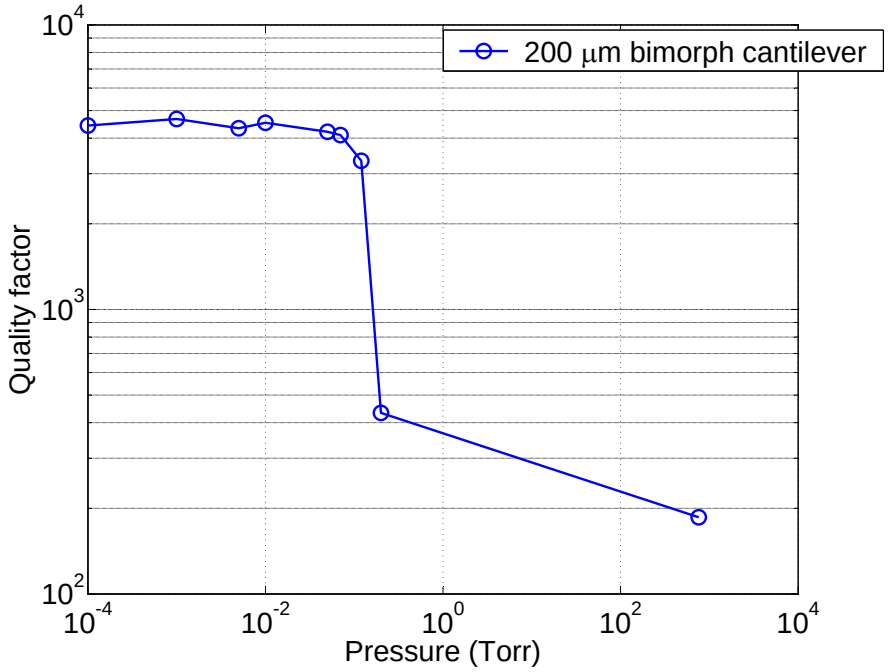

Figure 7.10: Measured quality factors for a 200 μm bimorph at different vacuum levels.

Chapter 8

Length Extensional Mode Resonators

The flexural mode resonators described in previous chapters all feature relatively large displacements. As a result, the flexural mode resonators are sensitive to air damping. In order to achieve higher quality factors, vacuum packaging is necessary for those resonators, putting complexity in fabrication.

In contrast, the resonators presented in this chapter works in length extensional mode and have a relatively small displacement. Therefore, they are less sensitive to the presence of air damping.

The schematics of the free-free bar resonators used in this work is shown in Fig. 8.1. The free-free beam anchored at its midpoint is driven into longitudinal vibration by signals applied to the continuous electrode surfaces on either side of the piezoelectric layer. It is possible to excite all odd modes of vibration with this configuration, although signal from higher modes will suffer from attenuation due to the cancellation of charge on areas of the beam with opposite strain.

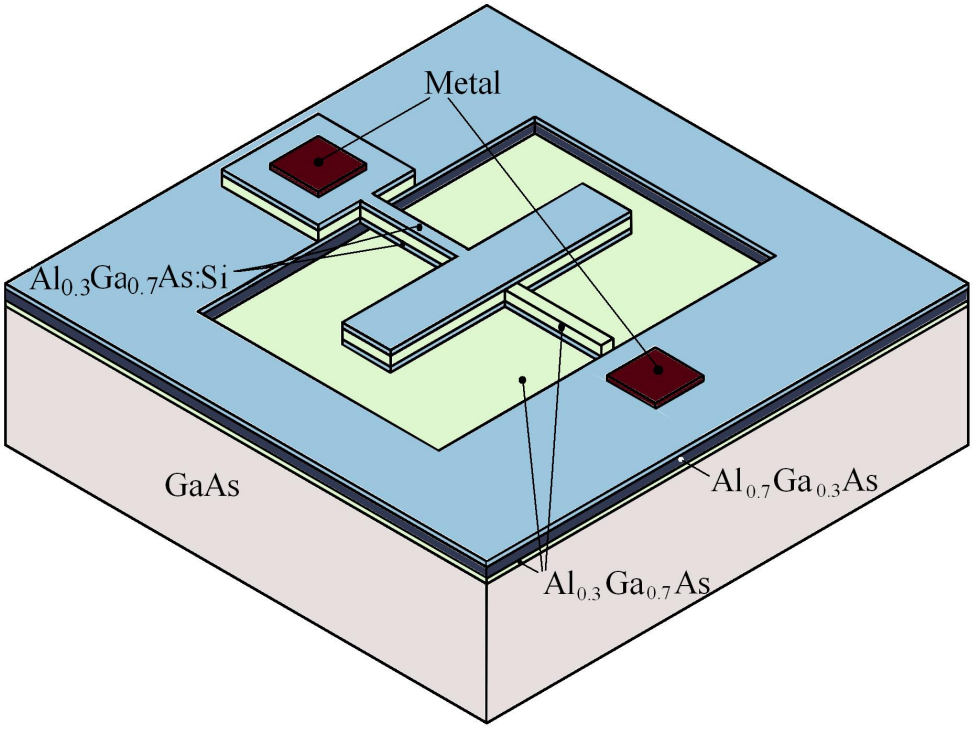

Figure 8.1: Schematics of bar resonators.

8.1 Bar Resonator Model

The n^{th} mode resonance frequency is given by

$$f_n = \frac{n}{2L}\sqrt{\frac{E}{\rho}} \tag{8.1}$$

where n, L, E and ρ represent mode number, beam length, elastic stiffness in the direction of vibration, and beam density, respectively. The output current resulting from strain of the piezoelectric layer is given by [21]:

$$I(j\omega) = j\omega \int D_3 dA \tag{8.2}$$

where D_3 is the electric displacement on the top electrode, defined through the linear piezoelectric constitutive equations as:

$$D_3 = d_{31} E b S_1(x) \tag{8.3}$$

where d_{31} is the transverse piezoelectric coupling coefficient, b is the beam width, and $S_1(x)$ is the strain field along the beam length. The strain field can be written in terms of the longitudinal displacement, given by $u = X(j\omega)\phi(x)$, as $S_1(x) = du/dx$. Here, $X(j\omega)$ is the modal displacement and $\phi(x)$ is the mode shape. For a free-free beam, the mode shape is given by [21]:

$$\phi(x) = cos(\frac{n\pi}{L}x) \tag{8.4}$$

Thus, for all odd modes (n=1,3,5,), the output current may then be written as:

$$I(j\omega) = -2j\omega d_{31} E b X(j\omega) \tag{8.5}$$

The electromechanical coupling parameter η is defined as the ratio of output charge to modal displacement. From equation 8.5, η is found to be:

$$\eta = \frac{I(j\omega)}{j\omega X(j\omega)} = -2 d_{31} E b \tag{8.6}$$

Following a Butterworth-Van Dyke equivalent circuit approach for piezoelectric resonators, the single-port device shown in Fig. 8.1 may be modeled by a motional RLC branch with component values defined by the coupled electromechanical behavior of the piezoelectric structure, in parallel with a static capacitive branch defined by the parasitic capacitance of the piezoelectric film. Higher order modes are included by placing additional motional branches in parallel with the fundamental

mode motional branch. The motional resistance is a critical parameter in resonator design, since it represents the effective impedance of the structure at resonance. The motional resistance for the nth longitudinal vibration mode, $R_{x,n}$, is given by [47]:

$$R_{x,n} = \frac{M\omega_n}{Q\eta^2} \tag{8.7}$$

The modal mass for the beam, M, may be derived as:

$$M = \int_0^L \rho bt\phi^2(x)dx = \frac{\rho btL}{2} \tag{8.8}$$

Therefore, the motional resistance for all odd modes of a bar resonator is given by:

$$R_{x,n} = \frac{n\pi\rho^{0.5}t}{8d_{31}^2E^{1.5}bQ} \tag{8.9}$$

8.2 Experimental Results

Electrical device characterization was performed using the same circuit described in chapter 5, in which a resonator is used as a branch of a capacitive bridge as depicted schematically in Fig. 8.2. The non-active branches of the bridge are composed of matched on-chip capacitors with impedance equal to that of the resonator far from resonance.

The fabricated bar resonators were tested using an Agilent 4395A network analyzer. Both atmospheric and vacuum measurements were conducted to observe the effects of air damping on quality factor, motional resistance, and power handling. For measurement in atmospheric pressure, devices were placed on an RF-1 probe station (Cascade Microtech, Beaverton OR). The electrical contacts to the devices

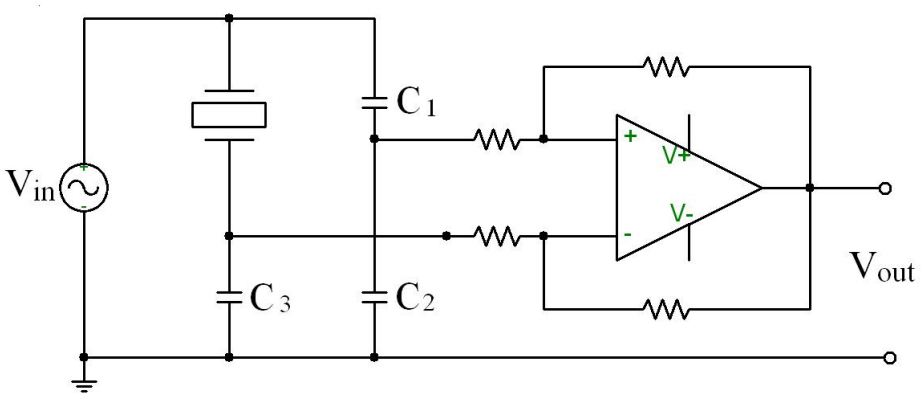

Figure 8.2: Schematic of capacitive bridge interface circuit.

are accomplished by coaxial probes to reduce cross talk between probes. A table top vacuum probe station (Desert Cryogenics, Tuscon AZ) equipped with 50 Ω BeCu-tipped stripline probes was used for resonator characterization at reduced pressures.

Bar resonators were fabricated with a width of 20 μm and lengths ranging from 100 μm to 1000 μm, corresponding to measured first-mode resonance frequencies between 2.5 MHz and 25 MHz. As shown in Fig. 8.3, the measured resonance frequencies show excellent agreement with theoretical values determined from Eqn. 8.2 for the first 5 odd modes, with deviations smaller than 1% observed for all measurements.

The quality factors of bar resonators were measured at both atmospheric pressure and moderate vacuum levels. Experimental quality factors are summarized for atmospheric pressure measurements in Fig. 8.4(a), and for 70 μTorr measurements

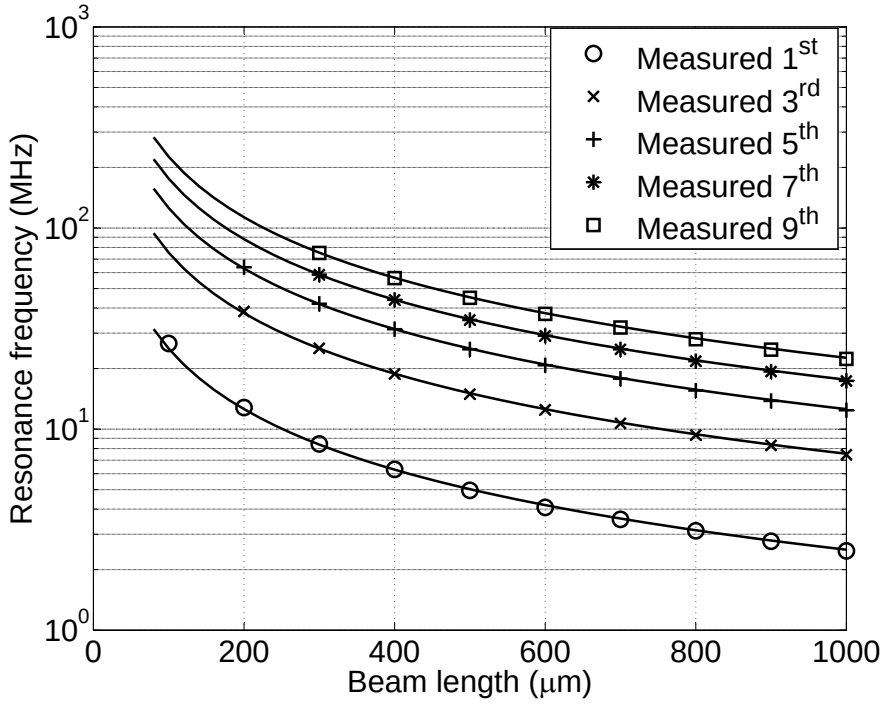

Figure 8.3: Theoretical and measured resonance frequencies. Experimental results match theoretical values to within 1% for all measurements.

in Fig. 8.4(b), for the 1st through 9th odd modes of vibration. As expected, the vacuum measurements exhibit higher Qs. Measured Q values at 70 Torr are on average 2 times higher than their corresponding atmospheric pressure measurements, indicating that air damping remains a dominant loss mechanism for these devices. Both sets of measurements display a similar trend, with Q values increasing nearly linearly with resonance frequency up to 25 MHz. This observed increase may be the result of higher losses at low frequencies due to excitation of spurious modes in devices with large length-to-width ratios. The maximum Q value was measured from a 900 μm long bar resonator operating in its 7th resonant mode at 21.8 MHz.

Fig. 8.5 shows the frequency spectra for this measurement, with a quality factor of 25,390 in vacuum.

For measurements beyond 25 MHz, limitations in the capacitive bridge interface often prevented the collection of good data due to poor signal-to-noise. However, in some measurements Qs were observed to level off and drop as the resonance frequency increased. For example, a 9^{th} mode resonator in vacuum provided a Q of 5,331 at 56.3 MHz, dropping to only 1,621 at 75.2 MHz. Assuming thermoelastic damping is the dominant loss mechanism [54] at higher frequencies, Q is expected to be inversely proportional to resonance frequency. However, it is also possible that increased losses occur due to failure of Euler-Bernoulli beam theory as the modal vibration period nears the beam width in higher frequency devices. While Euler-Bernoulli beam theory is valid for length to width ratios above 10, rolloff in Q is observed to begin when the modal period is around 100 μm, or 5 times the beam width. Maintaining a length to width ratio above 10 may improve high frequency Qs in future designs.

8.2.1 Motional Resistance

Resonator motional resistance, given by the ratio of voltage and current at the resonance frequency, should ideally be as close to 50 Ω as possible in order to provide impedance matching to typical 50 Ω RF circuits. The motional resistance of fabricated piezoelectric resonators was determined by directly connecting the

bar resonators to 50 Ω impedance of the input and output ports of the network analyzer. From the measured insertion loss (IL) of the devices at resonance, the motional resistance can be calculated as:

$$R_{x,n} = 50 \times 10^{\frac{IL}{20}} \tag{8.10}$$

Fig. 8.6 shows the measured motional resistance of bar resonators operating in their 1^{st} and 3^{rd} modes. Measurements of R_x for higher modes are not reported here since the impedance of the static piezoelectric capacitance at higher frequencies is comparable to the theoretical motional resistance, preventing accurate measurement of R_x. The lowest measured motional resistance was $R_x = 4.3$ kΩ at 12.78 MHz for a device resonating in its 1^{st} longitudinal mode. Although higher than the desired 50 Ω value, measured motional resistances are comparable with reported values for electrostatic resonators [47] or showing improvement compared to other piezoelectric bar resonators [9] within a similar resonance frequency range.

8.2.2 Power Handling

The ability of a resonator to handle practical power levels is an important parameter when considering real-world applications of microscale resonators. To assess power handling limits, devices were driven with gradually increasing power levels until nonlinear behavior became apparent in the resonant response. For example, Fig. 8.7(a) presents the transmission curve of a 300 μm long bar resonator at various input power levels. The power levels shown in this figure are the set

power levels from network analyzer. The set power is applied through a 50 Ω source resistance (R_s) within the network analyzer, which generates an appropriate driving signal based on the assumption of an equal 50 Ω load resistance. In reality the effective load is substantially higher due to the motional resistance of the resonator, and the actual power through the resonator (P_R) is lower than the set power (P_{set}) by a factor which is inversely proportional to the motional resistance (R_x):

$$P_R \approx 4P_{set}\frac{R_s}{R_x} \qquad \text{for} \qquad R_x \gg R_s \tag{8.11}$$

For the device shown in Fig. 8.7(a), the motional resistance of the resonator was measured at approximately 8 kΩ. Due to the impedance mismatch between this resonator and the 50 Ω source and load impedances of network analyzer, the power dissipated in the resonator is approximately -6 dBm when the power output of the network analyzer is set to 10 dBm. Power handling levels for 1^{st} and 3^{rd} mode operation of all fabricated devices is shown in Fig. 8.7(b). As with R_x measurements, power handling values are not reported for higher modes since the static feedthrough capacitance of the piezoelectric film shunts the majority of the input power at higher frequencies, leading to artificially high values of apparent power handling capacity using the measurement technique described above. Overall, the measured 1^{st} and 3^{rd} mode values compare favorably against power handling levels reported for comparable electrostatic bar resonators, which exhibit a typical operational range between about -40 and 20 dBm [47]. Further improvements in power handling can be realized by increasing resonator thickness, although at the expense of increased motional resistance.

8.2.3 Temperature Stability

Uncompensated temperature stability has been measured at atmospheric pressure. Variation in the 1st resonant frequency of an 800 μmm long bar resonator is shown in Fig. 8.8 over a temperature range of $30 - 100°C$. The resulting temperature coefficient of frequency (TCF) is 45 $ppm/°C$ and mainly due to the temperature dependence of Young's modulus of the $Al_{0.3}Ga_{0.7}As$ films. This value is substantially higher than that of AT-cut quartz crystal resonators (on the order of -1.7 $ppm/°C$ [55]) but compares favorably with other MEMS resonators. For example, bar resonators fabricated using a piezo-on-silicon technology exhibited an uncompensated TCF of -40 $ppm/°C$ [9].

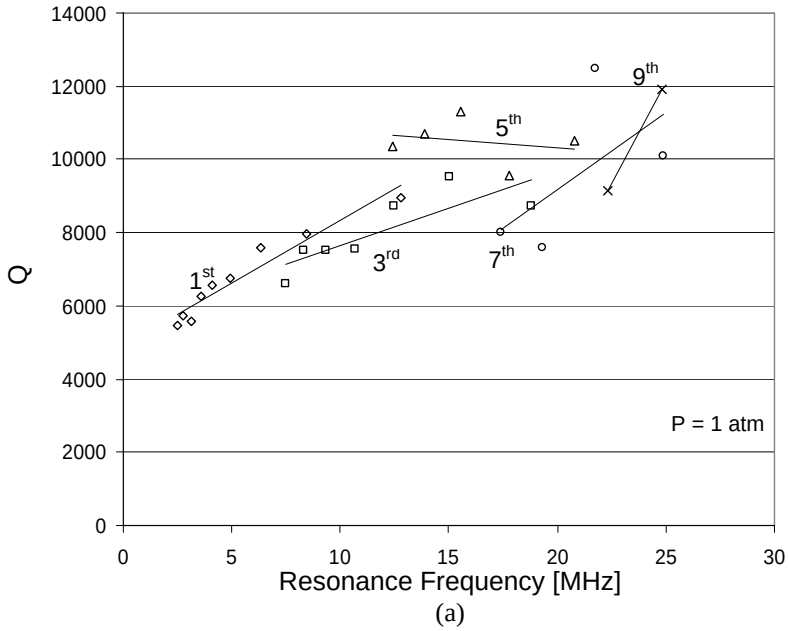

(a)

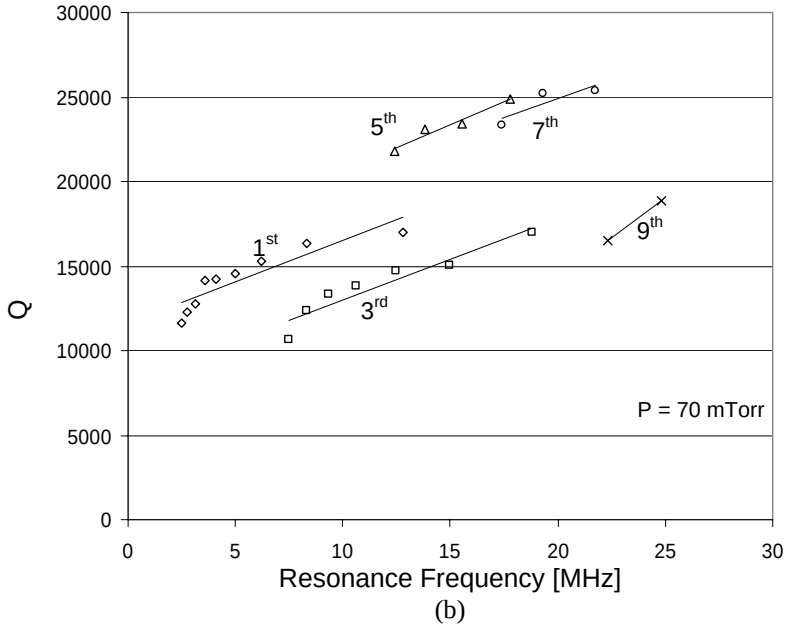

(b)

Figure 8.4: Experimental quality factors of bar resonators operating at (a) atmospheric pressure and (b) 70 μ Torr are shown, along with linear curve fits to each set of modal data.

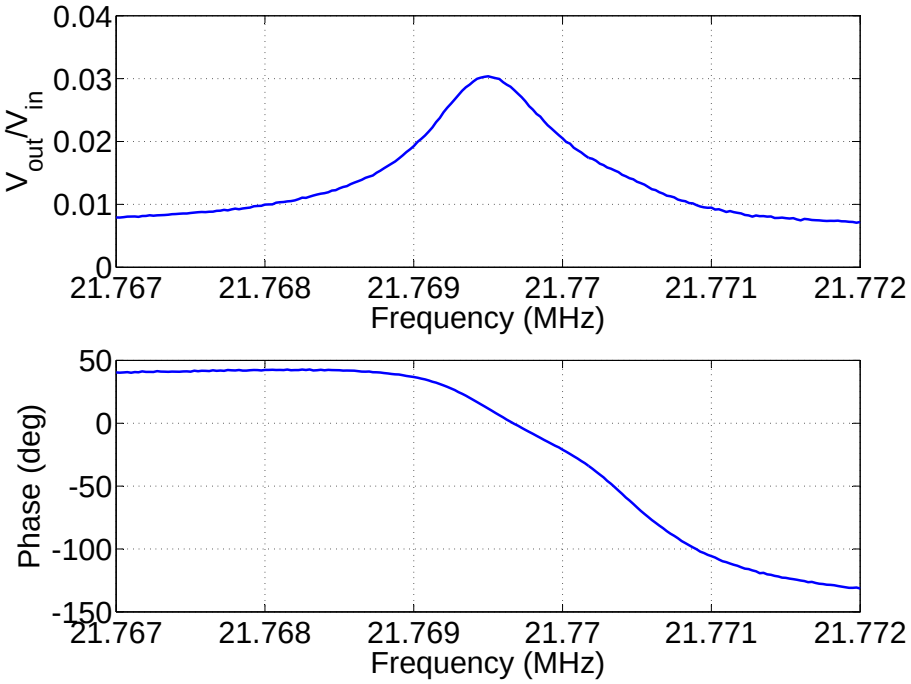

Figure 8.5: Frequency response of a 900 μm long bar resonator near its 7^{th} resonance frequency showing the highest measured quality factor (Q=25,390 at 70 μ Torr. V_{out} is the output voltage of the capacitive bridge circuit with an amplifier stage gain of 100.

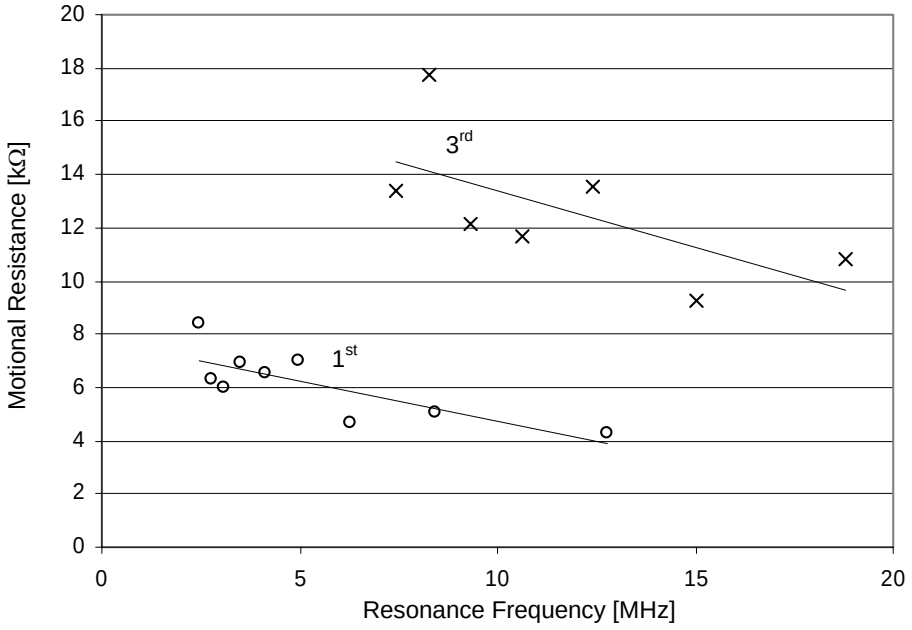

Figure 8.6: Motional resistance of bar resonators operating in their 1^{st} and 3^{rd} modes.

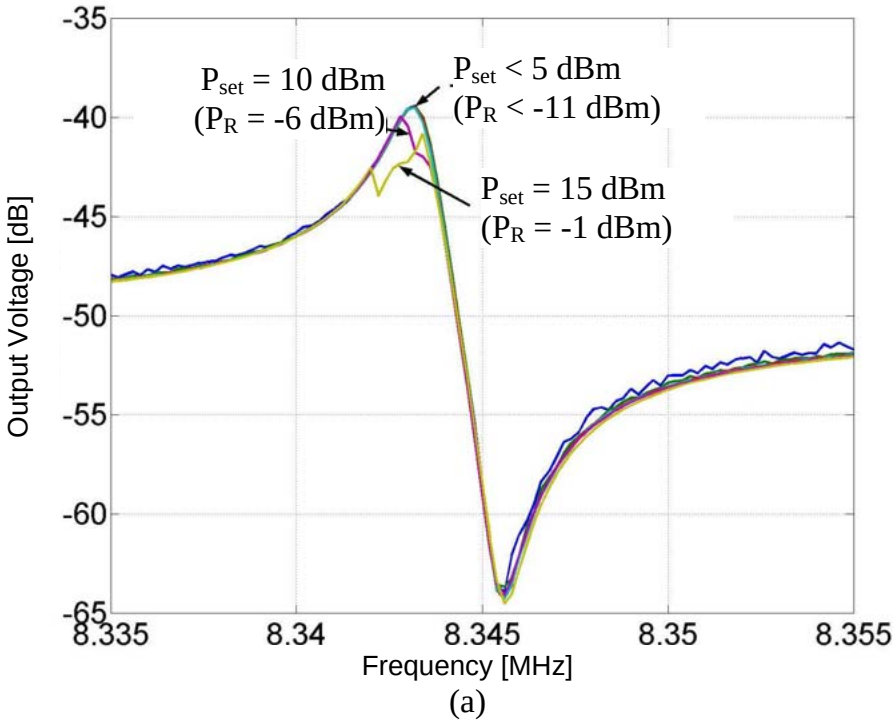

(a)

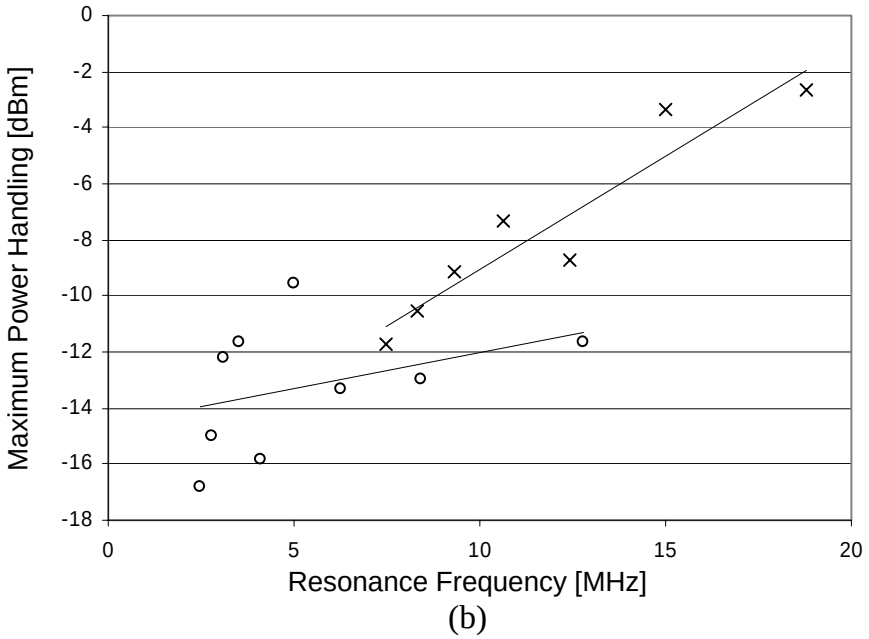

(b)

Figure 8.7: (a) Transmission curve of a 300 μm bar resonator at various input (P_{set}) and device (P_R) power levels exhibiting nonlinear behavior at -6 dBm device power, and (b) measured power handling limits of resonators operating in their 1^{st} and 3^{rd} modes.

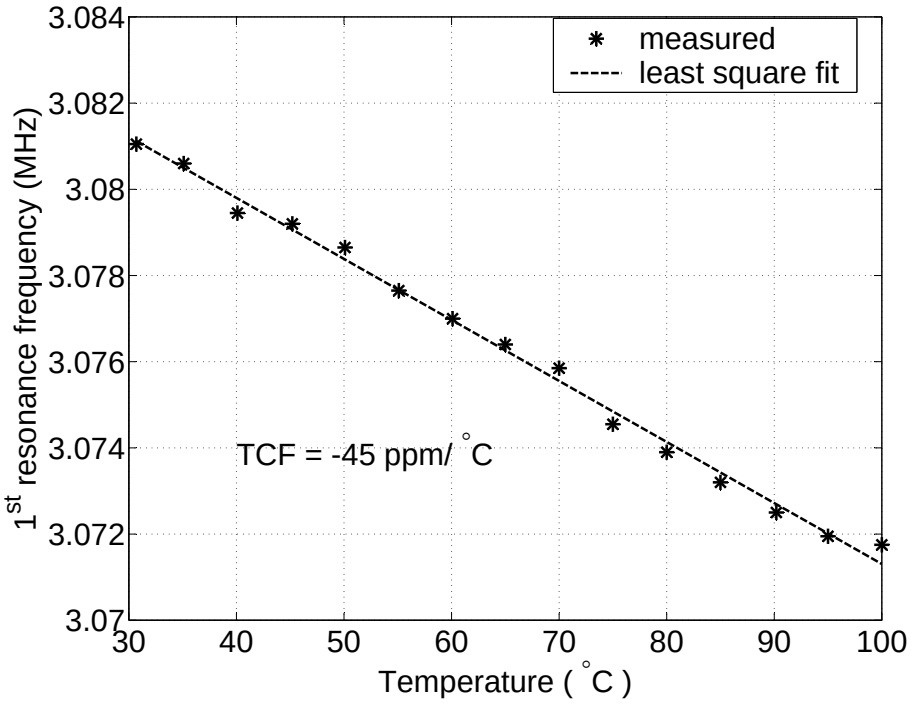

Figure 8.8: Variation in 1^{st} mode resonance frequency for an 800 μm long bar resonator over a temperature range from $30°C$ to $100°C$.

Chapter 9

Conclusion and Future Work

9.1 Resonator Results

Piezoelectric resonators based on single crystal $Al_{0.3}Ga_{0.7}As$ have been realized to take advantage of moderate piezoelectric coupling factor inherent in thin film $Al_{0.3}Ga_{0.7}As$, low loss single crystal nature of $Al_{0.3}Ga_{0.7}As$ as both piezoelectric and electrode layers, and low interfacial damping between piezoelectric layer and electrode layers, i.e. undoped $Al_{0.3}Ga_{0.7}As$ piezoelectric layer and Si doped $Al_{0.3}Ga_{0.7}As$ electrode layers. To this end, four different types of resonators are developed. Namely, cantilever beam, clamped–clamped beam, free–free beam and in–plane length extensional mode bar resonators. All resonators have been analyzed by theoretical model, and FEA modeling, and compared to the measurement results. The measured quality factors of cantilever beam, clamped–clamped beam, and bar resonators in air and vacuum is shown in Fig. 9.1 and Fig. 9.2 respectively. By comparing the quality factors obtained in air and vacuum, it is clear that flexural mode resonators, including cantilever and clamped–clamped beam, must be operated in vacuum in order to achieve a reasonable quality factors for filter implementation. In contrast, bar resonators exhibited a sufficiently high quality factors even without vacuum. For this reason, the application of bar resonators in filter implementation is more realistic. In conclusion, table 9.1 summarizes important results from all

resonator types.

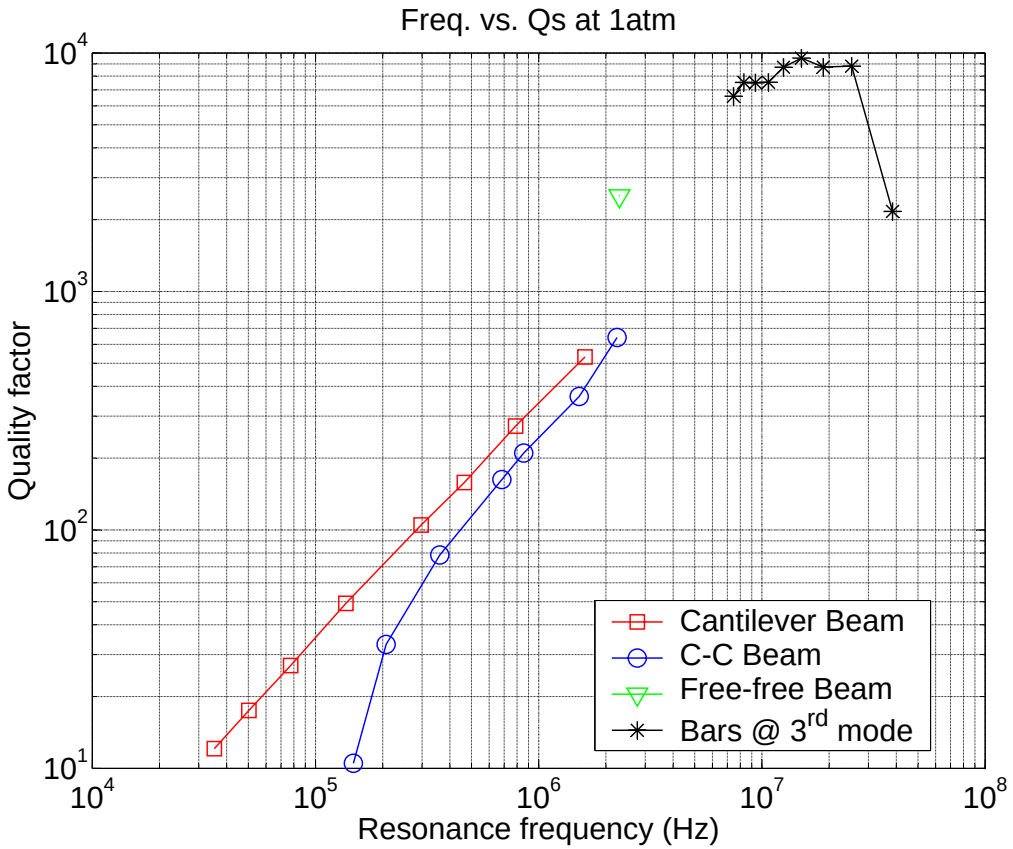

Figure 9.1: Quality factors of resonators at 1 atm.

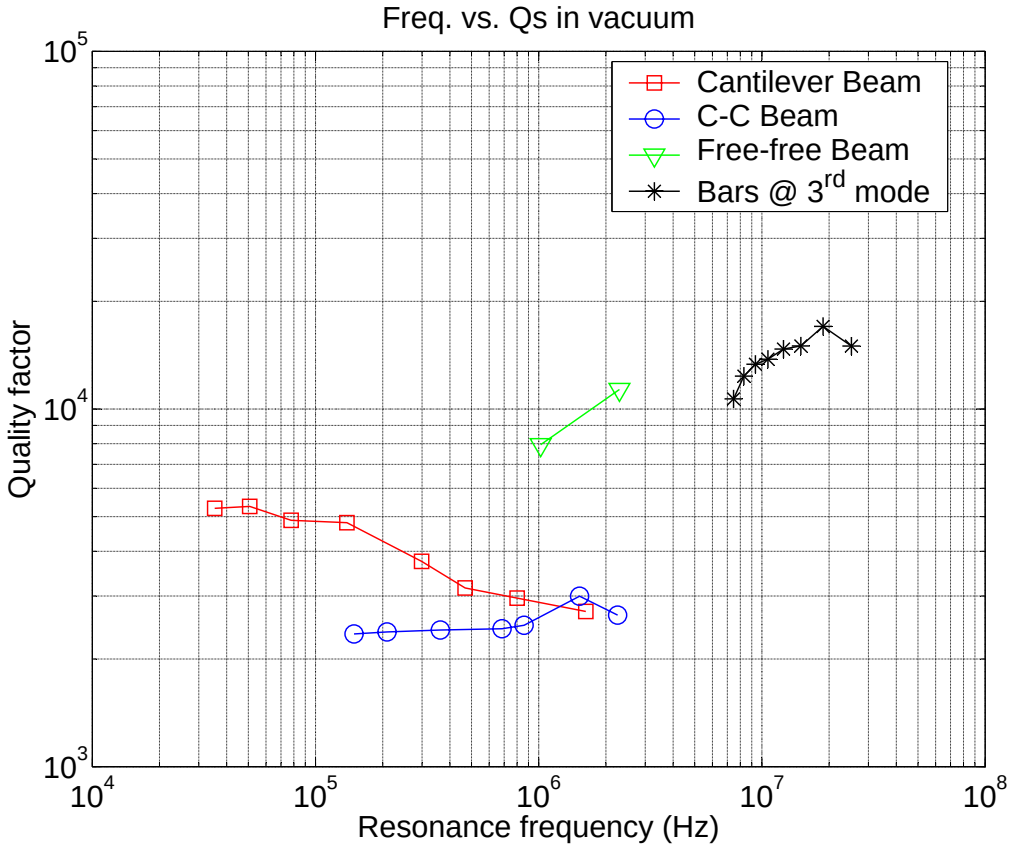

Figure 9.2: Quality factors of resonators in vacuum.

Table 9.1: Results of developed resonators.

Resonator type	Q_{max}	freq. @ Q $_{max}$	f_{max}	Q @ f_{max}	TCF
Cantilever beam	5,277	35.21 kHz	1.62 MHz	5,033	-53.9 $ppm/°C$
C–C beam	3,700	3.1 MHz	3.1 MHz	3,700	176.5 $ppm/°C$
F-F Beam	11,341	2.3 MHz	2.3 MHz	11,341	-53.68 $ppm/°C$
Bar resonator	25,207	19.3 MHz	75.1 MHz	1,621	-45 $ppm/°C$

9.2 Future Work

The developed resonator in this work covers frequency range of 15 kHz to 71 MHz with Qs less than 25,000. In order to meet the requirement of wireless communication industry, higher resonant frequency and higher quality factors are desired. In order to get higher resonant frequency, the resonator dimensions need to be shrinked accordingly. But in order to detect higher resonant frequency, the problems associated with parasitic capacitance must be solved. Fig. 9.3 gives the impedance of 200 long bar resonators in case of internal capacitance only and internal capacitance together with 5 pF of parasitic capacitance assuming a quality factor of 10,000. The figure clearly shows the effect of parasitic capacitance. One of the proposed solution is get rid of parallel capacitance associated with probe pad which in on the order of 100 times of the area of the resonator itself by using metal bridge design. The fabrication process for metal bridge is still under investigation. Another approach is to reduce the parasitic capacitance caused by connection cables. Proposed solution for this problem is wire bonding the resonator chips to sockets or further integrate a buffer units on substrate.

In order to get higher quality factors, efforts should be given to the control of surface quality, reduce anchor width for bar and free–free beam resonators etc.. The ultimate quality factors of resonators are determined by losses due to thermoelastic current and anchor loss.

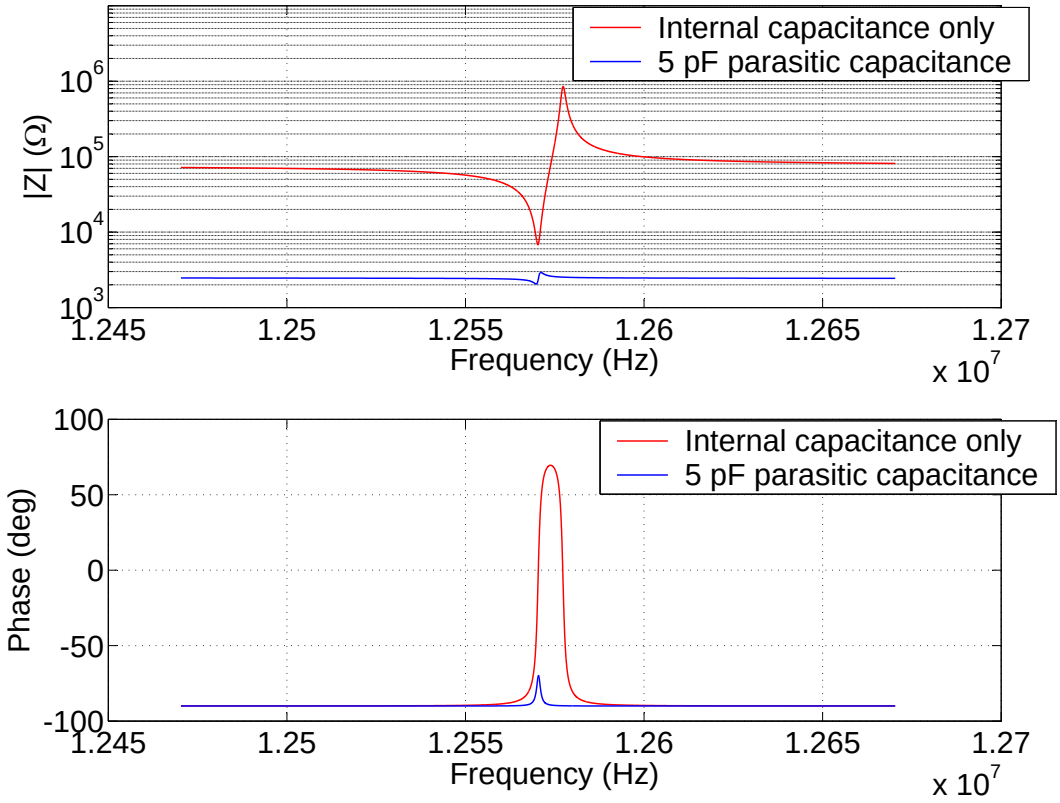

Figure 9.3: Impedance of the bar resonator with existence of parasitic capacitance.

Another design for future high frequency resonators is 2-D disk resonators. In this design, the disk is vibrating in bi–axial breathing mode. 4 support beams are attached to the disk at its node points. So far, the fabricated disk resonators have frequency range of 19.5 MHz to 29 MHz with excellent agreement to the theoretical predictions. The measured quality factors are up to 11,000 in air. Fig. 9.4 gives the SEM view of developed disk resonator. Fig. 9.5 gives transmission spectra of resonator when directly connected to network analyzer.

Based on the developed resonators in this work, bandpass filters can be imple-

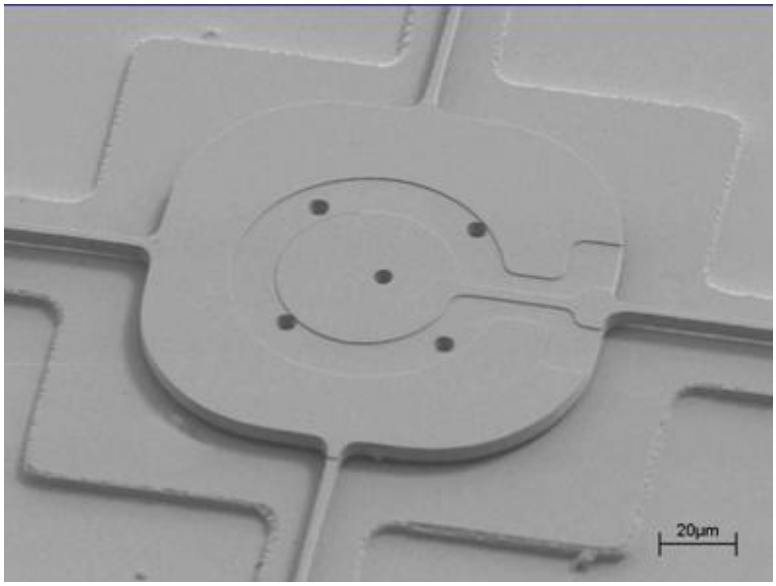

Figure 9.4: SEM image of a typical developed disk resonator.

mented. For low frequency filters, this can be done by mechanical coupling of resonators. When the frequency range goes higher, the required mechanical coupling element will need submicron feature size and accurate positioning, putting complexity in lithography. As an alternative method, electrical coupling of resonators including capacitive coupling and electrical cascading can be adopted to avoid submicron or even nanometer lithography and get more design flexibility [46]. The electrical coupling can first implemented with wire bonded resonators and discrete electrical parts, and can further implemented with integrated circuits.

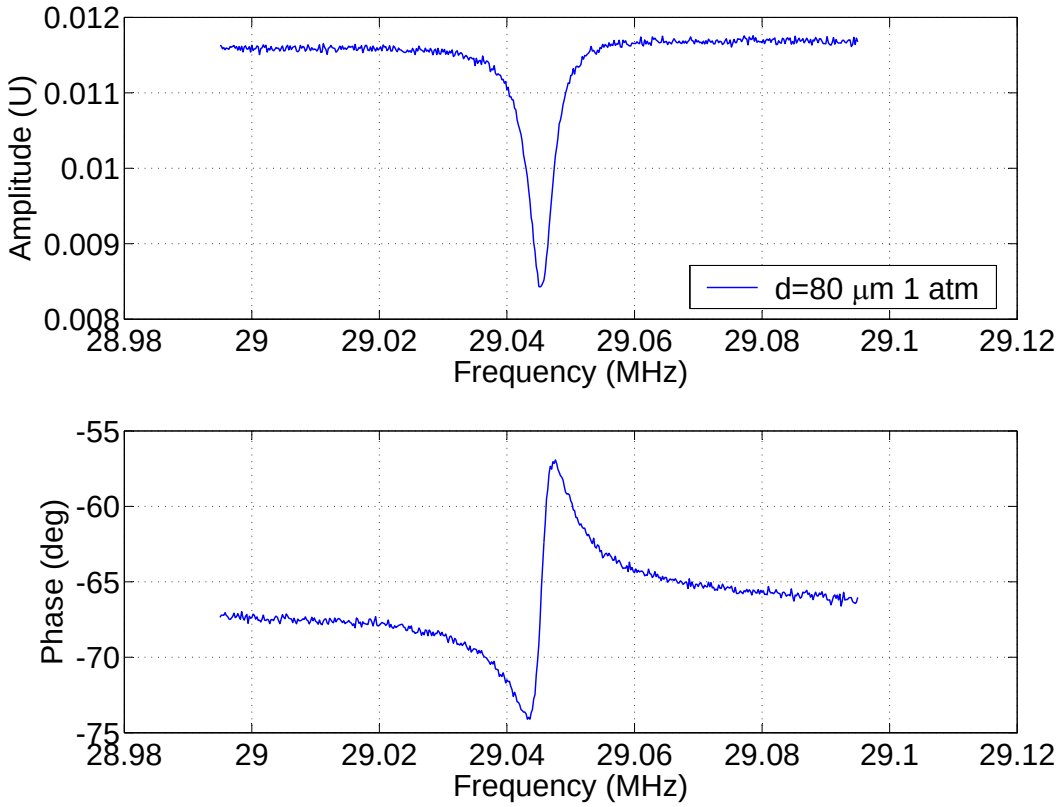

Figure 9.5: Frequency spectra of a disk resonator near resonant frequency.

BIBLIOGRAPHY

[1] R. Aigner, S. Marksteiner, L. Elbrrecht, W. Nessler, "RF-Filters in Mobile Phone Applications", *Transducers 2003*, pp. 891–894, 2003.

[2] T. H. Lee, "The Design of CMOS Radio-Frequency Integrated Circuits", Cambridge University Press, pp. 500–504, 1998.

[3] A. T. Kollias, J. N. Avaritsiotis, "Analysis and Design of Thin Film Resonators Ladder Filters", *Microelectronics Reliability*, vol. 42, pp. 1133–1140, 2002.

[4] M. Hara, J. Kuypers, T. Abe, M. Esashi, "Surface Micromachined AlN Thin Film 2GHz Resonator for CMOS Integration", *Sensors and Actuators A*, vol. 11, pp. 211–216, 2005.

[5] J. Yao, "RF MEMS from a Device Perspective", *Journal of Micromechanics and Microengineering*, vol. 10, R9–R38, 2000.

[6] C. T. C. Nguyen, "Micromechanical Filters for Miniaturized Low-power Communications", *Proceedings of the SPIE - The International Society for Optical Engineering*, vol. 3673, pp. 55-66, 1999.

[7] S. Pourkamali, F. Ayazi, "SOI-Based HF and VHF Single-Crystal Silicon Resonators with Sub-100 Nanometer Vertical Capacitive Caps", *Transducers '03*, pp. 837–840, 2003.

[8] D. L. DeVoe, "Piezoelectric Thin Film Micromechanical Beam Resonators", *Sensors and Actuators A (Physical)*, vol. A88, no.3, pp. 263–272, 2001.

[9] S. Humad, R. Abdolvand, G. K. Ho, G. Piazza, F. Ayazi, "High Frequency Micromechanical Piezo-on-Silicon Block Resonators", *Proc. IEEE International Electron Devices Meeting (IEDM'03)*, Washington DC, pp. 957-960, 2003.

[10] B. Piekarski, D. L. DeVoe, M. Dubey, R. Kaul, "Surface Micromachined Piezoelectric Resonant Beam Filters", *Sensors and Actuators A (Physical)*, vol. A91, no.3, pp. 313–20, 2001.

[11] A. N. Cleland, M. Pophristic, I. Ferguson, "Single-Crystal Aluminum Nitride Nanomechanical Resonators", *Applied Physics Letters*, vol. 79, No. 13, pp. 2070–2072, 2001.

[12] G. Piazza, P. J. Stephanou, J. M. Porter, M. B .J. Wijesundara, A. P. Pisano, "Low Motional Resistance Ring-Shaped Contour-Mode Aluminum Nitride Piezoelectric Micromechanical Resonators for UHF Applications", *Proc. MEMS2005*, pp. 20–23, FL, 2005.

[13] A. Park, T. S. J. Lammerink, J. H. J. Fluitman, "Review of Excitation and Detection Mechanisms for Micromechanical Resonators", *Sensors and Materials*, vol. 5, pp. 143–181, 1993.

[14] K. Wang, C. T.-C. Nguyen, "High-Order Medium Frequency Micromechanical Electronic Filters", *Journal of Microelectromechanical Systems*, vol. 8, no. 4, pp. 534–557, 1999.

[15] W.-T. Hsu, H.R. Clark, C.T.-C. Nguyen, 2001, "A Sub-Micron Capacitive Gap Process for Multiple-metal-Electrode Lateral Micromechanical Resonators", *Proceedings of IEEE 2001*, pp. 349–352, 2001.

[16] X. M. H. Huang, M. K. Prakash, C. A. Zorman, M. Mehregany, M. L. Roukes, "Free-Free Beam Silicon Carbide Nanomechanical Resonators", *Proceedings of IEEE 2003*, pp. 342–343, 2003.

[17] A. N. Cleland, M. L. Roukes, "Fabrication of High Frequency Nanometer Scale Mechanical Resonators from Bulk Si Crystals", *Applied Physics Letter*, vol. 69 (18), pp. 2653–2655, 1996.

[18] G. Piazza, R. Abdolvand, G. K. Ho, F. Ayazi, "Voltage-Tunable Piezoelectrically-Transduced Single-Crystal Silicon Micromechanical Resonators", *Sensors and Actuators A*, vol. 111, pp. 71-78, 2004.

[19] K. Hjort, J. Söderkvist, J. Schweitz, "Gallium Arsenide as a Mechanical Material", *Journal of Micromechanics and Microengineering*, vol. 4, pp. 1-13, 1994.

[20] J. Saderkvist, K. Hjort, "The Piezoelectric Effect of GaAs Used for Resonators and Resonant Sensors", *Journal of Micromechanics and Microengineering*, vol. 4, pp. 28-34, 1994.

[21] S. Rao, "Mechanical Vibrations", 1990.

[22] S. D. Senturia, "Microsystem Design", 2000.

[23] A. Deh, K. Fricke, K. Mutamaba, H. L. Hartnagel, "A Piezoresistive GaAs Pressure Sensor with GaAs/AlGaAs Membrane Technology", *Journal of Micromechanics and Microengineering*, vol. 5, pp. 139-142, 1995.

[24] M. Garrigues, J. L. Leclercq, P. Viktorovitch, "III-V Semiconductor Based MOEMS Devices for Optical Telecommunications", *Microelectronic Engineering*, vol. 61-62, pp. 933-945, 2002.

[25] S. Adachi, "GaAs, AlAs, and $Al_{0.3}Ga_{0.7}As$: Material Parameters for Use in Research and Device Applications", *Journal of Applied Physics*, vol. 58(3), R1-R29, 1984.

[26] J. L. Leclercq, R. P. ribas, J. M. Karam, P. Viktorovitch, "III-V Micromachined Devices for Microsystems", *Microelectronics Journal*, vol. 29, pp. 613-619, 1998.

[27] K. Fobelets, R. Vounchx, G. Borghs, "A GaAs Pressure Sensor Based on Resonant Tunneling Diodes", *Journal of Micromechanics and Microengineering*, vol. 4, pp. 123-128, 1994.

[28] M.-A. Dubois, P. Muralt, "Properties of Aluminum Nitride Thin Films for Piezoelectric Transducers and Microwave Filter Applications", *Applied Physics Letters*, vol. 74, no. 20, pp. 3032-3034, 1999.

[29] S.-H. Kim, J.-H. Kim, H.-D. park, G. Yoon, "AlN-based Film Bulk Acoustic Resonator Devices with W/SiO2 Multilayers Reflectro for RF Bandpass Filter Application", *Journal Vaccum Science Technology B*, vol. 19, no. 4, pp. 1164-1168, 2001.

[30] K. Hjort, "Sacrificial Etching of III-V Compounds for Micromechanical Devices", *Journal of Micromechanics and Microengineering*, vol. 6, pp. 370-375, 1996.

[31] K. E. Speller, H. Goldberg, J. Gannon, E. Laawrence, "Unique MEMS Characterization Solutions Enabled by Laser Doppler Vibrometer Measurements".

[32] "Laser Doppler Vibrometry", http://www.dipmec.unian.it/misure/strumenti/LDV/ldv_en.html.

[33] "Vibrometer Operational Manual", Polytec PI.

[34] D. L. DeVoe, A. P. Pisano, "Modeling and Optimal Design of Piezoelectric Cantilever Microactuators", *Journal of Microelectromechanical Systems*, vol. 9, no. 3, pp. 266-270, 1997.

[35] Agilent technologies, "Agilent Technologies Impedance Measurement Handbook", Dec. 2003.

[36] A. Baz, "Active Vibration Control", Course Notes for ENME 808J, University of Maryland, 2003.

[37] L. Lin, R. T. Howe, A. P. Pisano, "Microelectromechanical Filters for Signal Processing", *Journal of Microelectromechanical Systems*, vol. 7, no. 3, pp. 286-294, 1998.

[38] W. C. Tang, T. Cuong, H. Nguyen, R. T. Howe, "Laterally Driven Polysilicon Resonant Microstructures", *Sensors and Actuators*, vol. 20, no. 1-2, pp. 25-32, 1989.

[39] B. Antkowiak, J. P. Gorman, M. Varghese, D. J. D. Carter, A. E. Duwel, "Design of a High-Q, Low-Impedance, GHz-Range Piezoelectric MEMS Resonator", *Transducers*, pp. 841-846, 2003.

[40] J. Wang, Z. Ren, C. T. C. Nguyen, "Self-Aligned 1.14-GHz Vibrating Radial-Mode Disk Resonators", *Transducers*, pp. 947-950, 2001.

[41] H. M. Cheng, M. T. S. Ewe, G. T. C. Chiu, R. Bashir, "Modeling and Control of Piezoelectric Cantilever Beam Micro-Mirror and Micro-Laser Arrays to Reduce Image Banding in Electrophotography Processes", *Journal of Micromechanics and Microengineering*, vol. 11, pp. 487-498, 2001.

[42] M. L. Roukes, "Nanoelectromechanical Systems", *Solid-State Sensor and Actuator Workshop*, pp. 367-376, 2000.

[43] R. L. Kubena, "MEMS Quartz-Based Resonators for UHF Signal Processing", *DARPA PI Meeting*, Orlando, FI, 2003.

[44] F. Ayazi, "Nano-Precision Integrated Electromechanical Filters for UHF Communication", *DARPA PI Meeting*, Orlando, FI, 2003.

[45] A. Duwel, D. Carter, B. Antkowiak, D. White, J.-M. Kang, J. Gorman, "Selectable MEMS Resonator Arrays", *DARPA PI Meeting*, Orlando, FI, 2003.

[46] S. Pourkamali, R. Abdolvand, F. Ayazi, "A 600kHz Electrically–Coupled MEMS Bandpass Filter", *Proceedings of MEMS 2003*, pp. 702–705, 2003.

[47] Y.-W. Lin, "Series-Resonant VHF Micromechanical Resonator Reference Oscillators", *IEEE Journal of Solid-State Circuits*, vol. 39, no. 2, December 2004.

[48] S. Pourkamali, Z. Hao, F. Ayazi, "VHF Single Crystal Silicon Capacitive Elliptic Bulk-mode Disk Resonators–part II: Implementation and Characterization", *Journal of Microelectromechanical Systems*, vol. 13, pp. 1054–1062, 2004.

[49] K. M. Lakin, "Thin Film Resonator Technology", *Proceedings of IEEE FCS-EFTF*, pp. 1-14, 2003.

[50] L. Li, P. Kumar, P. Boudreaux, D. L. DeVoe, "Piezoelectric Microbeam Resonators Based on Epitaxial $Al_xGa_{1-x}As$ Films", *Proceedings of ASME IMECE*, Washington DC, Nov. 2003.

[51] "Japanese Utility Model Application", no. 55-138824, 1980.

[52] D. J. D. Carter, J. Kang, D. White, A. E. Duwel, "Fabrication and Measurement of and IC-compatible GHz-range Piezoelectric Longitudinal Bar Resonator", *Proceedings of Solid-State Sensor, Actuator and Microsystem Workshop*, Hilton Head SC, June 2004.

[53] P. Kumar, L. Li, L. Calhoun, P. Boudreaux, D. L. DeVoe, "Fabrication of Piezoelectric $Al_{0.3}Ga_{0.7}As$ Microstructures", *Sensors and Actuators*, vol. A115, pp. 96-103, 2004.

[54] A. S. Nowick, B. S. Berry, "Anelastic Relaxation in Crystalline Solids", Chapter 17, Academic Press, 1972.

[55] M. E. Frerking,"Crystal oscillator design and temperature compensation", Van Nostrand, 1978.